

# STUDY AND ANALYSIS OF PARASITIC OSCILLATIONS IN GYROTRONS

## A DISSERTATION

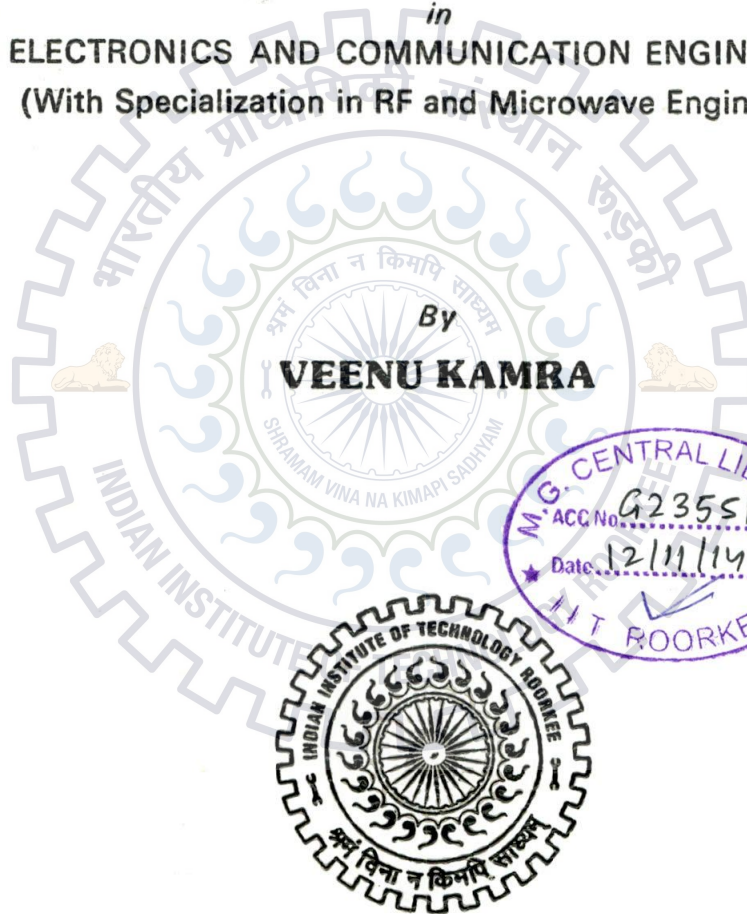
*Submitted in partial fulfillment of the  
requirements for the award of the degree*

*of*

**MASTER OF TECHNOLOGY**

*in*

**ELECTRONICS AND COMMUNICATION ENGINEERING**  
(With Specialization in RF and Microwave Engineering)



By

**VEENU KAMRA**



DEPARTMENT OF ELECTRONICS AND COMMUNICATION ENGINEERING  
INDIAN INSTITUTE OF TECHNOLOGY ROORKEE  
ROORKEE - 247 667 (INDIA)  
JUNE, 2014

---

### CANDIDATE'S DECLARATION


---

I hereby declare that the work being presented in the dissertation entitled, "*Study and Analysis of Parasitic Oscillations in Gyrotrons*" in partial fulfillment of the requirements for the award of the degree of *Master of Technology* in *Electronics & Communication Engineering*, submitted in the Department of Electronics and Communication Engineering, Indian Institute of Technology Roorkee (India), is an authentic record of my own work carried out under the guidance of Prof. M.V. Kartikeyan, Head of Department, Department of Electronics & Communication Engineering, Indian Institute of Technology Roorkee, India and Prof. John Jelonnek, Head of Institute, Institute for Pulsed Power and Microwave Technology, Karlsruhe Institute of Technology, Germany.

The matter embodied in the dissertation report has not been submitted for the award of any other degree elsewhere.

Date : 30/06/14

Place : IIT Roorkee

  
(Veenu Kamra)

---

### CERTIFICATE

---

This is to certify that the above statement made by the candidate is correct to the best of my knowledge.

  
Prof. M.V. Kartikeyan

Head of Department

Electronics & Communication Engg

Indian Institute of Technology Roorkee

Roorkee, India.



Prof. John Jelonnek

Head of Institute, IHM

and Professor, IHE

Karlsruhe Institute of Technology

Karlsruhe, Germany.

## ACKNOWLEDGEMENTS

I would like to express my gratefulness to all who contributed ideas, encouragement and support. I would like to thank, firstly God for giving me grace and wisdom.

I would like to convey my deep sense of gratitude to my supervisor, **Dr. M. V. Kartikeyan**, Professor, Department of Electronics and Communication Engineering and head of the institute computer Center, Indian Institute of Technology Roorkee. His continuous support and motivation at every stage of my research encouraged me to give my best efforts. His vast experience on millimeter wave source design helped me to resolve practical issues and design optimized systems. Apart from knowledgeable guide he is person with humble and kind heart. He has always encourage me for quality research work with innovation.

I specially thank to **Prof. John Jelonnek**, Karlsruhe Institute of Technology, Germany, for his valuable guidance and giving me pleasure to work under his supervision. I feel proud to be a research member of his group.

I am grateful to **Dipl.-Ing. Andreas Schlaich** for his kind cooperation in carrying out my thesis work. His valuable support and time to time guidance in technical issues, which was instrumental in making this dissertation work a success. He always taught me the right direction to work. He is a very good teacher and kind hearted person.

It is pleasure to thank, **Dr. S.N. Sinha, Dr. D. Singh, Dr. N.P. Pathak** and **Dr. A. Patnaik**, for their efforts to build my base of RF and Microwave engineering and expand my horizon of knowledge during entire stay in IIT Roorkee.

Finally, I would also like to thank all my friends for their support and informative

discussions.

Above all, I thank my parents for their never losing trust and confidence on me, even in my tough time and become source of inspiration.

(Veenu Kamra)



## ABSTRACT

Gyrotrons (gyromonotrons) are best suitable high power microwave devices for generation of high powers at microwave and millimeter regimes when comparing with conventional microwave tubes, used for plasma/fusion experiments. In present work, we focus on the problem of parasitic oscillations in the high power gyrotrons. Their origin can be anywhere in the whole geometry either in the region after the gyrotron interaction cavity or before. They can lead to a dynamic modulation of the output power or degrade the efficiency of the gyrotron. The major question which arises is, at which position these parasites are generated and which modes other than cavity mode are excited. The spurious frequencies generated by the parasitic oscillations are the most valuable and direct source of information about the parasites. To analyze such measured frequencies, a new tool called "Brillouin Analysis Tool" was developed in MATLAB. This tool is applied to different measurement data from the KIT step-tunable gyrotron and some also from the W7-X 140 GHz gyrotron to find the position and mode of measured parasitic oscillations.

The investigation of the coupling coefficient variation is a key feature to find the suitable modes of the parasites. The Coupled dispersion relation is also included in the tool to observe the brillouin diagrams. It can be applied to both the cavity mode and the parasites. The tool is also capable to observe the distraction from the uncoupled interaction frequency of the analysing mode (as observed experimentally also).

# Contents

Candidate's Declaration . . . . .	i
Certificate . . . . .	i
Acknowledgements . . . . .	ii
Abstract . . . . .	iv
Table of Contents . . . . .	v
List of Figures . . . . .	vii
List of Tables . . . . .	x
Glossary . . . . .	xi
<b>1 Introduction</b> . . . . .	<b>1</b>
1.1 Background . . . . .	1
1.2 Motivation And Scope . . . . .	2
1.3 Problem Statement . . . . .	3
1.4 Organization of the Thesis . . . . .	4
<b>2 Gyrotron Theory</b> . . . . .	<b>5</b>
2.1 Introduction . . . . .	5
2.2 Principle of Operation . . . . .	5
2.3 Gyrotron Interaction Principle . . . . .	8
2.4 Bunching Mechanism . . . . .	11
<b>3 Theoretical Concepts Behind The Brillouin Tool</b> . . . . .	<b>14</b>
3.1 Introduction . . . . .	14
3.2 Brillouin Diagram . . . . .	14
3.2.1 Voltage depression . . . . .	17
3.2.2 Power Correction . . . . .	17
3.3 Calculating appropriate modes . . . . .	18

3.4	Coupling Coefficient . . . . .	19
3.5	Coupled Dispersion Relation . . . . .	20
3.6	Summary on analysis procedure . . . . .	23
<b>4</b>	<b>Description of Tool</b>	<b>24</b>
4.1	Overview of the Tool . . . . .	24
4.2	Data Import Window . . . . .	26
4.3	Data Analysis Window . . . . .	28
4.4	Brillouin Diagram Window . . . . .	31
4.5	Data Fitting Window . . . . .	32
4.6	Coupling Coefficient Window . . . . .	36
4.7	Coupled Dispersion Relation Window . . . . .	37
<b>5</b>	<b>Analysis Results</b>	<b>39</b>
5.1	Overview . . . . .	39
5.2	Results and Discussion on locating the position and mode for parasitic oscillations . . . . .	40
5.2.1	Case 1 . . . . .	40
5.2.2	Case 2 . . . . .	48
5.2.3	Case 3 . . . . .	61
5.3	Results and Discussion on checking Coupled Dispersion Relation . . . . .	80
5.3.1	Case 1 . . . . .	80
5.3.2	Case 2 . . . . .	85
<b>6</b>	<b>Conclusions And Future Scope</b>	<b>89</b>
6.1	Conclusions . . . . .	89
6.2	Future Scope . . . . .	90
	<b>Bibliography</b>	<b>92</b>

# List of Figures

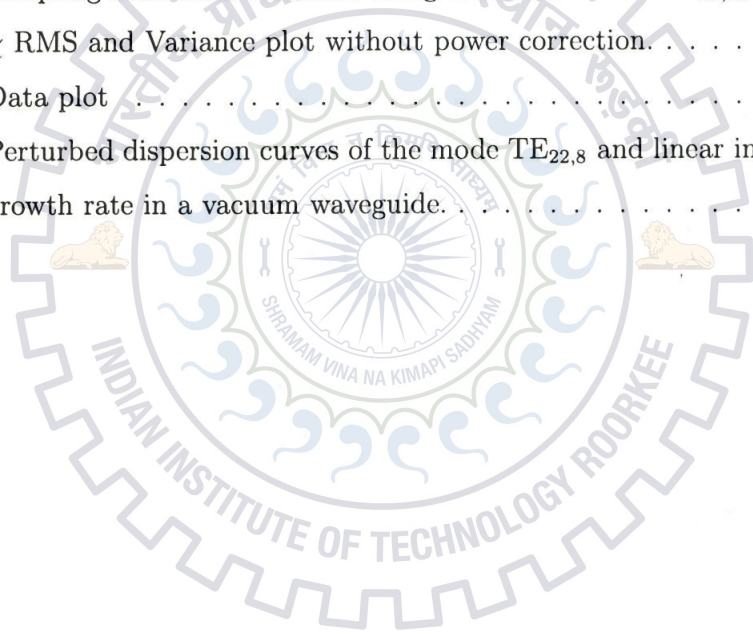
2.1	General classification chart of microwave tubes . . . . .	6
2.2	Schematic of a gyro-oscillator . . . . .	7
2.3	Electron bunching . . . . .	11
2.4	Dispersion diagram of gyrotron oscillator . . . . .	13
4.1	Overview of the tool. . . . .	25
4.2	Data Import window plotting geometry of gyrotron and corresponding magnetic fields. . . . .	28
4.3	Data Analysis window showing plot of $\beta_{\perp}$ without power correction along geometry of gyrotron. . . . .	30
4.4	Plot of $\beta_{\perp}$ with power correction along geometry of gyrotron. . . . .	30
4.5	Brillouin Diagram window showing plot of hyperbola, beam lines and resonance points. . . . .	32
4.6	Data Fitting window showing minima points along RMS deviation and variance curve. . . . .	33
4.7	Plot of $\chi$ values and variance along the geometry . . . . .	34
4.8	Plot of $Z$ values corresponding to the $\chi$ range. . . . .	35
4.9	Plot of minimum variance of $Z$ and average $Z$ value for each $\chi$ value . . . . .	35
4.10	Fifth Window showing different modes depending on a $\chi$ range for a particular $Z$ position. . . . .	37
4.11	Coupled Dispersion Relation Window. . . . .	38
5.1	$\chi$ RMS and Variance plot. . . . .	41
5.2	Brillouin Diagram for Variance minimum 1). . . . .	42



*LIST OF FIGURES*

5.3 Brillouin Diagram for Variance minimum 2). . . . .	43
5.4 Coupling coefficient variation along Z axis for mode $TE_{19,6}$ . . . . .	45
5.5 Coupling coefficient variation along Z axis for mode $TE_{22,5}$ . . . . .	45
5.6 Coupling coefficient variation along Z axis for mode $TE_{21,8}$ . . . . .	47
5.7 Coupling coefficient variation along Z axis for mode $TE_{19,9}$ . . . . .	47
5.8 Data plot . . . . .	49
5.9 $\chi$ RMS and Variance plot. . . . .	50
5.10 Brillouin Diagram for variance minimum 1). . . . .	51
5.11 Brillouin Diagram for variance minimum 2). . . . .	52
5.12 Brillouin Diagram for variance minimum 3). . . . .	52
5.13 Coupling coefficient variation along Z axis for mode $TE_{0,9}$ . . . . .	54
5.14 Coupling coefficient variation along Z axis for mode $TE_{14,4}$ . . . . .	54
5.15 Coupling coefficient variation along Z axis for mode $TE_{22,3}$ . . . . .	56
5.16 Coupling coefficient variation along Z axis for mode $TE_{0,11}$ . . . . .	56
5.17 Coupling coefficient variation along Z axis for mode $TE_{11,7}$ . . . . .	57
5.18 Coupling coefficient variation along Z axis for mode $TE_{22,6}$ . . . . .	59
5.19 Plot of variance in Z as a function of $\chi$ . . . . .	59
5.20 Coupling coefficient variation along Z axis for mode $TE_{17,8}$ . . . . .	60
5.21 Data plot . . . . .	62
5.22 $\chi$ RMS and Variance plot. . . . .	63
5.23 Brillouin Diagram for variance minimum 1). . . . .	64
5.24 Brillouin Diagram for variance minimum 2). . . . .	65
5.25 Brillouin Diagram for variance minimum 3). . . . .	65
5.26 Brillouin Diagram for variance minimum 4). . . . .	66
5.27 Brillouin Diagram for variance minimum 5). . . . .	66
5.28 Brillouin Diagram after optimizing Variance minimum 1). . . . .	67
5.29 $\chi$ RMS and Variance plot for selected data lines (2,3,4,6,7,8,9,10,12,13,14). . . . .	67
5.30 Brillouin Diagram for variance minimum 1). . . . .	69
5.31 Coupling coefficient variation along Z axis for mode $TE_{15,9}$ . . . . .	70

5.32 Coupling coefficient variation along Z axis for mode $TE_{18,8}$ . . . . .	70
5.33 Coupling coefficient variation along Z axis for mode $TE_{19,7}$ . . . . .	72
5.34 Coupling coefficient variation along Z axis for mode $TE_{16,8}$ . . . . .	72
5.35 Brillouin Diagram after optimizing variance minimum 5). . . . .	73
5.36 $\chi$ RMS and Variance plot for selected data lines (1,2,3,6,7,8,9,10,13). . . . .	74
5.37 Coupling coefficient variation along Z axis for mode $TE_{6,14}$ . . . . .	76
5.38 Coupling coefficient variation along Z axis for mode $TE_{20,8}$ . . . . .	76
5.39 Coupling coefficient variation along Z axis for mode $TE_{23,7}$ . . . . .	77
5.40 Coupling coefficient variation along Z axis for mode $TE_{13,11}$ . . . . .	77
5.41 $\chi$ RMS and Variance plot without power correction. . . . .	78
5.42 Data plot . . . . .	82
5.42 Perturbed dispersion curves of the mode $TE_{22,8}$ and linear instability growth rate in a vacuum waveguide. . . . .	83



# List of Tables

5.1	Data file for case 1	40
5.2	Gyrotron constraints	41
5.3	Local minima points in RMS value of $\chi$	42
5.4	Local minima points in Variance curve of $\chi$	42
5.5	Expected modes and their coupling coefficients	44
5.6	Expected modes and their coupling coefficients	46
5.7	Data file for case 2	48
5.8	Gyrotron constraints	49
5.9	Local minima points in RMS value of $\chi$	50
5.10	Local minima points in variance curve of $\chi$	51
5.11	Expected modes and their coupling coefficients	53
5.12	Expected modes and their coupling coefficients	55
5.13	Expected modes and their coupling coefficients	58
5.14	Data file for case 3	61
5.15	Gyrotron constraints	62
5.16	Local minima points in RMS value of $\chi$	63
5.17	Local minima points in variance curve of $\chi$	64
5.18	Local minima points in RMS value of $\chi$	68
5.19	Local minima points in variance curve of $\chi$	68
5.20	Expected modes and their coupling coefficients	69
5.21	Expected modes and their coupling coefficients	71
5.22	Local minima points in RMS value of $\chi$	74
5.23	Local minima points in variance curve of $\chi$	75

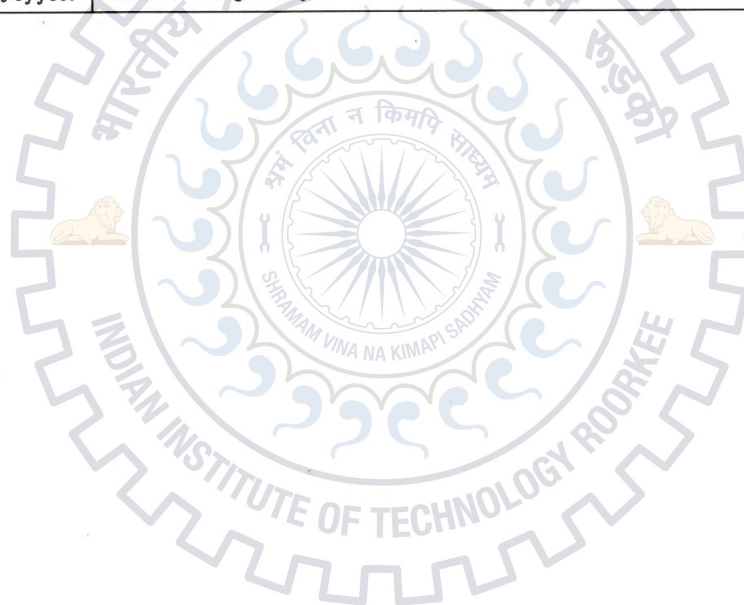
5.24	Expected modes and their coupling coefficients . . . . .	75
5.25	Local minima points in RMS value of $\chi$ . . . . .	78
5.26	Local minima points in variance curve of $\chi$ . . . . .	79
5.27	Gyrotron Constraints . . . . .	80
5.28	Data file for W7-X . . . . .	81
5.29	Analysis of Coupled Dispersion Relation . . . . .	84
5.30	Testing of Mode $TE_{19,6}$ . . . . .	85
5.31	Analysis of Coupled Dispersion Relation . . . . .	85
5.32	Testing of Mode $TE_{22,5}$ . . . . .	86
5.33	Analysis of Coupled Dispersion Relation . . . . .	86
5.34	Testing of Mode $TE_{21,8}$ . . . . .	86
5.35	Analysis of Coupled Dispersion Relation . . . . .	87
5.36	Testing of Mode $TE_{19,9}$ . . . . .	87
5.37	Analysis of Coupled Dispersion Relation . . . . .	87
5.38	Testing of Mode $TE_{7,14}$ . . . . .	88
5.39	Analysis of Coupled Dispersion Relation . . . . .	88

## Glossary Items

$I_b$	Beam current
$U_0$	Accelerating voltage
$U_b$	Beam voltage
$\omega$	Angular frequency
$\Omega_{c0}$	Electron cyclotron frequency
$\Omega_c$	Relativistic electron cyclotron frequency
$v_{ph}$	Electron phase velocity
$v_{\parallel}$	Axial electron drift velocity
$v_{\perp}$	Transverse electron drift velocity
$\beta_{\parallel}$	Parallel normalised velocity
$\beta_{\perp}$	Transverse normalised velocity
$k_{\parallel}$	Axial wave number
$k_{\perp}$	Perpendicular wave number
$\gamma_{rel}$	Relativistic factor
$m$	Azimuthal mode indices
$n$	Radial mode indices
$E$	Electric field
$B$	Magnetic field
$r_L$	Larmor radius
$P_{in}$	Input power
$P_{out}$	Output power
$\alpha$	Velocity ratio
$R_0$	Geometry radius
$R_e$	Beam radius (guiding center radius)

GLOSSARY ITEMS

$m_0$	Rest mass of electron
$e$	Charge of an electron
$c$	Velocity of light
$s$	Harmonic number
$\eta$	Efficiency of gyrotron
$\chi_{mn}$	Eigen value of a particular mode
$p$	Relativistic momentum of electron
$E_{kin}$	Kinetic energy
$f_{offset}$	Offset frequency



# Chapter 1

## Introduction

### 1.1 Background

The demands for energy are increasing so rapidly and the stock of conventional energy resources are depleting so fast, that it is now realised that nuclear energy derived from nuclear fission process can not alone cater to the present day need. Hence the world is now determined to explore the unlimited source of energy which is possible only from the nuclear fusion. Nuclear power or energy is an outcome of basic research in the field of reactor physics. Fusion research requires heating plasmas confined by intense magnetic field to high temperatures of  $10-15 \times 10^6$  Celsius where thermonuclear reactions can take place. Electron Cyclotron Resonance Heating (ECRH) has become a well-established heating method for both tokamaks and stellarators type fusion nuclear reactors [1], which requires high frequency (28 - 240 GHz), high power (0.5 - 4 MW) continuous wave (CW) RF-source. The confining magnetic fields in present day fusion devices are in the range of  $B = 1 - 7$  Tesla.

Even though, solid-state semiconductor devices are used extensively as low power high frequency sources, but they fail to satisfy high power requirements of many applications like Electron Cyclotron Resonance Heating (ECRH), Electron Cyclotron Current Drive (ECCD), material processing etc. Gyrotron oscillators (gyrotrons)

are fast wave devices which can provide hundreds of kilowatts power at millimeter/sub-millimeter frequencies and enable a wide range of technologies. At present, gyrotron oscillators, as sources of high power millimeter waves, play an important role in heating systems for thermonuclear fusion reactors (for details refer [11]). Among many concepts, gyrotrons have uniquely met the needs of the program and continue to excel meeting the increasing demand for high average power sources. There are several other applications also such as deep-space and specialized satellite communication, high-resolution Doppler radar, radar ranging and imaging in atmospheric and planetary science, drivers for next-generation high-gradient linear accelerators, ECR ion sources, submillimeter-wave and THz spectroscopy, materials processing and plasma chemistry [1]. The gyrotron is explained in detail in Chapter 2.

## 1.2 Motivation And Scope

Output power levels in gyrotrons, i.e., in the order of one megawatt have been experimentally obtained with efficiency higher than 0.30 both at low (8 GHz) and high (140 GHz) frequencies. Because of the increasing beam currents and energies, new effects are observed, among which parasitic oscillations may be the most deteriorating one [14] [15]. They are excited by the electron beam prior to the desired gyrotron interaction zone (the cavity: description can be found in section 2.2) or later. It is an old problem in microwave tube development, but here we discuss mainly in megawatt gyrotrons. Parasitic gyrotron oscillations in the frequency range of 120 - 130 GHz have been observed at the FZK/KIT laboratory in the course of the development of the 1-MW 140-GHz CW gyrotron. It lowers the quality factor in order to increase the starting currents of possible unwanted oscillations.

The high energy electron beam can excite waveguide modes in all places where proper resonance interaction between mode and beam is possible. Theoretically



it should do this in the cavity only, but oscillations are observed in other places also which we call parasitics. These oscillations are considered as the cause of the following problems:

- They increase stray radiation significantly, enough to damage components.
- They increase beam parameter spread; for beam tunnel oscillations, this means that cavity mode is degraded; for after-cavity interaction, this means that depressed collector operation is degraded.
- They cause spurious signals, which complicate measurement.

This thesis describes experimental and theoretical investigations of parasitic oscillations. A new measurement data processing tool is introduced to determine and characterize these undesired oscillations, and a dedicated study is presented. Directly from the experiment, we cannot determine from where these oscillations come. On the other hand, simulation of parasitic oscillations is cumbersome and not well verified. This tool enables us to combine multiple parasitic oscillation frequency measurements, and evaluate them together to check if a common position and mode can be found in the gyrotron.

### 1.3 Problem Statement

- To investigate and analyse the parasitic oscillations which are obtained at the output of the gyrotron. They can be generated anywhere in the gyrotron tube.
- The main motive of designing this tool is to:
  - Find out where the oscillations come from.
  - Investigate the mode present.

- The following characteristics have to be designed for this investigation:
  - Implement suitable data import and management: loading different files containing geometry profile, B profile, measured frequencies and beam parameters.
  - Beam parameter calculation: simulation data is conveniently only available in one position, so beam parameters in rest of geometry must be calculated.
  - Automatic fitting techniques and Brillouin representation.
  - Further indicators: coupling coefficient and coupled dispersion relation.

## 1.4 Organization of the Thesis

There are six chapters compiled in this dissertation including the present chapter.

- *Chapter one* gives a brief introduction of gyrotron, along with the motivation and scope and problem statement of this thesis.
- *Chapter two* presents the related gyrotron theory which includes the basic principle of gyrotrons, electron beam, bunching mechanism in gyrotrons, dispersion diagram, beam-wave interaction and RF behavior.
- *Chapter three* deals with the theoretical laws behind the design of the tool.
- *Chapter four* includes the description of the developed tool. It describes the working procedure and different characteristics of the tool.
- *Chapter five* presents sample results and findings.
- *Chapter six* concludes the thesis with the concluding remarks and outline direction for future scope.

## Chapter 2

# Gyrotron Theory

### 2.1 Introduction

In this chapter, a brief review of the principles and theories of gyrotron will be given. A more complete and detailed description can be found in [2] – [9]. This chapter presents useful gyrotron equations, most importantly including a discussion of the mechanism through which the electron beam couples with the RF field and transfers its energy to the resonant cavity mode.

### 2.2 Principle of Operation

Microwave tubes are classified into two part based on the electron velocity.

- Fast wave devices
- Slow wave devices

They are used to generate or amplify coherent electromagnetic radiation. Fast wave devices in which phase velocity  $v_{ph}$  of electromagnetic wave is greater than the speed of light, in contrast, in slow wave devices wave phase velocity is less than velocity of light. Gyrotron is fast wave device which can produce hundreds of kilowatt of power

at very high frequency. According to type electron beam classification of microwave tubes shown in Fig. 2.1.

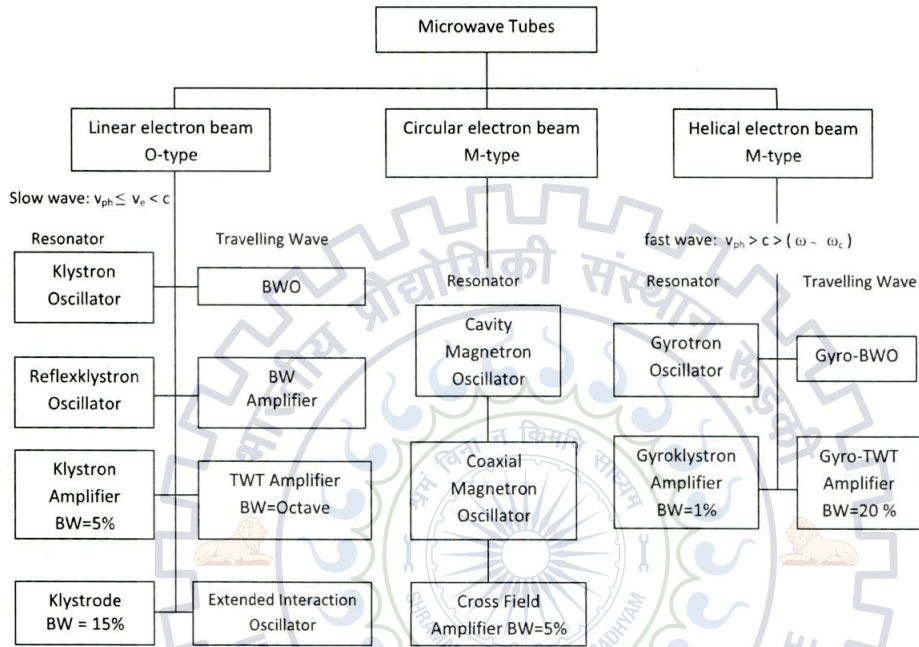


Figure 2.1: General classification chart of microwave tubes (reproduced from [2]).

Fig. 2.2 shows the basic structure of gyrotron. A magnetron-type electron gun is situated at lower end of gyrotron. The voltage applied to the cathode creates the electric field which has both the perpendicular and parallel components with respect to the lines of the magnetic field produced by a solenoid. Thus, electrons emitted from the cathode acquire both the orbital and axial velocity components, and follows helical trajectories. Then, the electrons move towards the cavity in the growing magnetic field, in which the electron flow undergoes the adiabatic compression and the electron orbital momentum increases. In the region of the uniform magnetic field, the electrons interact with the eigenmode of the cavity and transform a part of their kinetic energy into microwave energy. Then, the spent beam exits from the axially open cavity, undergoes decompression in the decreasing magnetic field and settles on the collector. The latter also functions as an oversized output waveguide in the axial

output couplers. The RF output power in the  $TE_{mn}$  mode is coupled through the axial output vacuum window. While in the case of radial output coupling, a quasi-optical mode converter is connected to the output waveguide and transforms the rotating  $TE_{mn}$  mode with axial power flow to a Gaussian mode with a radial power flow. The power is then transmitted through a radially located vacuum window. In Figure. 2.2 both ways of coupling are shown but transversal is state of the art for microwave class continuous wave gyrotrons.

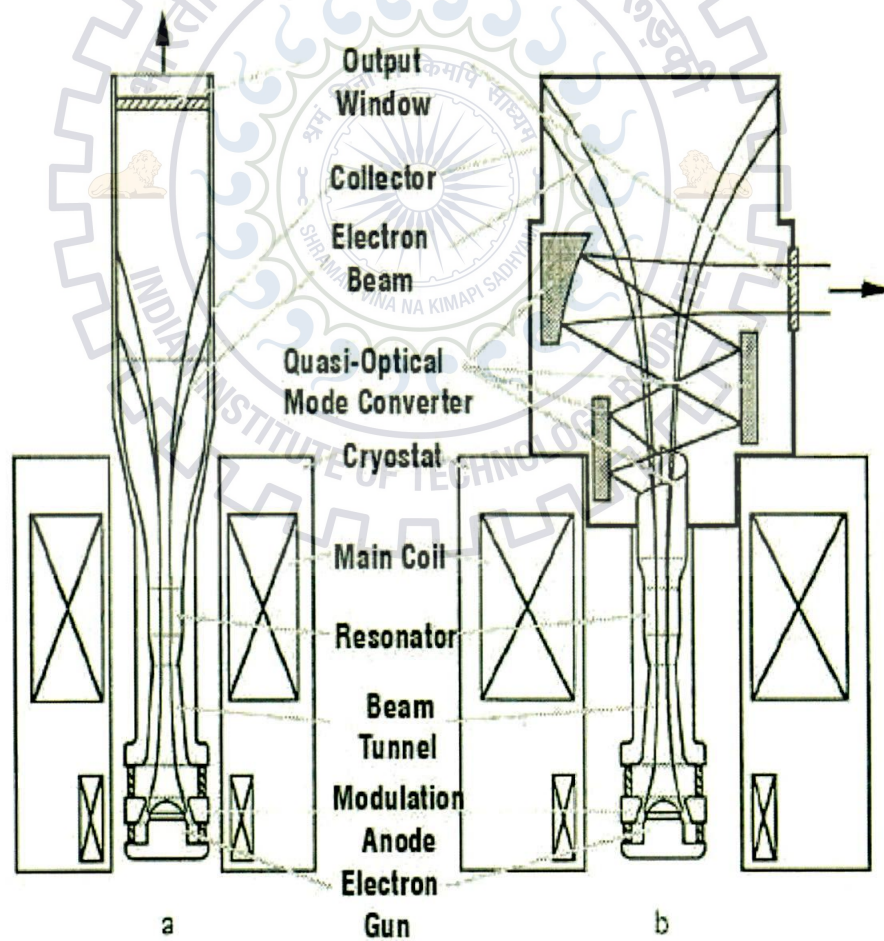


Figure 2.2: Schematic of a gyro-oscillator (reproduced from [8]).

Classical microwave tubes require interaction structures smaller than a wavelength due to the kind of electron coherent radiation involved. Gyrotrons however, are based on the mechanism of coherent cyclotron radiation from electrons gyrating in a constant magnetic field. In these devices, the electrons can resonantly interact with fast waves. Therefore, the interaction space in gyrotrons can be much larger than in classical microwave tubes operating at the same wavelength. Because of this large interaction area, they allow the designer to reduce the power loss density at the cavity walls and with the use of appropriate coolants, wall loading could be further reduced.

With the unique features and wide range of applications, it gives an impact on users and developers that gyrotrons (gyromonotrons) are best suitable high power microwave devices for generation of high powers at microwave and millimeter regimes when comparing with conventional microwave tubes.

### 2.3 Gyrotron Interaction Principle

In the gyrotrons, input power given is DC with accelerating voltage  $U_0$  and beam current  $I_b$ . Electron beam is generated by thermionic emission. In these fast-wave devices electrons undergo oscillations transverse to the direction of beam motion by the action of an external force (field) and hence they radiate. The gyrotron cavity is where the electron beam transfers energy to the transverse electric field mode. This is popularly known as beam wave interaction. The magnetic field in the interaction region (cavity) is chosen in a way that the cyclotron frequency or its harmonics is close to the frequency of the Rf field. The contributions from the electrons reinforce the original emitted radiation in the oscillator. This is the condition of coherent radiation, which is satisfied if a bunching mechanism exists to create electron density variations of a size comparable to the wavelength of the imposed EM wave. To achieve such a mechanism, a resonance condition must be

satisfied between the periodic motion of the electrons and the EM wave in the interaction region [1], [2], [9], [17]:

$$\omega - k_{\parallel} v_{\parallel} \cong s\Omega_c, s = 1, 2, \dots (k_{\parallel} v_{\parallel} = \text{Doppler term}) \quad (2.1)$$

Here  $\omega$  is the wave angular frequency,  $k_{\parallel}$  is the characteristic axial wave number,  $v_{\parallel}$  is the axial electron drift velocity,  $\Omega_c$  is an effective frequency, which is associated with macroscopic oscillatory motion of the electrons, and  $s$  is the harmonic number.

In gyrotrons, EM energy is radiated by relativistic electrons gyrating in an external longitudinal magnetic field which is produced by superconducting magnet. In this case, the effective frequency  $\Omega_c$  corresponds to the relativistic electron cyclotron frequency:

$$\Omega_c = \frac{\Omega_{co}}{\gamma_{rel}} \text{ where } \Omega_{co} = \frac{eB}{m_0} \text{ and } \gamma_{rel} = \frac{1}{\sqrt{1 - (\frac{v}{c})^2}} \quad (2.2)$$

where  $\gamma_{rel}$  is the relativistic factor. A group of relativistic electrons gyrating in a strong magnetic field will radiate coherently due to bunching caused by the relativistic mass dependence of their gyration frequency. Bunching is achieved because, as an electron loses energy, its relativistic mass decreases and it thus gyrates faster. The strength of the magnetic field determines the radiation frequency.

The motion of an electron in an EM field is governed by the Lorentz force equation:

$$\frac{dp}{dt} = -e(E + v \times B) \quad (2.3)$$

where  $p$  is the relativistic momentum of electron,  $-e$  its charge and  $v$  its velocity,  $E$  and  $B$  the electric and magnetic fields, respectively. The velocity is divided into two components i.e.,  $v_{\parallel} = \beta_{\parallel} c$  and  $v_{\perp} = \beta_{\perp} c$ . The component  $v_{\parallel}$  is parallel to the magnetic field and the other one  $v_{\perp}$  perpendicular to it. The electrons gyrate around

the axial magnetic field with electron cyclotron frequency (following equation 2.2 ) given by

$$\Omega_c = \frac{eB}{m_0\gamma_{rel}} \quad (2.4)$$

Here  $m_0$  is the electron rest mass and  $\gamma_{rel} = \frac{1}{\sqrt{1-\beta_{\parallel}^2-\beta_{\perp}^2}}$  the relativistic mass factor, which can also be expressed in terms of the beam voltage  $U_b$ :

$$\gamma_{rel} = 1 + \frac{E_{kin}}{m_0c^2} = 1 + \frac{U_b}{511\text{kV}} \quad (2.5)$$

The electrons follow the helical trajectory around the external field lines of force. The relation between  $U_0$  and  $U_b$  is given in equation 3.7.  $E_{kin}$  is kinetic energy of electrons and can also be expressed as:

$$E_{kin} = m_0c^2(\gamma_{rel} - 1) = eU_b \quad (2.6)$$

The *larmor radius* is the radius of the helical path of a charged particle spiraling about magnetic field lines, i.e. the radius of gyro-motion and is given by

$$r_L = \frac{m_0v_{\perp}}{eB} = \frac{p_{\perp}}{eB} \quad (2.7)$$

The phase bunching process can be mostly understood in a frame of reference in which the axial velocity vanishes. First of all, let us find the rate of change of energy by taking the scalar product of Eq. 2.3 with  $v$ :

$$\frac{dW}{dt} = \frac{dp}{dt} \cdot v = -eE \cdot v, \quad (2.8)$$

since  $(v \times B) \perp v$ . We conclude that those electrons which have a velocity component in the direction of  $E$  are decelerated ( $\dot{W} < 0$ ), and those with a velocity component opposite to  $E$  are accelerated ( $\dot{W} > 0$ ).

In short, we put in DC, which is transformed into kinetic energy of electrons. In the interaction, the E-field of a TE mode decelerates the electrons, by this converting



motion energy into field energy. Of the mode, only the transverse field component acts, so only transverse electron energy can be extracted.

## 2.4 Bunching Mechanism

The phase bunching mechanism can be explained as follows (details can be found in [18]): Consider three randomly phased electrons which are labeled as 1, 2 and 3 as shown in the Fig. 2.3 (a). These three electrons are gyrating about a common guiding center in a uniform magnetic field. As they are gyrating with equal radii ( $r_L$ ) they are said to have equal initial energy ( $|v_1| = |v_2| = |v_3|$ ). Fig. 2.3 (a) shows the phases of rotation and the electron velocities when we start following them. The RF field present in the resonator cavity is described by a radial electric field which we assume to be uniform over the region of interest. Furthermore, let the angular frequency of rotation ( $\omega$ ) be equal to the electron cyclotron frequency ( $\Omega_c$ ).

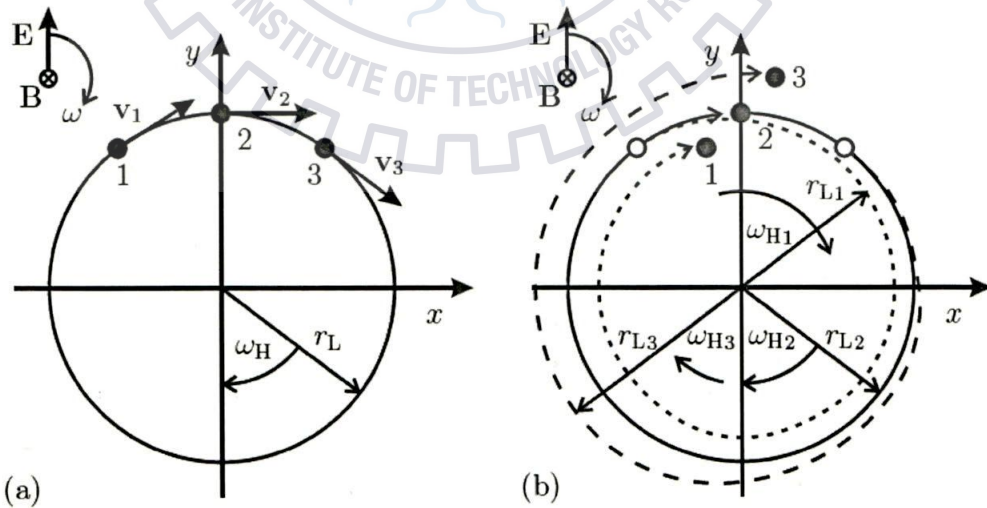


Figure 2.3: Illustration of the azimuthal bunching mechanism in a gyrotron (reproduced from [18]).

Due to the different phases with respect to the rotating electric field, the gyrating electrons may gain energy or transfer it to the field. In the situation shown in (a), electron 1 loses energy and electron 3 gains it, while the field does no work on electron 2 which moves perpendicularly to the field. In (b), the resulting bunching (exaggerated) after one field period is shown. The effect is due to the relativistic dependence of cyclotron frequency on electron energy.

Due to the different angles between velocity and electric field vector the electron energies do not change similarly. We can summarize the effects of Eqs. 2.4, 2.7 and 2.8 as follows:

- The electron 1 gets decelerated as the scalar product  $E \cdot v > 0$ , which leads to an increase in the  $\Omega_c$  and a decrease in the  $r_L$ .
- Electron 2 does not experience any change in energy as the scalar product  $E \cdot v = 0$ . Its cyclotron frequency and Larmor radius remain constant, and it stays in phase with the rotating field.
- The electron 3 gets accelerated as the scalar product  $E \cdot v < 0$ . This slows down the gyration and increases the Larmor radius.

After one field period [see Fig. 2.3 (b)] the electric field again points as in (a), but the electrons have been bunched around the positive y-axis [18].

In cylindrical cavity gyrotrons with radius  $R_0$  the operating mode is close to cutoff ( $v_{ph} = \omega/k_{\parallel} \gg c$ ) and to keep the electron bunches in the retarding phase the frequency mismatch  $\omega - s\Omega_c$  is small but positive. The Doppler term  $k_{\parallel}v_{\parallel}$  is of the order of the gain width and is small compared to the radiation frequency. Cyclotron harmonic operation reduces the required magnetic field for a given frequency by the factor  $s$ . The dispersion diagrams of fundamental and harmonic gyrotrons are illustrated in Figs. 2.4a and 2.4b, respectively. However, efficiencies of gyrotrons

operating at higher harmonics ( $s=2&3$ ) are lower than those operating at the fundamental frequency.

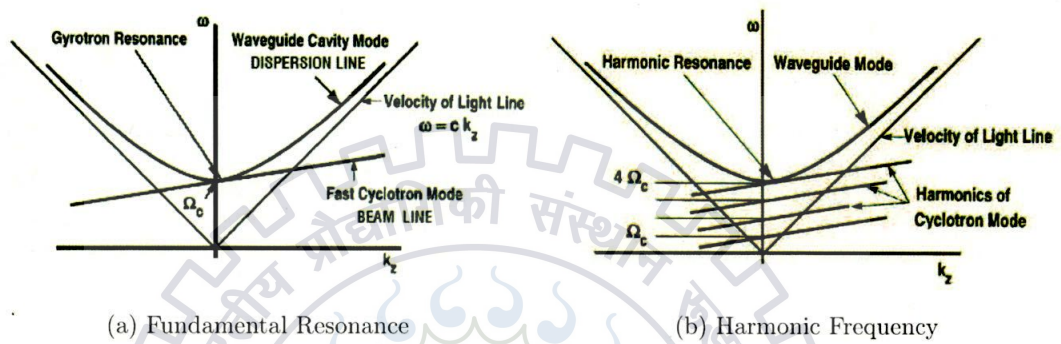


Figure 2.4: Dispersion diagram of gyrotron oscillator (reproduced from [19]).

The dispersion relation shows that there are strict relationships between wall radius, cyclotron frequency, mode frequency and its propagation constant. These relations are the basis of the tool described in the next chapter.

## Chapter 3

# Theoretical Concepts Behind The Brillouin Tool

### 3.1 Introduction

In this chapter, the theoretical concepts of the tool are presented, along with terminology used throughout the application. It mainly includes the adiabatic approximation to the equation of motion and the various constraints which are used for developing of the tool, i.e. power correction, mode approximation, brillouin diagram, coupling coefficient, and the coupled dispersion relation.

### 3.2 Brillouin Diagram

The waveguide dispersion relation of the gyrotron geometry (between beam tunnel entrance and launcher end) tells which modes are able to propagate with which speed and which frequency, through hyperbolic contours in the diagram. The gyrotron beam line (describing the electron beam in an abstract way) intersects these hyperbola where an interaction between the mode described by the hyperbola and the electron beam can take place (shown in figure 2.4). The simplified resonance

### CHAPTER 3. THEORETICAL CONCEPTS BEHIND THE BRILLOUIN TOOL

condition between field and beam is given in equation 2.1 and the waveguide mode dispersion relation can be represented as:

$$k_0^2 = k_{\parallel}^2 + k_{\perp}^2 \quad (3.1)$$

For solving these relations we want certain parameters. From simulation we have  $B(z)$ , and beam parameters ( $E_{kin}$ ,  $\alpha$  and  $R_e$ ) only at one position in the cavity so they must be calculated in the rest of the geometry. From measurement we have  $U_0$ ,  $I_b$ ,  $f$  (RF frequencies) and  $P_{out}$ .

The electrons gyrate rapidly around the guiding center and maximum energy transfer occurs when the electron gyration is approximately synchronous with a rotating field component. Description of the electron motion in crossed electric and magnetic field leads to an approximate, one dimensional equation known as the *adiabatic approximation*. It is valid only if the variations of the electric and magnetic fields are very small as compared to the dimensions of electron trajectories [21].

The relation

$$\frac{p_{\perp}^2}{B} \approx const \quad (3.2)$$

is referred to as the adiabatic approximation, where  $p_{\perp}$  is the transverse electron momentum and  $B$  is the magnetic field [20]. It is used for calculating beam parameters (like  $\beta_{\parallel}$  and  $\beta_{\perp}$ ) along the Z axis (geometry of gyrotron) as we can use the transverse momentum  $p_{\perp}$  as well as normalised velocity  $\beta_{\perp}$ . Initially for calculating these parameters at reference point (Z position in geometry profile at which the beam parameter reference simulation is performed) we want certain equations which are given below:

- Electron energy  $U_b$  and relativistic mass factor:

$$\frac{E_{tot}}{m_0c^2} = \gamma_{rel} = 1 + \frac{U_b}{511 \text{ kV}} = \frac{1}{\sqrt{1 - \beta_{\perp}^2 - \beta_{\parallel}^2}} \quad (3.3)$$

where  $eU_b$  is the beam kinetic energy and  $E_{tot}$  is total energy.

- Beam power  $U_0I_b$ , where  $U_0$  is the accelerating voltage and  $I_b$  is the total beam current.
- Velocity ratio:

$$\alpha = \frac{v_{\perp}}{v_{\parallel}} \quad (3.4)$$

The parameters for resonance points and beam lines in dispersion diagrams are calculated using equations 3.5 and 3.6 respectively. For resonance points, we determine  $k_{\parallel}$  by giving the value of frequency (obtained from the measurement). While beam lines are obtained by giving the range of  $k_{\parallel}$ .

$$k_{\parallel} = \frac{\omega - \Omega_c - 2 \cdot \pi \cdot f_{\text{offset}}}{\beta_{\parallel} c} \quad (3.5)$$

$$\omega = \Omega_c + \beta_{\parallel} ck_{\parallel} + 2 \cdot \pi \cdot f_{\text{offset}} \quad (3.6)$$

These dispersion diagrams are also called  $\omega - k_{\parallel}$  plots or Brillouin Diagrams. For each frequency, at each  $Z$  position a waveguide hyperbola can be defined from the resonance condition. Here  $f_{\text{offset}}$  is used just to facilitate user during operation, i.e. to perfectly match the resonance points into the defined hyperbola. Suitable matching yields an eigenvalue which allows mode guessing. It becomes only meaningful when we use multiple measurement points. If we find a suitable  $Z$  position where one hyperbola fits all points, then in the same instance we have found a probable place of origin and the corresponding eigenvalue. So, the more points, the results will be better.

### 3.2.1 Voltage depression

The influence of space charge forces on the local beam parameters must be considered. Since this space charge is present in the beam, the potential within the beam is reduced with respect to the cavity wall. The amount of voltage depression depends on beam current  $I_b$ , axial velocity  $\beta_{\parallel}$  and ratio of cavity to beam radius. It causes a large kinetic energy degradation as the beam current is increased. In a conventional hollow cavity, it is given by

$$\Delta U_b = U_0 - U_b = \frac{I_b}{2\pi\epsilon_0 c\beta_{\parallel}} \ln \frac{R_0}{R_e} \quad (3.7)$$

where  $U_0$  is the accelerating voltage,  $R_0$  is the cavity radius and  $R_e$  is the average radius of guiding centers at interaction.  $R_0$  is available from geometry profile and  $R_e$  must be calculated using adiabatic approximation, as from the simulation data we have  $R_e$  at only reference position.

### 3.2.2 Power Correction

When in the imported data we have  $P_{out}$  values, then power correction after beam-wave interaction makes sense. The gyrotron cavity is where the electron beam transfers energy to the transverse electric field mode, so power correction is actually needed behind the cavity, i.e.  $Z > Z_{cavity}$  to give meaningful results. Also note that the power extraction is (with some simplification) only affecting the transverse energies, hence we use the measured power to correct  $\beta_{\perp}$  and with this  $\gamma_{rel}$  will also change for  $Z > Z_{cavity}$ . If we have an estimate for the power loss between cavity and output window, the measured power can be scaled up accordingly. Also note that this way of calculation is very primitive, since it assumes that energy is extracted from all electrons in the same way. In reality, it depends on the bunching, and the beam parameters are spread very far after the power extraction. Here, be simply

assume that the average electron energy can be considered this way.

DC power in input beam is given by :

$$P_{in} = U_b I_b \quad (3.8)$$

Beam Voltage after extraction of power from beam can be presented as:

$$U_{b2} = (P_{in} - P_{out})/I_b \quad (3.9)$$

where  $P_{out}$  is output power from the gyrotron. Corrected  $\gamma_{rel}$  and  $\beta_{\perp}$  are showed below:

$$\gamma_2 = 1 + \frac{eU_{b2}}{m_0 c^2} \quad (3.10)$$

$$\beta_2 = \sqrt{1 - \frac{1}{\gamma_2^2}} \quad (3.11)$$

$$\beta_{\perp 2} = \beta_2^2 - \beta_{\parallel 1} \quad (3.12)$$

The values of  $\beta_{\perp 2}$  are smaller than the  $\beta_{\perp 1}$  due to the reduction of power present in the beam. After interaction in the cavity  $\beta_{\perp}$  follows the path of  $\beta_{\perp 2}$ .

### 3.3 Calculating appropriate modes

For high-power, high-frequency devices the effective mode density is high, since the spectrum is dense and the current is above the starting threshold for many modes. However, for a given set of parameters, any one of the several modes can be the stable operating mode, but typically only one of these has high efficiency.

Here we have to find the appropriate mode of the parasitic oscillation frequency that we are considering. Eigenvalues along the whole geometry can be calculated



by using the following equation

$$\chi = R_0 k_{\perp} \quad (3.13)$$

where

$$k_{\perp} = \sqrt{k_0^2 - k_{\parallel}^2} \quad (3.14)$$

here  $k_{\parallel}$  is taken from equation 3.5 and  $k_0$  is defined as  $\omega/c$ . In this  $\omega$  is the angular RF frequency which is available in measurement data.

Root mean square values and variance in the eigenvalues along whole geometry are also calculated for different measurement data to find the suitable eigenvalue and position. In the “normal” curve we take the points and assume that they come from one  $Z$  location, and we investigate the variance of  $\chi$ . The inversion is more complicated, but much more physical, in this, inverse  $Z$  values are calculated to cross examine the curve. From this curve we will be able to get the answer of the following question: “If the correct eigenvalue is  $\chi_0$ , how far do we have to spread out the points on the  $Z$  axis to make them match?”. By providing the eigenvalue range we can check their position of existence along the  $Z$  axis, i.e. we assume a fix  $\chi$  for all points, and allow the points to be spread out on the  $Z$  axis. For this reason, we have calculated variance( $Z(\chi)$ ). Theoretically normal  $\chi$  curve and inversion curve should resemble each other, and it is also proved in our analysis results (see Figure 4.7 and 4.8).

### 3.4 Coupling Coefficient

From the Brillouin diagram, we find one or several  $(Z, \chi)$  combinations which are likely the source of parasitic oscillations. The resonance condition only considers relative motion along the  $Z$  axis of beam and mode, and the cyclotron frequency.

But, the beam–mode coupling is also determined by the field structure, since the beam radius must be in a place where there is sufficiently strong field. We use the found eigenvalue in the coupling coefficient calculation, to find probable modes in the eigenvalue range we have determined.

The important point for this study is that the starting current is inversely proportional to the beam–field coupling constant. In general, the coupling coefficient is given by following equations [2]:

$$C_{mn}G_{mn} = \pm \frac{J_{m\pm s}(k_{mn}R_e)}{J_m(\chi_{mn})\sqrt{\pi(\chi_{mn}^2 - m^2)}}; \quad (3.15)$$

$$\text{Coupling Coefficient} = C_{mn}^2 G_{mn}^2 k_{mn}^2; \quad (3.16)$$

where  $k_{mn}$  is  $k_{\perp}$ . In gyrotrons the electron beam radius  $R_e$  is usually chosen such as to maximize the coupling of the electron beam to the RF field, which is polarized either co-rotating or counter-rotating with respect to the gyrating electrons ( $|J_{m\pm s}(k_{mn}R_e)|$  is maximum). We can see the variation of coupling coefficient along geometry in Figure ??.

From the beam-field coupling coefficient  $= C_{mn}^2 k_{mn}^2 J_{m\pm s}^2(k_{mn}R_e)$  one can see that:

- when  $J_{m+s}(k_{mn}R_e) < J_{m-s}(k_{mn}R_e)$ , only the co-rotating wave is excited;
- when  $J_{m+s}(k_{mn}R_e) > J_{m-s}(k_{mn}R_e)$ , only the counter-rotating wave is excited;
- when  $J_{m+s}(k_{mn}R_e)$  and  $J_{m-s}(k_{mn}R_e)$  are comparable, and both nonzero, it is difficult to determine exactly how much of each rotating component is present.

### 3.5 Coupled Dispersion Relation

A linear theory of cyclotron instability of a beam of electron oscillators in a waveguide, i.e., gyrotron (from [23]) is used. There is a so-called “coupled dispersion

relation", which takes into account the distortion of the waveguide dispersion relation due to the electron beam. More theory about this can be studied in [24], [25], [26], [27], [28]. The dispersion relation describes the dispersion of the eigen modes of the waveguide, i.e. gyrotron, which is penetrated by a beam of electron oscillators. For an electron beam of finite density, the waveguide and beam modes are coupled to one another and thereby are both perturbed. The perturbation is strongest near the points of intersection between the dispersion curves of the waveguide and beam modes. In the vicinities of these points, the modes are unstable (having a considerable growth rate). The two maxima in the growth rate correspond to two resonant points where the unperturbed dispersion curves of the waveguide and beam modes intersect. The dispersion curves  $f = Re(\frac{\omega}{2\pi})$  are calculated by solving the dispersion relation 3.17 for a vacuum waveguide. In this, we have not considered the electron plasma density inside the waveguide. The instability growth rate is given by  $Im(\frac{\omega}{2\pi})$ .

$$\omega^2 - \omega_{mn}^2 = \frac{2\nu c^2 \chi_{mn}^2}{\gamma N_{mn} R_0^2} \left[ \frac{(\omega^2 - c^2 k_{\parallel}^2)}{(\omega - \Omega_c)^2} \beta_{\perp}^2 H_{sm}(X_0, X_L) + \frac{(\omega - k_{\parallel} c \beta_{\parallel})}{(\omega - \Omega_c)} Q_{sm}(X_0, X_L) + U_{sm}(X_0, X_L) \right] \quad (3.17)$$

where the described dimensionless quantities  $X_0, X_L$  can be defined as

$$X_0 \equiv \frac{\chi_{mn}}{R_0} R_e \quad (3.18)$$

$$X_L \equiv \frac{\chi_{mn}}{R_0} R_L \quad (3.19)$$

and the rest variables are

$$H_{sm}(X_0, X_L) \equiv [J_{s-m}(X_0) J'_s(X_L)]^2 \quad (3.20)$$

$$Q_{sm}(X_0, X_L) \equiv 2H_{sm}(X_0, X_L) + 2X_L J_{s-m}(X_0) J'_s(X_L) \cdot \left\{ J_{s-m}(X_0) J''_s(X_L) + \frac{s-m}{s} \frac{X_L}{X_0} J'_{s-m}(X_0) J'_s(X_L) \right\} \quad (3.21)$$

$$U_{sm}(X_0, X_L) \equiv X_L J'_s(X_L) \left[ J_s(X_L) \left\{ \left[ 1 - \frac{s-m}{X_0^2} \right] J_{s-m}^2(X_0) - [J'_{s-m}(X_0)]^2 \right\} - 2 \frac{s-m}{s} \frac{X_L}{X_0} J'_s(X_L) J_{s-m}(X_0) J'_{s-m}(X_0) \right] \quad (3.22)$$

$$N_{mn} \equiv (\chi_{mn}^2 - m^2) J_l^2(\chi_{mn}) / 2\chi_{mn}^2 \quad (3.23)$$

$$\omega_{mn}^2 = c^2(k_{\parallel}^2 + \chi_{mn}^2/R_0^2) \quad (3.24)$$

The beam mode  $\Omega_c$  in the resonance term is given in equation 2.1.

Budker's parameter  $\nu$  used in dispersion equation is defined as

$$\nu = Ne^2/m_0c^2 \quad (3.25)$$

where  $N$  is the electron number density per unit axial length. Relativistic larmor radius at interaction  $R_L$ , as given in [2]

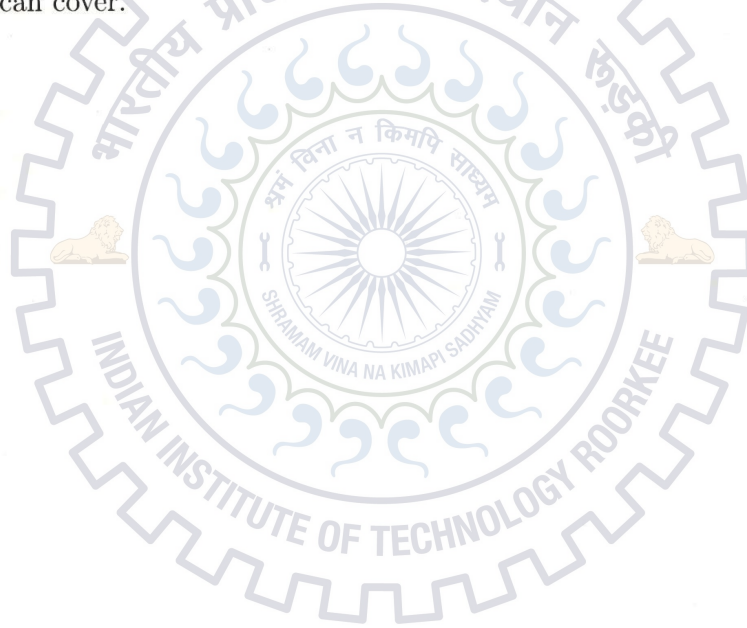
$$R_L = r_L \gamma_{rel} = \frac{c \gamma_{rel} \beta_{\perp}}{\Omega_0} = \frac{v_{\perp}}{\Omega_e} = 1.705 \text{ mm} \times \frac{\gamma_{rel} \beta_{\perp}}{B(\text{T})} \quad (3.26)$$

The eigenvalue problem given by the dispersion relation 3.17 can be considered as that of finding eigenfrequencies  $\omega$  for given wavenumber  $k_{\parallel}$ , or that of finding eigenwavenumbers  $k_{\parallel}$  for given frequency  $\omega$ . At a given wavenumber  $k_{\parallel}$ , the dispersion equation 3.17 is a quartic equation in  $\omega$ , thereby giving four eigenfrequencies  $\omega$ . If any of the four roots is complex, i.e.,  $\omega = \omega_r + \omega_j$ , we consider that mode unstable with a growth rate given by  $\omega_j$  at the real frequency  $\omega_r$ . Close examination of 3.17 reveals the following properties:

- There are two modified waveguide modes with  $\omega \simeq \pm\omega_{mn}$  (3.24), which are always stable, representing waves propagating in opposite directions.
- There exist two modified beam modes with  $\omega \simeq \Omega_c$ , (forward waves in 2.1), which may be unstable.

### 3.6 Summary on analysis procedure

In the analysis procedure, frequencies of parasitic oscillations are measured experimentally [30], varying external parameters like  $U_0$  or  $B$  field. As long as these frequencies only change slightly and monotonously, we assume them to come from the same mode in the same position inside the gyrotron. Our assumption can be checked in an indirect way, which is used by the tool. If we find a fitting  $(\chi, Z)$  combination, then the assumption will be justified. If we don't find the best fitting combination in the brillouin diagram, then the situation is more complicated than the tool can cover.



# Chapter 4

## Description of Tool

The described functionality was implemented as a “Brillouin Analysis Tool” in MATLAB. This chapter contains a description of the graphical user interface and serves as a user instruction manual.

### 4.1 Overview of the Tool

The tool requires file based input data, which is imported in the **Data Import**, i.e., opening window. All further data processing is internal, however result data can be exported into matlab workspace files and figure, e.g. as pdf. With the help of this tool, we analyse the data present, calculate the different characteristics of the beam (parameters), and observe the position and mode of the parasitic oscillations. All the measurement data and simulated data must be available in order to do the same. The beam parameters at the reference point are simulated with the KIT code ESRAY.

An overview of the steps which are to be done while using this tool, is shown in the following fig 4.1. The whole tool consists of six windows to perform the operations mentioned in the steps. The working of each window is described in detail in the following sections in easy-to-learn environment. We can move to the other window

one by one or after completing the operation of one window, we can proceed to the next one for further operations.

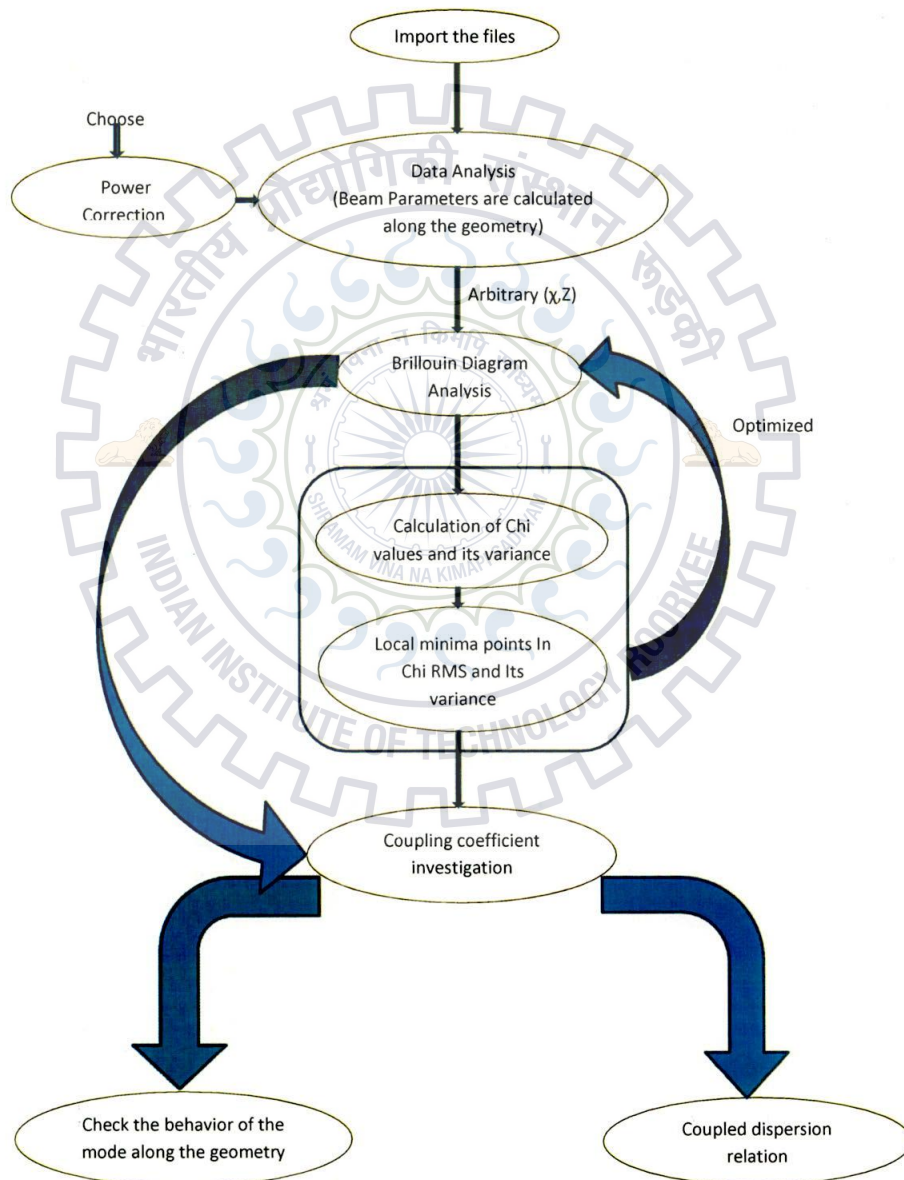


Figure 4.1: Overview of the tool.

## 4.2 Data Import Window

In the **Data Import** window, we first import all the data files which will be used in our analysis, i.e

- geometry profile of gyrotron,
- magnetic field profile, and
- main data file containing the measurement data and simulation data like cathode voltage, beam current, frequency, output power, kinetic energy, alpha, beam radius at reference point (refer Table 5.1).

The data in the geometry profile contains  $R_0$  vs  $Z$ , while magnetic field profile has  $B$  variation along  $Z$  axis. Main data file contains different data lines depending on variation in cathode voltage or B profiles (as given in Table 5.1 or 5.7). These are basically different measurement data which are sampled for analysis. Then we have to choose whether geo profile and B profile are in mm range or m range. In this we can load as many magnetic field profile as we want for making assignment. Then following steps have to be done:

- We have to specify the cavity center location in the respective coordinates, which is the crucial alignment information.
- The user has to give the value of  $Z$  discretization and reference point ( $Z$  position in geometry profile at which the beam parameter reference simulation is performed).

Both profiles are interpolated according to the user defined discretization between two  $Z$  points. This is done due to the non availability of uniform data and also to make synchronization of both profiles which makes our calculation easier. Discretization in the range of 0.1–0.5 yields good results, extra large value will not be



useful for calculating uniform beam parameters and extra small value will take long time to evaluate parameters which degrades the performance of tool. When the cavity centers of geometry profile and B profile are different, then co-alignment of B profile with respect to geometry profile is done. Then

- load the above defined files using these options, i.e.

- After selecting common Z range of both profile files, it will plot the figure.

While loading the main data file, if output screen shows the message that it already contains the assigned magnetic field profile (i.e. for each data row, a B filename is specified), then there is no need to import B profile, one can directly load B profile by hitting . It should be always remembered that the tool expects a B profile file of that name in the same directory where the main data file exists, otherwise there will be an error. Figure 4.2 presents the **Data Import** window showing all the defined features.

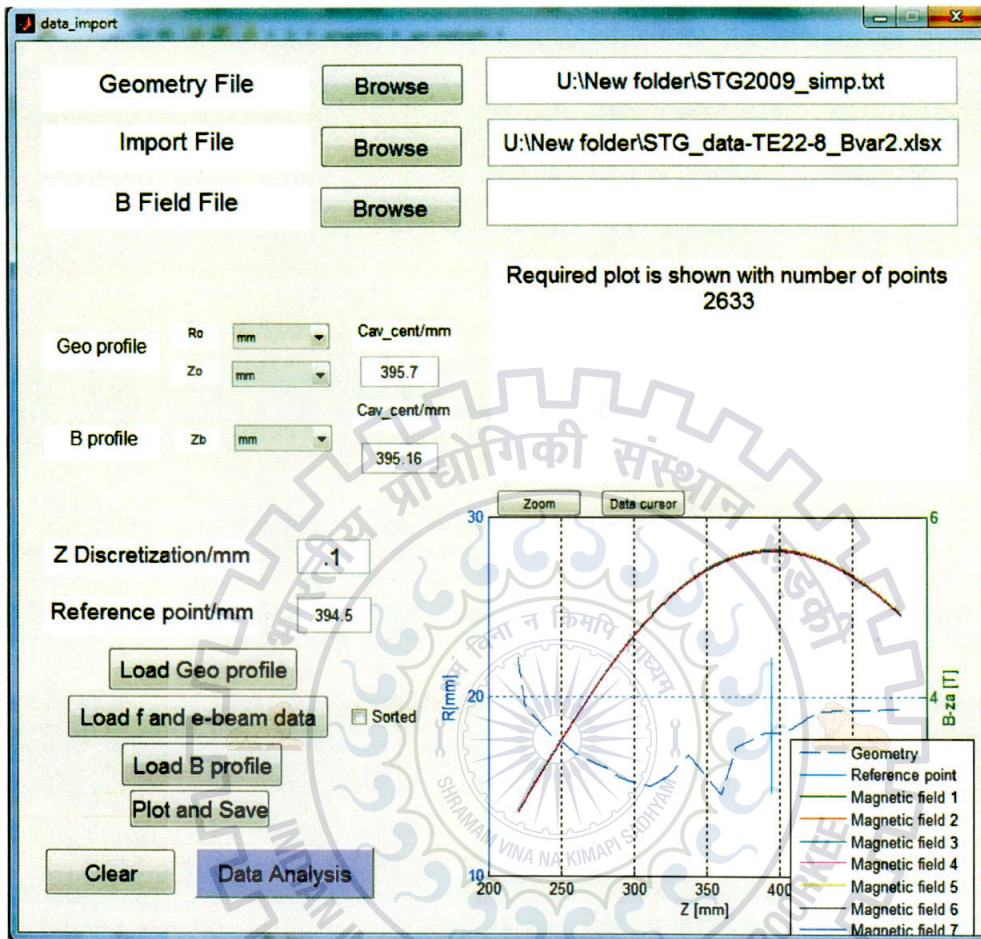


Figure 4.2: Data Import window plotting geometry of gyrotron and corresponding magnetic fields.

### 4.3 Data Analysis Window

On clicking **Data Analysis**, 2nd window will open as shown in Figure 4.3. It takes the data present in all the loaded files as input from the 1st window and will give an overview of the imported data.

- A table shows the imported data.
- **Assign**: We can select the rows and assign a particular B profile to them appearing in pushdown button.

- **Delete Field**: We can also delete particular B profile appearing in the push down button.
- **Calculate**: We calculate here the beam parameters for all points of the co-aligned and interpolated geometry, and this is the basis for all following actions in the tool.
- One more option is introduced, i.e, **Power Correction** (refer subsection 3.2.2). As in the cavity, RF interaction takes place. Some power from electron beam gets extracted to RF Beam. So at the output, reduced power is obtained. For this reason **Power Correction** is introduced, for getting correct parameters after RF interaction.
- Measured power is also affected by **Power Loss** which is occurring while traveling from launchers and reflecting mirrors. Both these features (earlier one and present one) makes sense only when we have measured output power. Define **Power Loss** in percentage. For example, if the measured power is 700 kW, the assumption of 5% loss between cavity and calorimeter will scale up the power assumed for the beam parameter correction to 735 kW.
- **Plot** We have to select the data lines from the table then it will plot different parameters ( $\beta_{\perp}$ ,  $\beta_{\parallel}$ ,  $\gamma$ , depression voltage, resonant frequency) for the selected rows. For example Figure 4.3 and 4.3 show the  $\beta_{\perp}$  without power correction and with power correction respectively, also showing the features of the window.

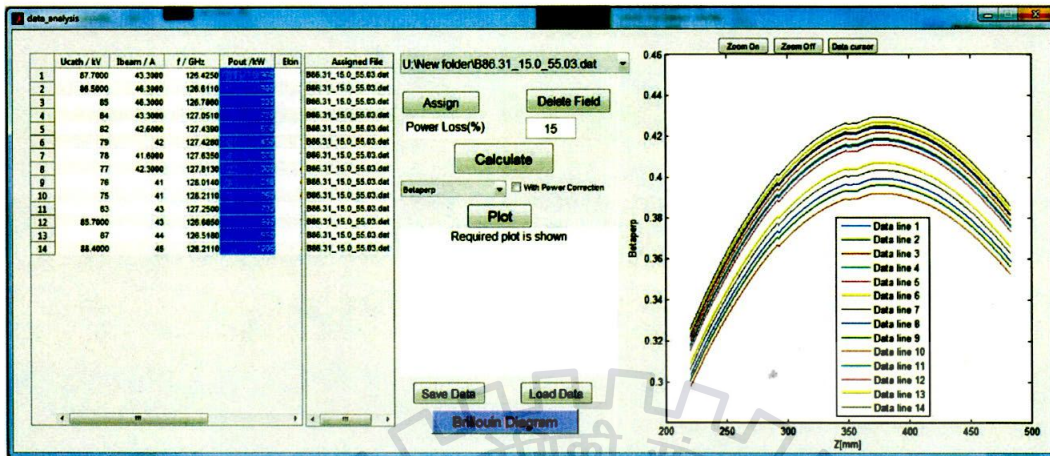


Figure 4.3: Data Analysis window showing plot of  $\beta_{\perp}$  without power correction along geometry of gyrotron.

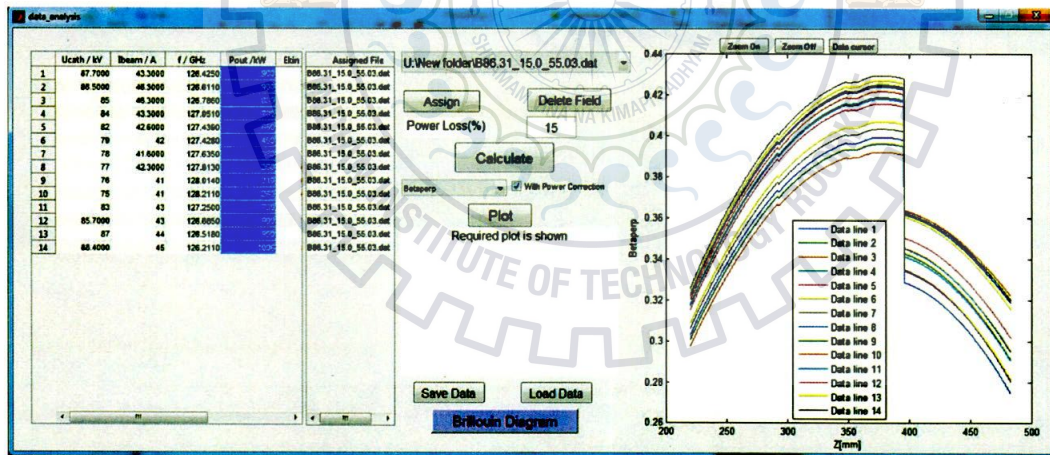


Figure 4.4: Plot of  $\beta_{\perp}$  with power correction along geometry of gyrotron.

- After doing calculations we can save the parameters in a file by using **Save**.
- We can load that saved file whenever we require by using **Load** and choosing that particular file.

## 4.4 Brillouin Diagram Window

On clicking **Brillouin Diagram**, the 3rd window will open as shown in Figure 4.5.

- We can plot 3 things here, i.e, **Hyperbola**, **Beam Lines** and **Resonance points**, depending upon the selection.
- A **Slider** is provided to set the value of  $Z$  in the geometry of Gyrotron.
- For plotting a hyperbola we have to give the eigenvalue ( $\chi$ ).
- We can set the range of  $k_{\parallel}$  by using either **Manual** or **Automatic** mode. In the manual mode, we can change the  $k_{\parallel}$  range externally or it will take default values while in the automatic mode, tool itself set the  $k_{\parallel}$  range as 1.5 times of maximum and minimum values.
- A frequency Offset is provided to shift the graph as per our requirement and can be used to take into account that the gyrotron interaction band has a certain width.
- Beam lines and resonance points are plotted according to the highlighted data lines in **Data Analysis** window.
- Can also import the  $\chi$  and  $Z$  value by using Push the extracted parameters. This button is to pull the settings from the next window, i.e. **Data Fitting** to easily get the suitable  $(\chi, Z)$  combination to fit in the present window.

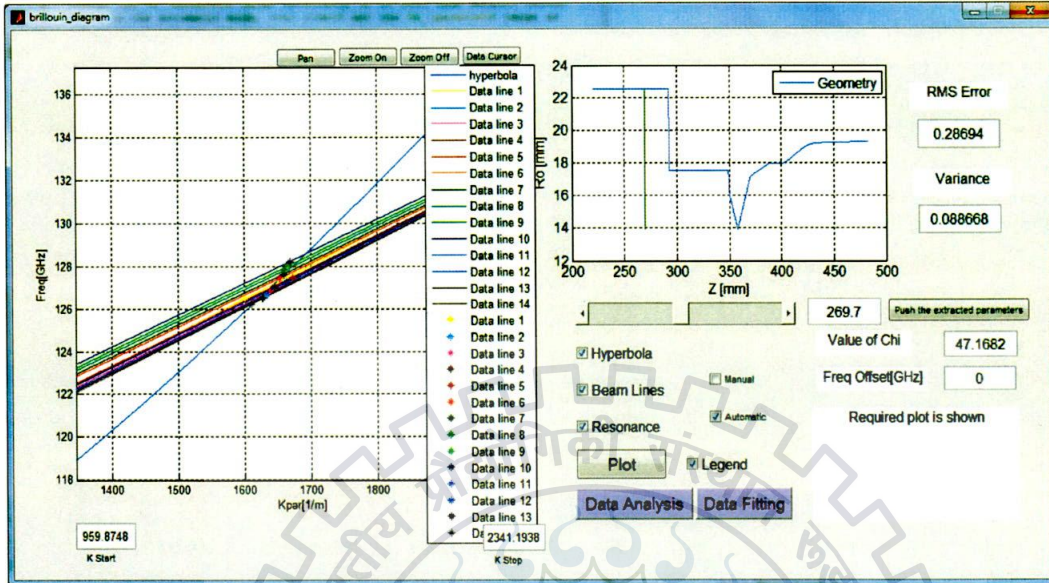


Figure 4.5: Brillouin Diagram window showing plot of hyperbola, beam lines and resonance points.

## 4.5 Data Fitting Window

On clicking **Data Fitting**, 4th window will open as shown in Figure 4.6.

- **Calculate Chi** First calculate the eigen values for all data lines.
- **Calculate Variance** Then calculate variance depending upon the data selection in **Data Analysis**.
- **Plot** It will plot the  $\chi$  values and variance along the geometry as presented in Figure 4.7.

The variation in eigenvalue curve among different data lines is calculated.

- A table shows the local minima points along RMS deviation and variance curve.

- The data of selected row can be exported to the third window for plotting Brillouin diagram according to that.

- Data with respect to the data cursor can also be exported by using

Extract Parameters from Data Cursor

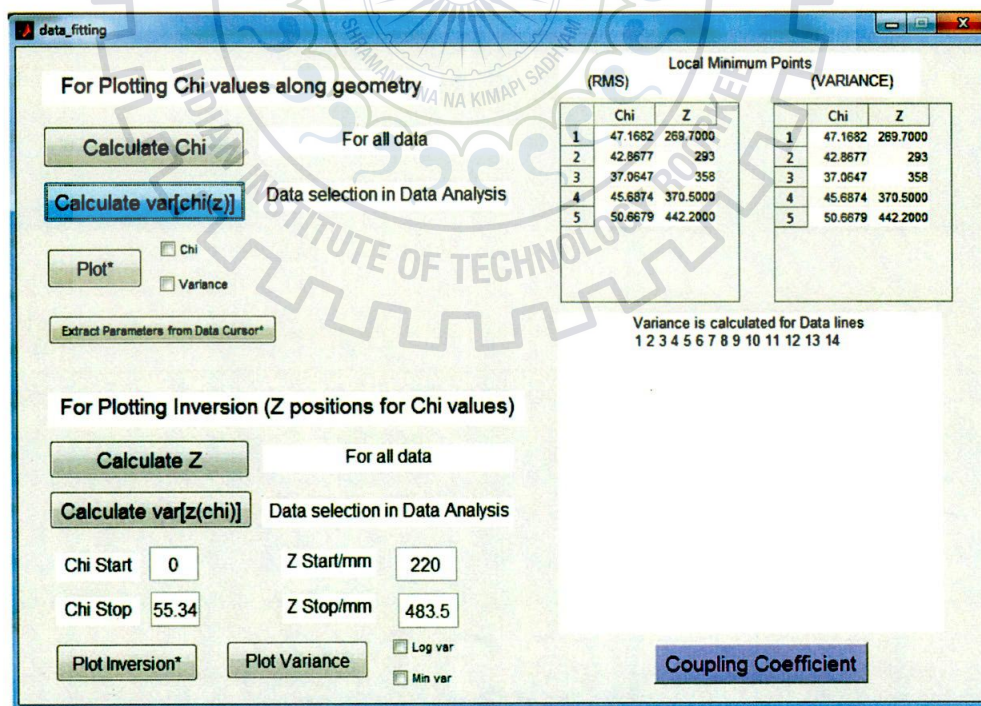


Figure 4.6: Data Fitting window showing minima points along RMS deviation and variance curve.

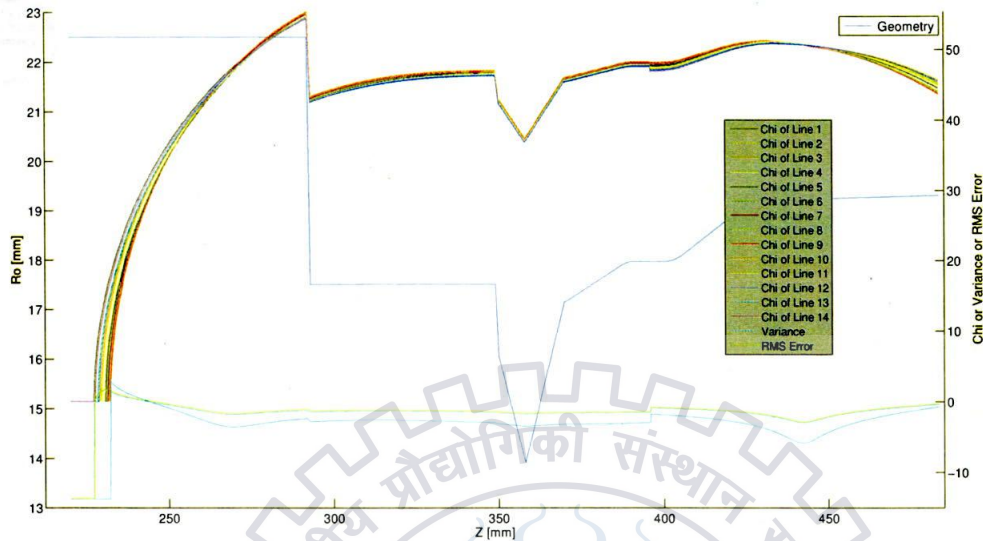


Figure 4.7: Plot of  $\chi$  values and variance along the geometry

We do following steps for plotting inversion curve.

- **Calculate Z** Calculate the values of  $Z$  depending on the  $\chi$  range given by user.
- **Calculate Variance** Then calculate variance of  $Z$  values for each  $\chi$  value.
- **Plot Inversion** and **Plot Variance** Gives the following plots shown in Figure 4.8 and 4.9 respectively. In general, **Plot Variance** will give linear plot while by choosing **Log var**, will give logarithmic plot, **Min var** will give plot of points having minimum variance and choosing both will give logarithmic plot of points having minimum variance.



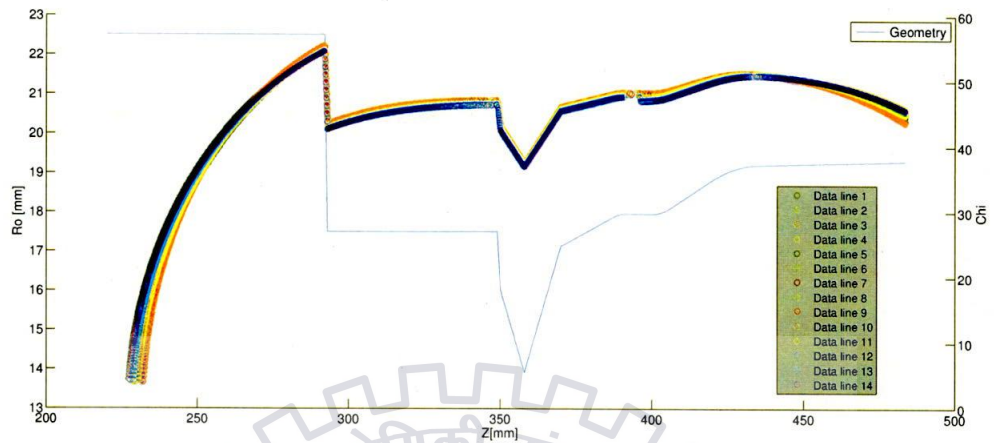


Figure 4.8: Plot of Z values corresponding to the  $\chi$  range.

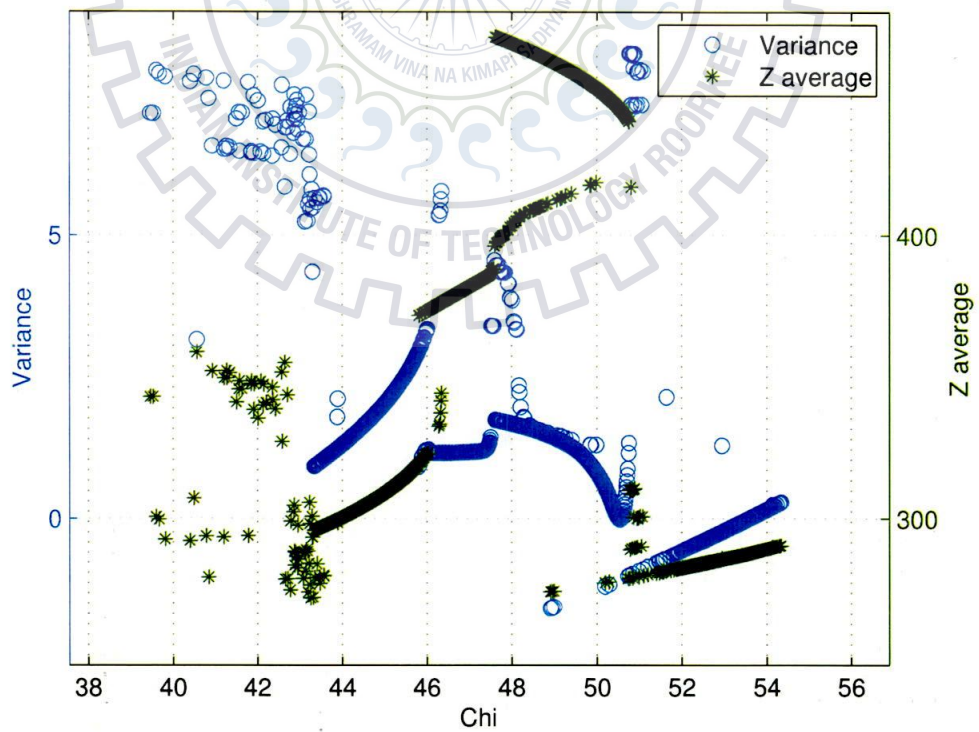


Figure 4.9: Plot of minimum variance of Z and average Z value for each  $\chi$  value

## 4.6 Coupling Coefficient Window

On clicking **Coupling Coefficient**, the 5th window will open as shown in Figure 4.10.

- Choose the  $Z$  value at which we want to find the possible modes which can exist.
- Depending on the  $Z$  value, it will give us the possible range of  $\chi$  values.
- Also provides the possible modes which can exist.
- We can also change the range of Chi and get the corresponding modes using .
- Then we can select the mode and get the coupling coefficient variation along  $Z$ .
- will give us the maximum and minimum coupling coefficient variation along  $Z$ .

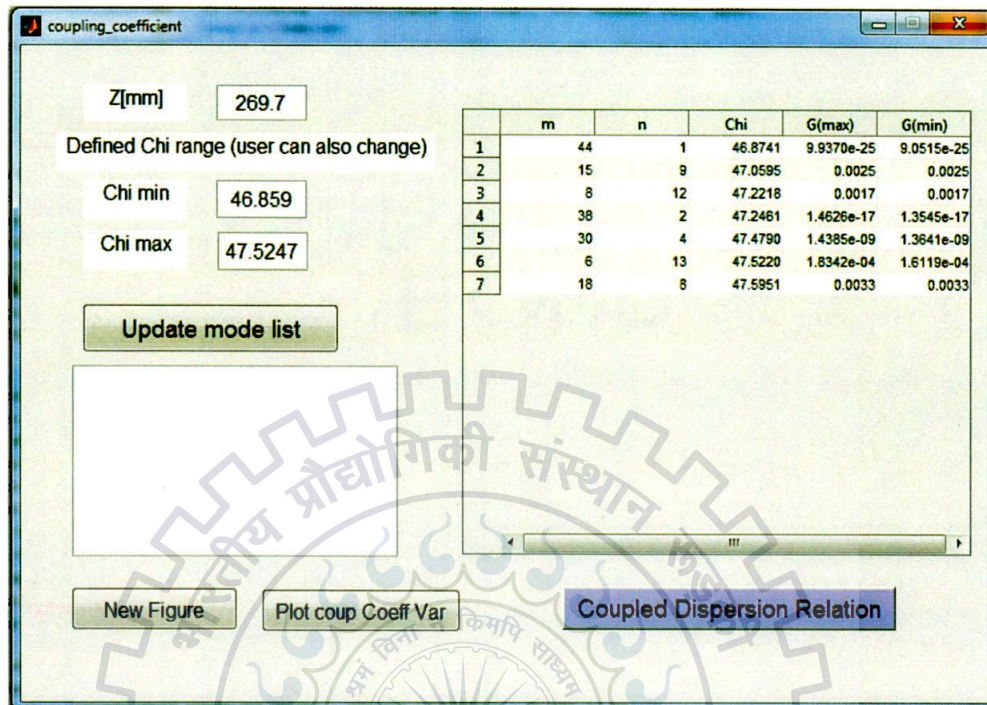


Figure 4.10: Fifth Window showing different modes depending on a  $\chi$  range for a particular  $Z$  position.

## 4.7 Coupled Dispersion Relation Window

On clicking **Coupled Dispersion Relation**, 6th window will open as shown in Figure 4.11.

- Choose the mode and the  $Z$  position where we want to check the sustainability of the relation.
- When we hit the **Calculate** button of left hand side it will calculate relation for all data lines according to the loaded file.
- We can change the  $k_{||}$  range and the step size, otherwise it will take the default values.
- Then we can plot each data line using **Plot**. After hitting, the related data will appear in the right hand side of the window.

- We can also change the fields of the data i.e.,  $\beta_{||}$ ,  $\beta_{\perp}$ ,  $E_{kin}$ ,  $R_0$ ,  $R_e$ ,  $I_b$ , and  $BM$  (Magnetic field), and calculate according to the provided data.
- The following results will be displayed on the window, i.e.
  - Maximum possible interaction frequency
  - Minimum possible interaction frequency
  - Approximate possible interaction frequency
  - Interaction frequency according to the Cold Dispersion Relation.

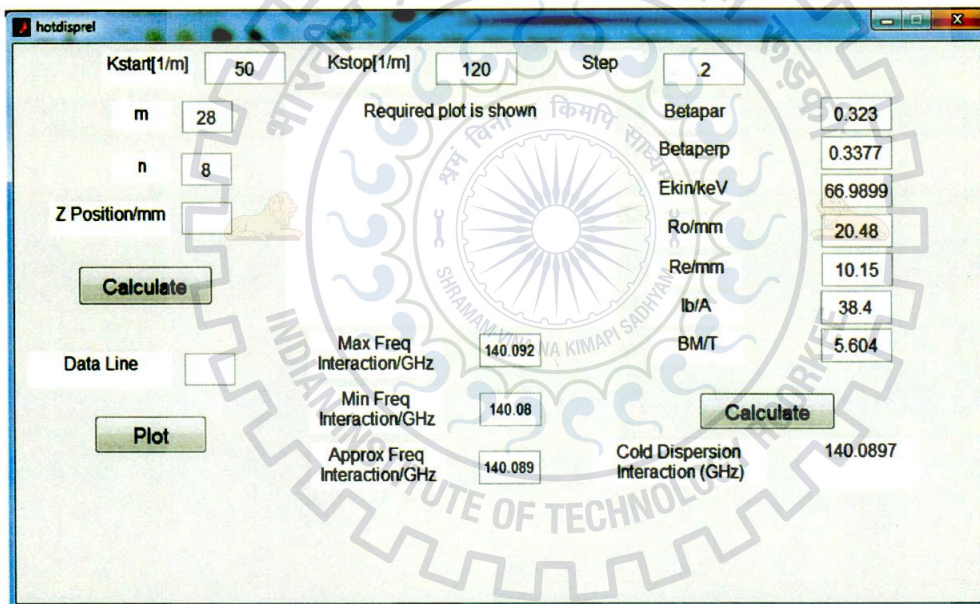


Figure 4.11: Coupled Dispersion Relation Window.

# Chapter 5

## Analysis Results

### 5.1 Overview

In this chapter, the results and outcomes of the tool are discussed. We will discuss different sets of measurements, each consisting of a set of measured parasitic frequencies in the KIT step-tunable gyrotron [29]. More details about measurement system are provided in [30]. Discussed measurement data examples:

- Sweeping magnetic field.
- Sweeping cathode voltage.
- Sweeping cathode voltage along with  $P_{out}$  measurement.

Simulations using the “Brillouin Analysis Tool” give the electron beam parameters in the whole gyrotron geometry (that means along the  $Z$  axis). We now want to find out where the oscillations come from. If we knew where that would be, we could take the beam parameters in that  $Z$  position, and the measured frequency points should fit on the hyperbola of one mode. By this at least the eigenvalue of that mode can be identified. Since we don't know, we simply have to try many positions till we find one which provides the best fit.

## 5.2 Results and Discussion on loacting the position and mode for parasitic oscillations

### 5.2.1 Case 1

Here we discuss the results coming from the tool when we are considering variation along magnetic field in the measurement data. Data file for 140 GHz Gyrotron is given in the Table 5.1 and its constraints are given in the Table 5.2. In this measurement, parasites are in the range of 129–130 GHz.

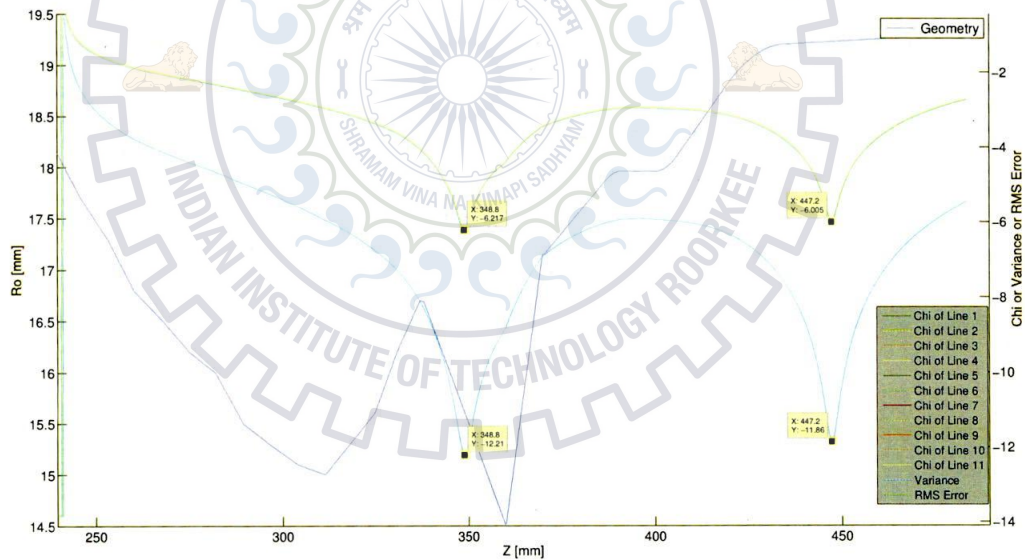
Table 5.1: Cathode voltage, beam current, frequency, output power, kinetic energy, alpha, beam radius, and assigned magnetic profile for a 140 GHz gyrotron.

Measurement data				Simulation data			
$U_0$	$I_b$	f	$P_{out}$	$E_{kin}$	$\alpha$	$R_b$	B file
kV	A	GHz	kW	keV		mm	
74.3	39	129.435	0	67.51	1.438	8.013	B92.80_35.22.dat
74.3	39	129.415	0	67.51	1.438	8.013	B92.77_35.22.dat
74.3	39	129.395	0	67.51	1.438	8.013	B92.72_35.22.dat
74.3	39	129.381	0	67.51	1.438	8.013	B92.66_35.22.dat
74.3	39	129.361	0	67.51	1.438	8.013	B92.62_35.22.dat
74.3	39	129.348	0	67.51	1.438	8.013	B92.57_35.22.dat
74.3	39	129.328	0	67.51	1.438	8.013	B92.52_35.22.dat
74.3	39	129.314	0	67.51	1.438	8.013	B92.47_35.22.dat
74.3	39	129.294	0	67.51	1.438	8.013	B92.42_35.22.dat
74.3	39	129.274	0	67.51	1.438	8.013	B92.36_35.22.dat
74.3	39	129.247	0	67.51	1.438	8.013	B92.32_35.22.dat

Table 5.2: Gyrotron constraints

Mode	TE <sub>22,8</sub>
Geometry Cavity Center ( $z_{G\_cavityCenter}/mm$ )	395.7
Magnetic Field Cavity center ( $z_{B\_cavityCenter}/mm$ )	395.16
Reference Position ( $z_{B\_refPos}/mm$ )	394.5

Based on the available data, we have calculated the eigen values along the whole geometry, and also their root mean square error and variance between different data lines. Their curves can be seen in  $\chi$  RMS and Variance plot which is given in Figure 5.1.

Figure 5.1:  $\chi$  RMS and Variance plot.

Plot shows several local minima points in RMS value of  $\chi$  which are given in Table 5.3, also local minima points in Variance curve of  $\chi$  given in Table 5.4. Taking only variance minimas into our consideration, Brillouin diagram for Variance minimum 1) and minimum 2) are shown in Figure 5.2 and in Figure 5.3 respectively.

Table 5.3: Local minima points in RMS value of  $\chi$

	$\chi$	Z	$\log(\text{RMS}+(1e-6))$
1	42.1119	348.8000	-6.217
2	51.8882	447.2000	-6.005

Table 5.4: Local minima points in Variance curve of  $\chi$

	$\chi$	Z	$\log(\text{var}+(1e-6))$
1	42.1119	348.8000	-12.21
2	51.8882	447.2000	-11.86

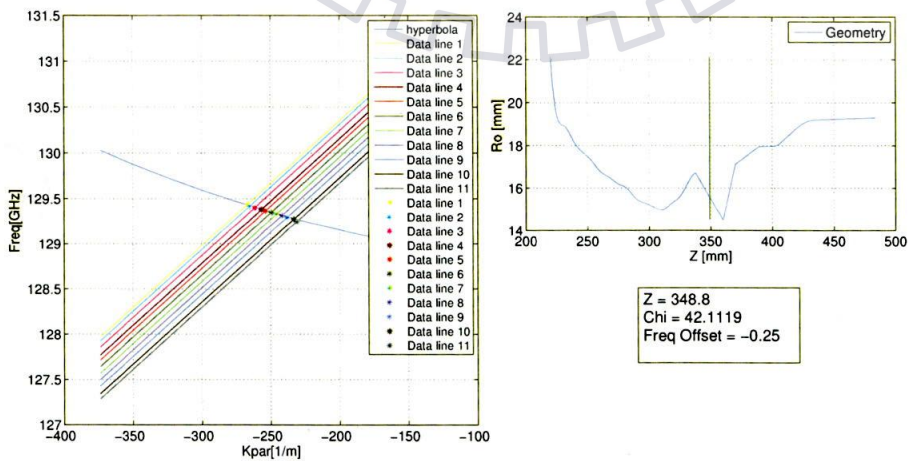


Figure 5.2: Brillouin Diagram for Variance minimum 1).



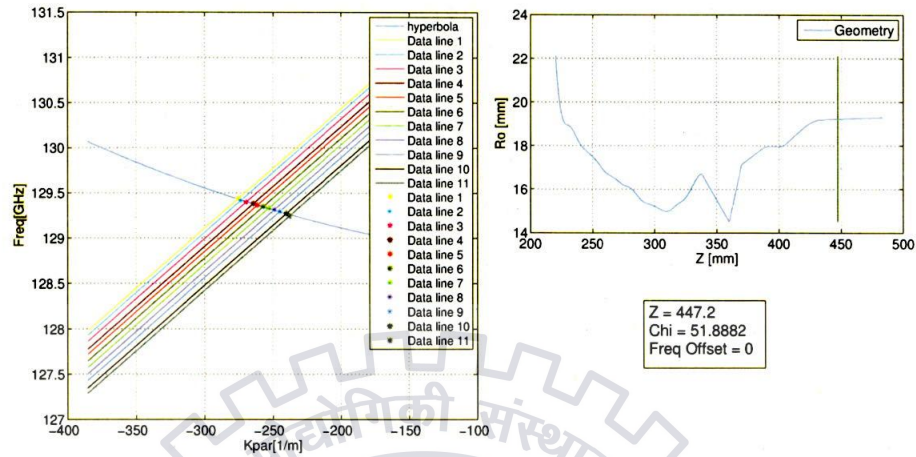


Figure 5.3: Brillouin Diagram for Variance minimum 2).

We are getting best fit at  $Z=348.8$  and  $Z=447.2$ . As we are using frequency offset, so on increasing the range of  $\chi$  value we are getting several approximate modes. First taking  $Z = 348.8$  and  $\chi$  range between 41.5-42.5, expected modes and their coupling coefficients are given in Table 5.5. On seeing the table, we came to know that mode  $TE_{19,6}$  and  $TE_{22,5}$  are giving best results. Coupling coefficient variation along  $Z$  axis for mode  $TE_{19,6}$  is shown in Figure 5.4 and for mode  $TE_{22,5}$  is shown in Figure 5.5.

Table 5.5: Expected modes and their coupling coefficients at  $Z=348.8$  and  $\chi$  range between 41.5-42.5.

m	n	$\chi$	G(max)	G(min)
2	13	41.5689	0.0017	0.0017
0	13	41.6171	0.0016	0.0016
16	7	41.6433	1.8977e-04	1.8964e-04
25	4	41.7206	4.3477e-04	4.3472e-04
11	9	41.7286	0.0019	0.0019
39	1	41.7623	1.5916e-14	1.5911e-14
33	2	41.8754	3.4337e-09	3.4328e-09
19	6	41.9446	0.0057	0.0057
22	5	41.9879	0.0045	0.0045
29	3	42.1626	3.7194e-06	3.7187e-06
9	10	42.2246	2.2269e-05	2.2215e-05
14	8	42.4259	1.8259e-04	1.8244e-04
7	11	42.6115	0.0023	0.0023

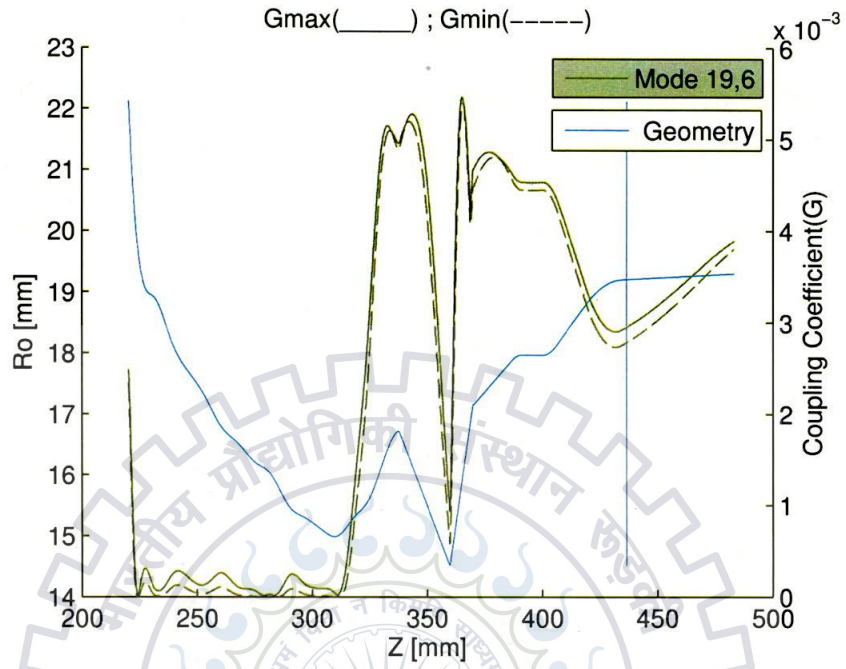


Figure 5.4: Coupling coefficient variation along Z axis for mode  $TE_{19,6}$

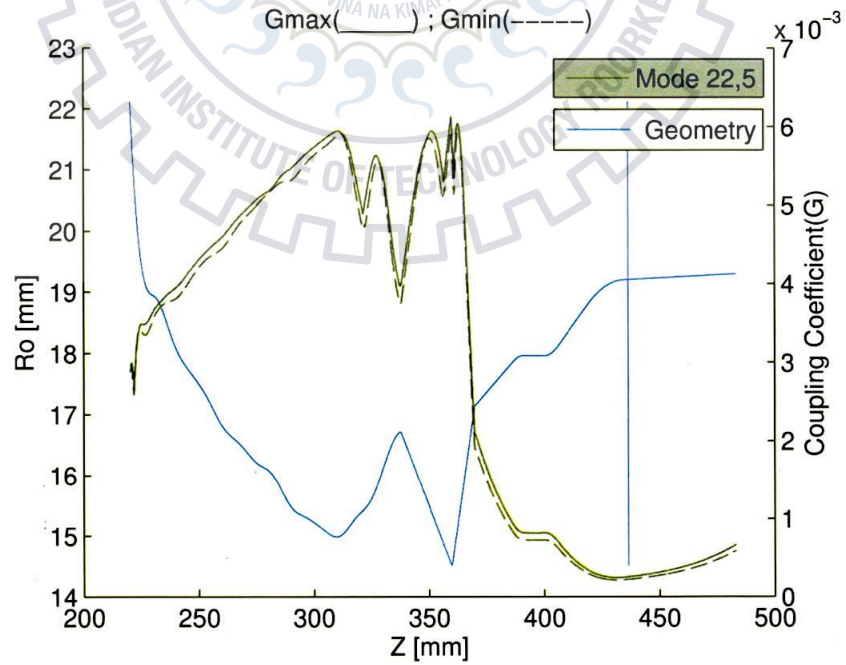


Figure 5.5: Coupling coefficient variation along Z axis for mode  $TE_{22,5}$

Since there is no power measurement data, so no power correction is made. Because of this, the minima found at  $Z > Z_{cavity}$  are not worth very much but for the sake of explanation, we have discussed this minima also. Expected modes and their coupling coefficients at  $Z=447.2$  and  $\chi$  range between 51.3-52.3 is given in Table 5.6. Similarly, mode  $TE_{21,8}$  and  $TE_{19,9}$  are giving best results, so coupling coefficient variation along Z axis for mode  $TE_{21,8}$  is shown in Figure 5.6 and for mode  $TE_{19,9}$  is shown in Figure 5.7.

Table 5.6: Expected modes and their coupling coefficients at  $Z=447.2$  and  $\chi$  range between 51.3-52.3.

m	n	$\chi$	G(max)	G(min)
21	8	51.4014	0.0044	0.0044
11	12	51.4331	0.0016	0.0016
30	5	51.4364	4.1416e-07	4.1410e-07
42	2	51.5214	6.4481e-18	6.4467e-18
24	7	51.6394	9.5860e-04	9.5854e-04
27	6	51.6629	3.8370e-05	3.8367e-05
16	10	51.6874	1.9634e-05	1.9610e-05
9	13	51.8308	8.2470e-06	8.2295e-06
49	1	51.9778	1.7738e-25	1.7733e-25
34	4	52.0361	5.5829e-10	5.5820e-10
7	14	52.1438	0.0020	0.0020
38	3	52.1517	1.5903e-13	1.5900e-13
19	9	52.2612	0.0045	0.0045
14	11	52.2993	2.1066e-04	2.1057e-04
5	15	52.3756	0.0018	0.0018

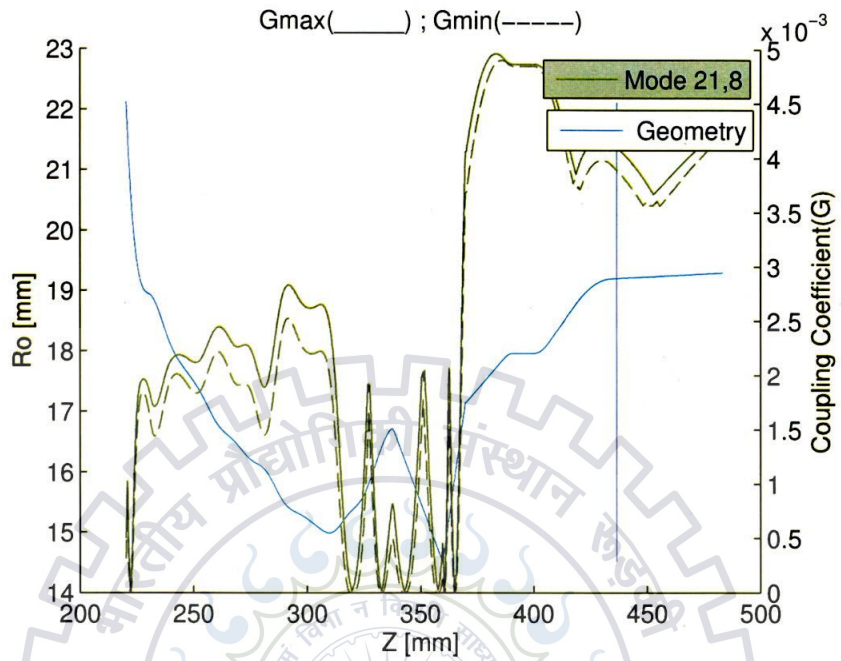


Figure 5.6: Coupling coefficient variation along Z axis for mode TE<sub>21,8</sub>

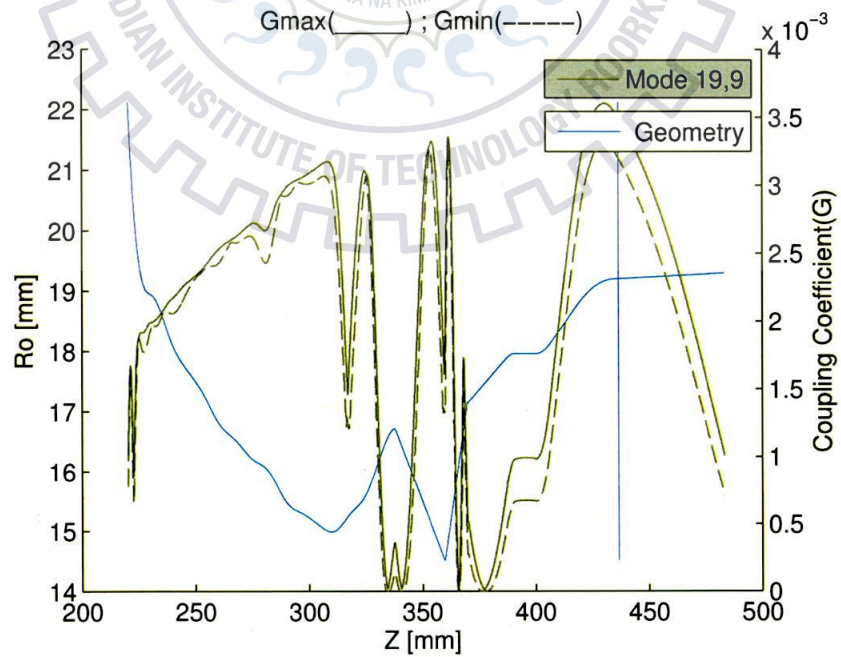


Figure 5.7: Coupling coefficient variation along Z axis for mode TE<sub>19,9</sub>

### 5.2.2 Case 2

We discuss the results coming from the tool when we are considering variation along cathode voltage in the measurement data. The data file for 140 GHz gyrotron is given in the Table 5.7 and its constraints are given in the Table 5.8. In this measurement, parasites are in the range of 116–117 GHz. The variation in measured frequency along variation in cathode voltage is presented in Figure 5.8.

Table 5.7: Cathode voltage, beam current, frequency, output power, kinetic energy, alpha, beam radius, and assigned magnetic profile for a 140 GHz gyrotron.

Measurement data				Simulation data			
$U_0$	$I_b$	f	$P_{out}$	$E_{kin}$	$\alpha$	$R_b$	B file
kV	A	GHz	kW	keV		mm	
75.7	38.4	116.789	0	70.42	1.132	8.47	B86.22-36.22.dat
76.3	38.4	116.742	0	71.01	1.140	8.47	B86.22-36.22.dat
77	38.4	116.702	0	71.71	1.149	8.46	B86.22-36.22.dat
77	38.4	116.661	0	71.71	1.149	8.46	B86.22-36.22.dat
77	38.4	116.621	0	71.71	1.149	8.46	B86.22-36.22.dat
77.7	38.7	116.581	0	72.39	1.156	8.43	B86.22-36.22.dat
78.3	38.7	116.548	0	73.02	1.163	8.49	B86.22-36.22.dat
79	38.7	116.5	0	73.72	1.171	8.48	B86.22-36.22.dat
79.7	38.7	116.46	0	74.41	1.178	8.46	B86.22-36.22.dat
79.7	39.2	116.417	0	74.30	1.176	8.46	B86.22-36.22.dat
80.3	39.2	116.375	0	74.91	1.181	8.46	B86.22-36.22.dat
81	39.2	116.334	0	75.62	1.187	8.46	B86.22-36.22.dat
81.7	39.2	116.28	0	76.32	1.192	8.46	B86.22-36.22.dat
81.7	39.2	116.24	0	76.32	1.192	8.46	B86.22-36.22.dat

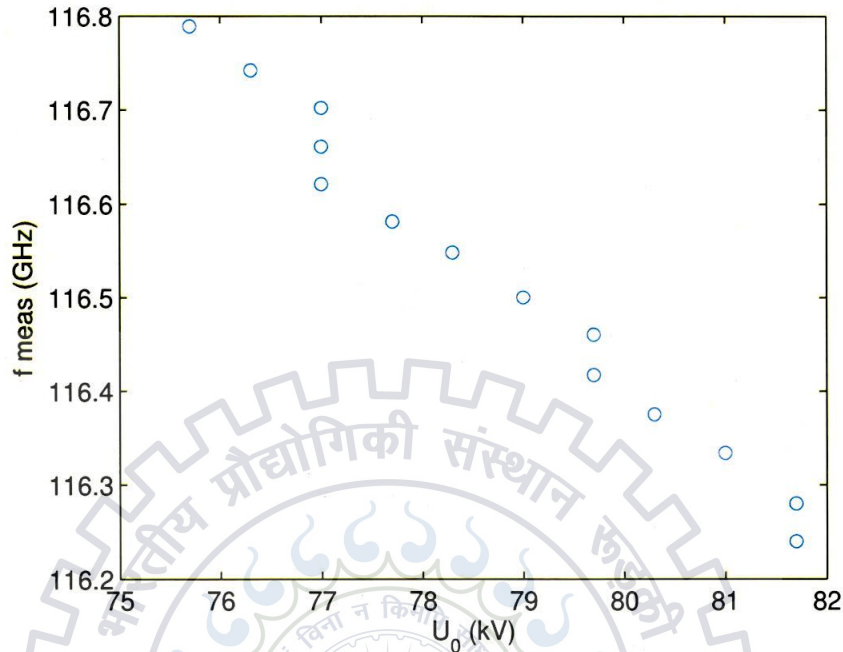


Figure 5.8: Data plot

Table 5.8: Gyrotron constraints

Mode	TE <sub>22,7</sub>
Geometry Cavity Center ( $zG\_cavityCenter/mm$ )	395.7
Magnetic Field Cavity center ( $zB\_cavityCenter/mm$ )	395.16
Reference Position ( $zB\_refPos/mm$ )	394.5

Based on the available data, we have calculated the eigen values along the whole geometry, and also their root mean square error and variance between different data lines. Their curves can be seen in  $\chi$  RMS and Variance plot is given in Figure 5.9.

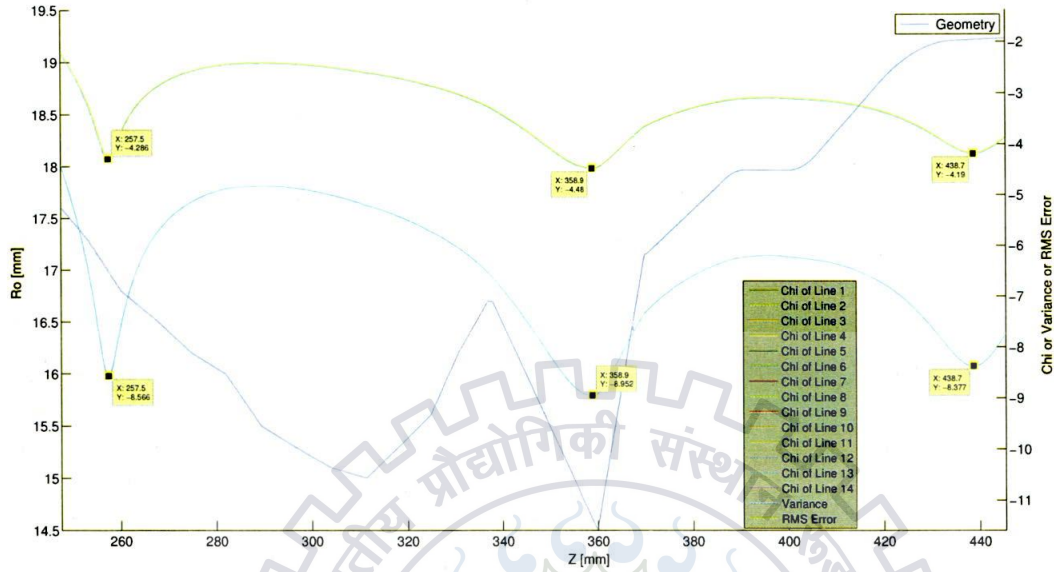


Figure 5.9:  $\chi$  RMS and Variance plot.

Plot shows several local minima points in RMS value of  $\chi$  as given in Table 5.9, also local minima points in variance curve of  $\chi$  given in Table 5.10. Taking only variance minimas into our consideration, Brillouin diagram for variance minimum 1), minimum 2) and minimum 3) are shown in Figure 5.10, in Figure 5.11 and in Figure 5.12 respectively.

Table 5.9: Local minima points in RMS value of  $\chi$

	$\chi$	Z	$\log(\text{RMS}+(1e-6))$
1	29.2142	257.5000	-4.286
2	34.8215	358.9000	-4.48
3	45.8921	438.7000	-4.19



Table 5.10: Local minima points in variance curve of  $\chi$

	$\chi$	Z	$\log(\text{var}+(1e-6))$
1	29.2142	257.5000	-8.568
2	34.8215	358.9000	-8.952
3	45.8921	438.7000	-8.377

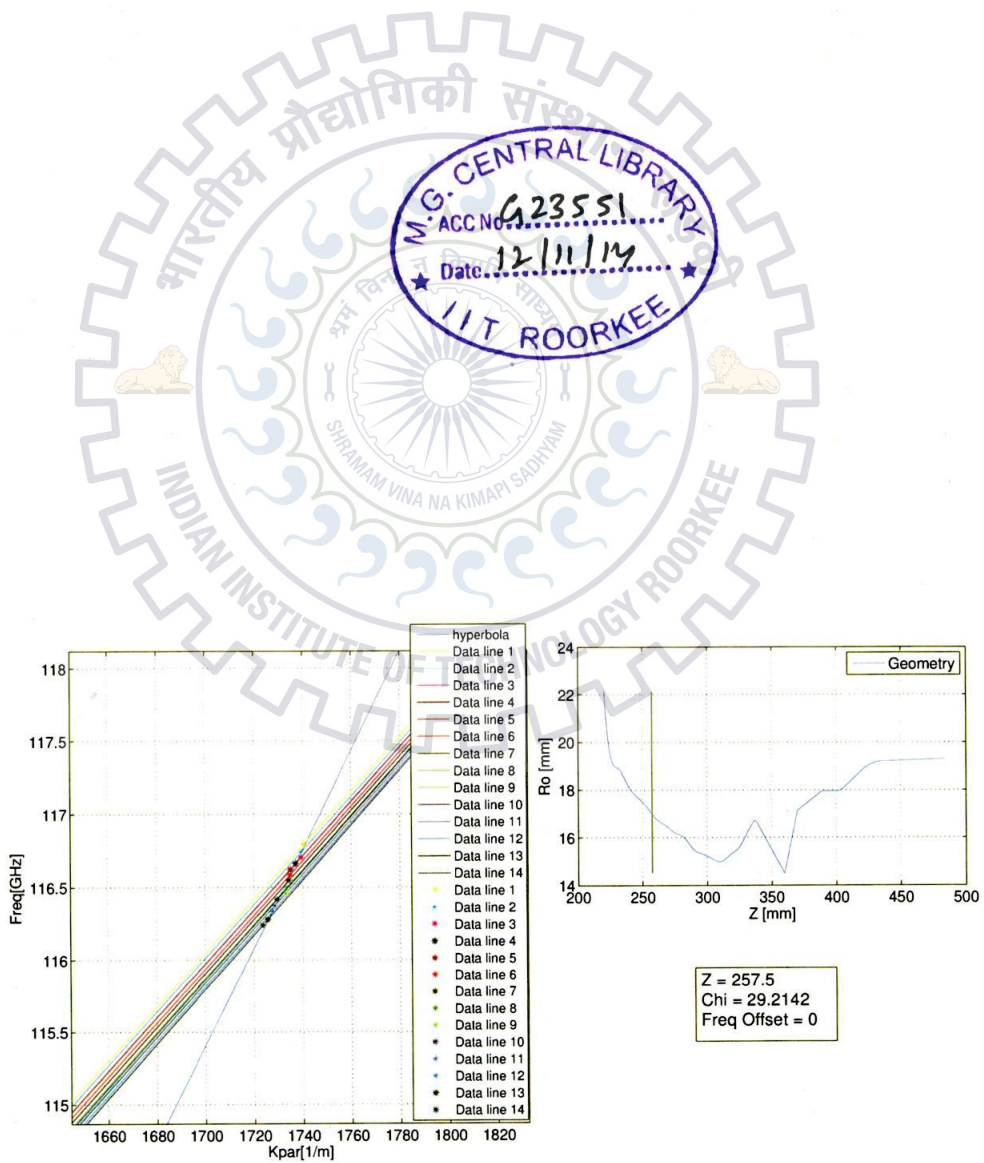


Figure 5.10: Brillouin Diagram for variance minimum 1).

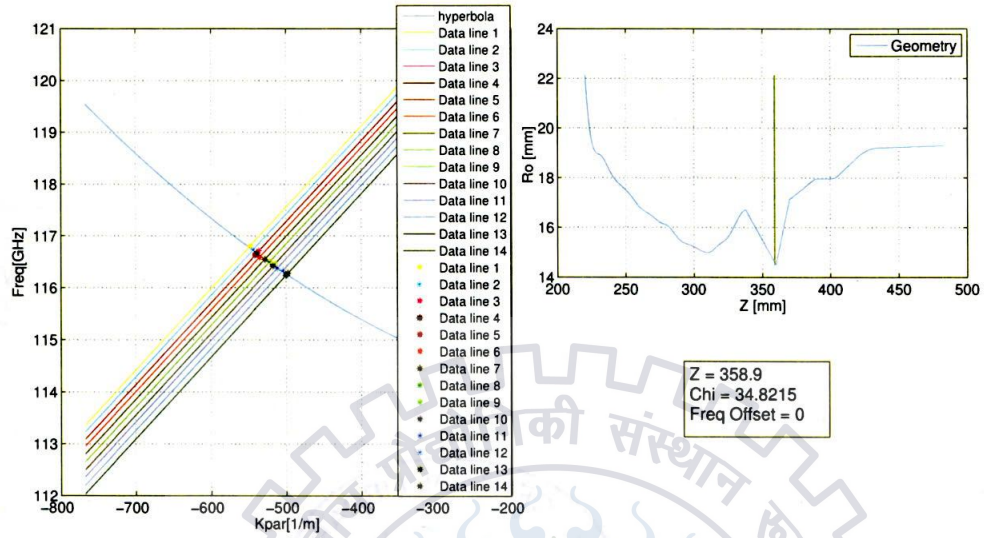


Figure 5.11: Brillouin Diagram for variance minimum 2).

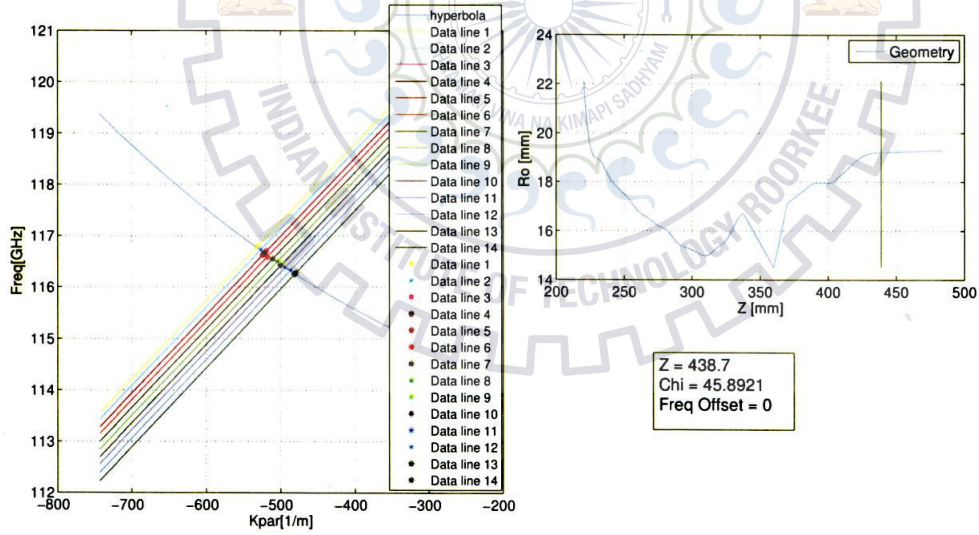


Figure 5.12: Brillouin Diagram for variance minimum 3).

All the minima points are giving good results, i.e., at  $Z=257.5000$ ,  $Z=358.9000$  and  $Z=438.7000$ . As we are using frequency offset, so on increasing the range of  $\chi$  value we are getting several approximate modes. First taking  $Z=257.5$  and  $\chi$  range between 28.5-29.5, expected modes and their coupling coefficients are given in Table 5.11. On seeing the table, we came to know that mode  $TE_{0,9}$  and  $TE_{14,4}$  are giving best results. coupling coefficient variation along  $Z$  axis for mode  $TE_{0,9}$  Figure 5.13 and for mode  $TE_{14,4}$  are shown in Figure 5.14.

Table 5.11: Expected modes and their coupling coefficients at  $Z=257.5$  and  $\chi$  range between 28.5-29.5.

m	n	$\chi$	G(max)	G(min)
17	3	28.5114	0.0040	0.0039
14	4	28.6943	0.0038	0.0037
4	8	28.7678	0.0018	0.0018
21	2	28.8156	2.4469e-04	2.1253e-04
2	9	28.9777	0.0018	0.0018
0	9	29.0468	0.0017	0.0017
9	6	29.2186	0.0021	0.0020
27	1	29.4482	8.0496e-08	6.2445e-08
18	3	29.6701	0.0037	0.0036

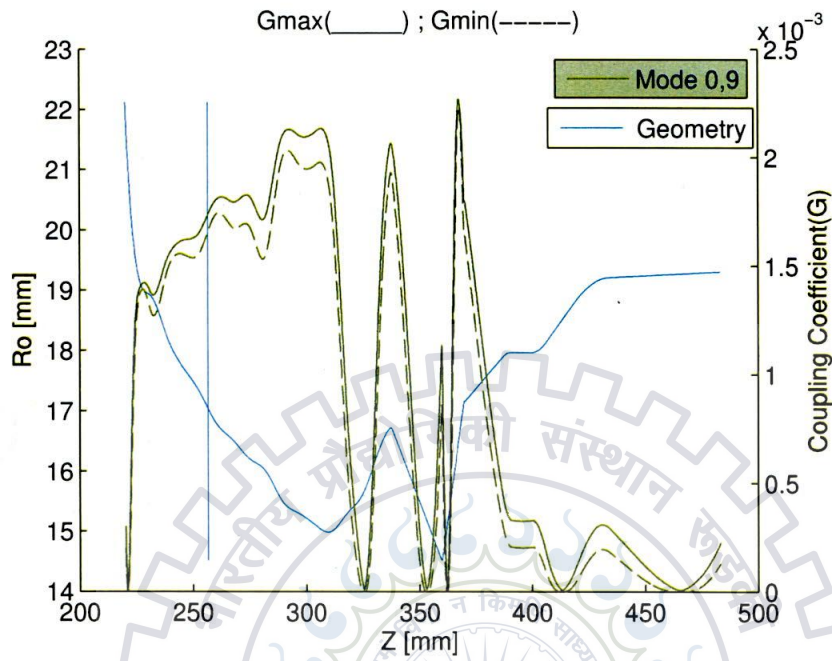


Figure 5.13: Coupling coefficient variation along Z axis for mode TE<sub>0,9</sub>

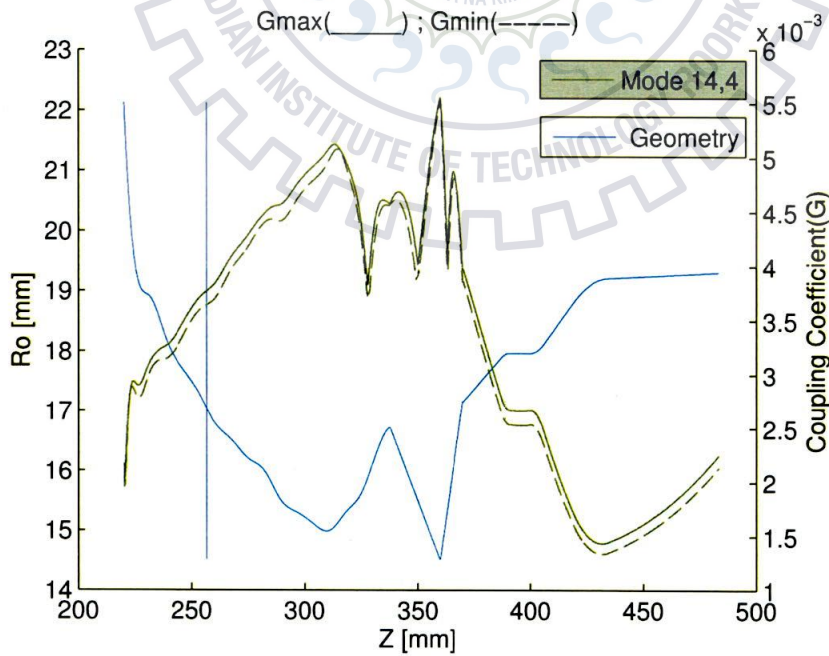


Figure 5.14: Coupling coefficient variation along Z axis for mode TE<sub>14,4</sub>

Similarly, expected modes and their coupling coefficients at  $Z=358.9$  and  $\chi$  range between 34.2-35.3 are given in Table 5.12. Mode  $TE_{0,11}$  and  $TE_{11,7}$  are giving best results, so coupling coefficient variation along  $Z$  axis for mode  $TE_{22,3}$  Figure 5.15, for mode  $TE_{0,11}$  Figure 5.16 and for mode  $TE_{11,7}$  are shown in Figure 5.17.

Table 5.12: Expected modes and their coupling coefficients at  $Z=358.9$  and  $\chi$  range between 34.2-35.3.

m	n	$\chi$	G(max)	G(min)
22	3	34.2608	0.0015	0.0013
26	2	34.2930	1.6065e-05	1.3059e-05
8	8	34.3966	9.8172e-04	6.6087e-04
13	6	34.4145	8.9001e-04	5.8075e-04
32	1	34.5885	1.1485e-09	8.3752e-10
19	4	34.6915	0.0061	0.0061
16	5	34.7125	0.0042	0.0038
6	9	34.8134	0.0026	0.0025
4	10	35.1039	0.0026	0.0026
11	7	35.1667	0.0029	0.0026
2	11	35.2755	0.0021	0.0019
0	11	35.3323	0.0022	0.0019

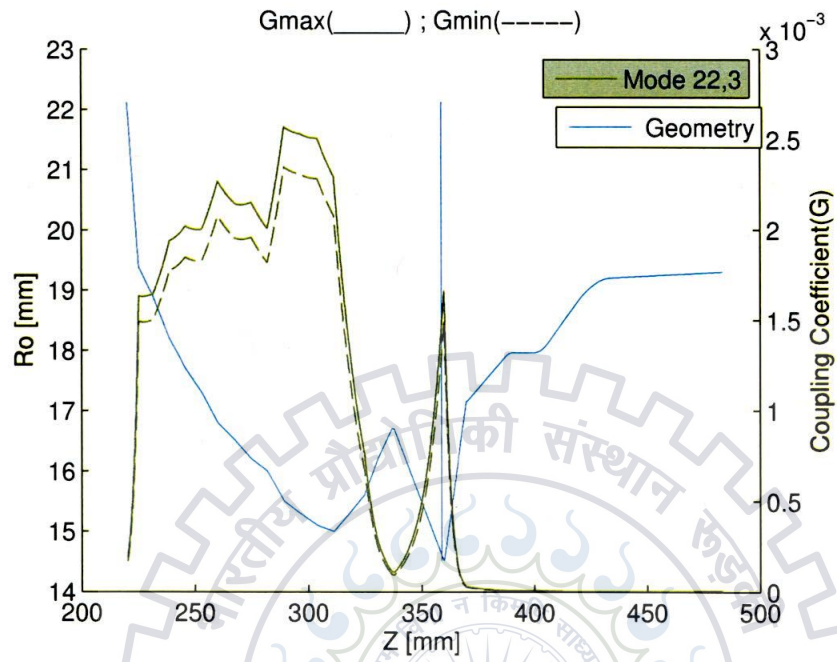


Figure 5.15: Coupling coefficient variation along Z axis for mode TE<sub>22,3</sub>

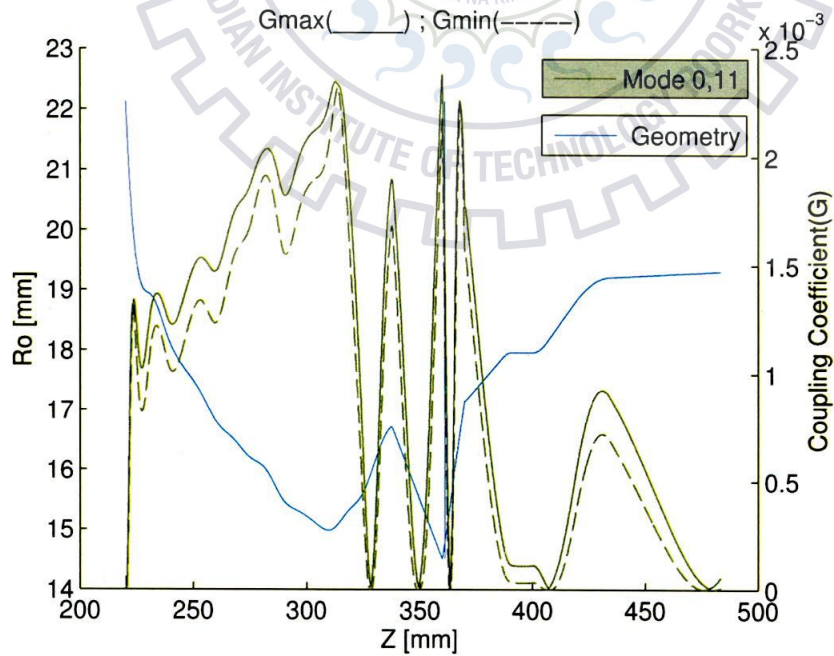


Figure 5.16: Coupling coefficient variation along Z axis for mode TE<sub>0,11</sub>

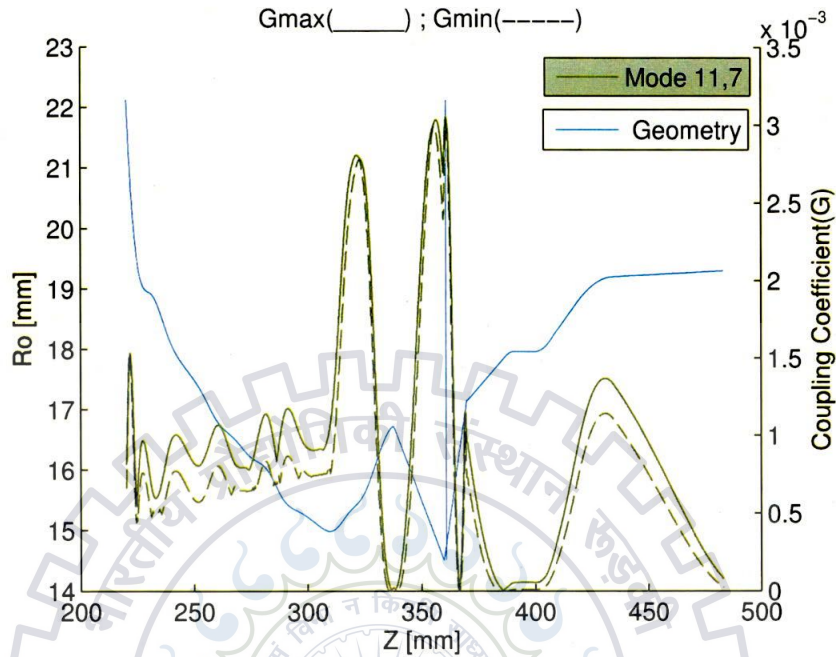


Figure 5.17: Coupling coefficient variation along Z axis for mode  $TE_{11,7}$

Since there is no power measurement data, so no power correction is made. Because of this, the minima found at  $Z > Z_{cavity}$  are not worth very much but for the sake of explanation, we have discussed this minima also. Expected modes and their coupling coefficients at  $Z=436.2$  and  $\chi$  range between 45.5-46.4 are given in Table 5.13. Similarly, mode  $TE_{22,6}$  is giving good result. Coupling Coefficient Variation along Z axis for mode  $TE_{22,6}$  is shown in Figure 5.18 and plot of variance in Z as a function of  $\chi$  in Figure 5.19. Coupling coefficient variation along Z axis for mode  $TE_{17,8}$  is shown in Figure 5.20

Table 5.13: Expected modes and their coupling coefficients at  $Z=438.7$  and  $\chi$  range between 45.5-46.4

m	n	$\chi$	G(max)	G(min)
32	3	45.5102	4.6574e-10	3.3979e-10
25	5	45.5592	5.3229e-05	4.4366e-05
22	6	45.6243	0.0013	0.0011
14	9	45.7402	3.4935e-04	1.9541e-04
7	12	45.7940	8.6299e-05	1.2250e-05
43	1	45.8524	6.5409e-21	4.0117e-21
5	13	46.0586	2.0127e-04	1.2046e-04
37	2	46.1745	2.4319e-14	1.6391e-14
3	14	46.2330	7.3213e-05	6.7910e-06
17	8	46.3138	0.0040	0.0039
1	15	46.3196	5.1722e-04	2.9939e-04
29	4	46.3333	2.6218e-07	2.0277e-07
12	10	46.3378	0.0017	0.0014
33	3	46.6218	2.1991e-10	1.5862e-10



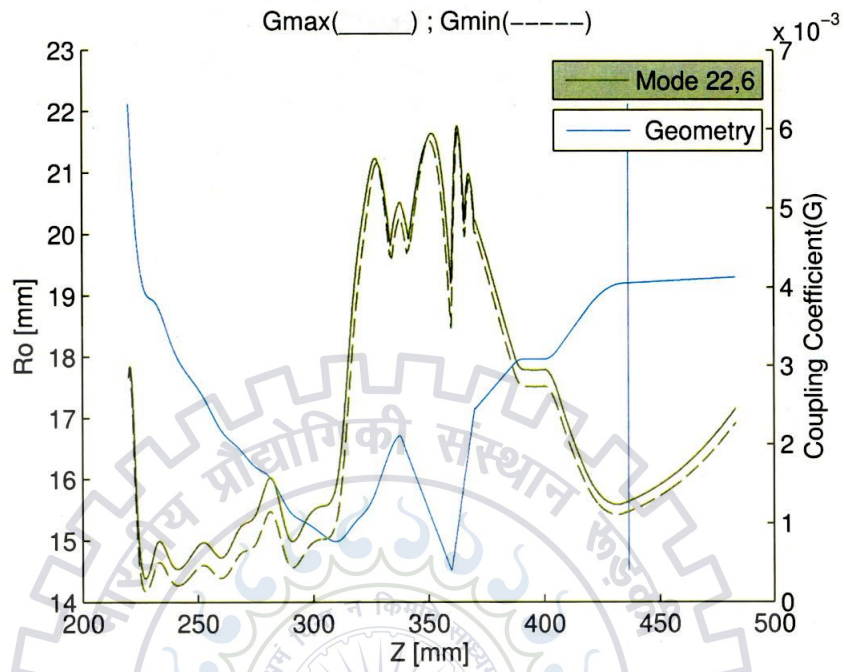


Figure 5.18: Coupling coefficient variation along Z axis for mode  $TE_{22,6}$

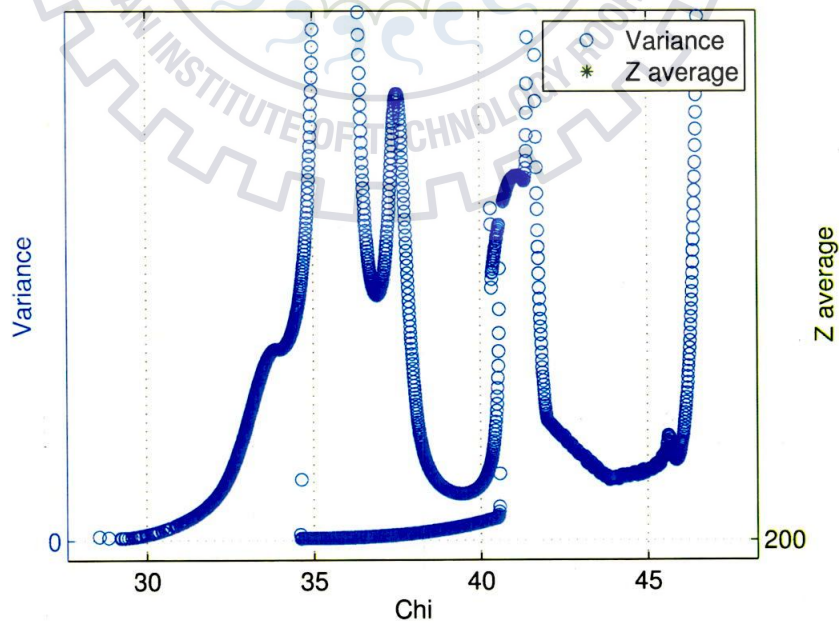


Figure 5.19: Plot of variance in Z as a function of  $\chi$ .

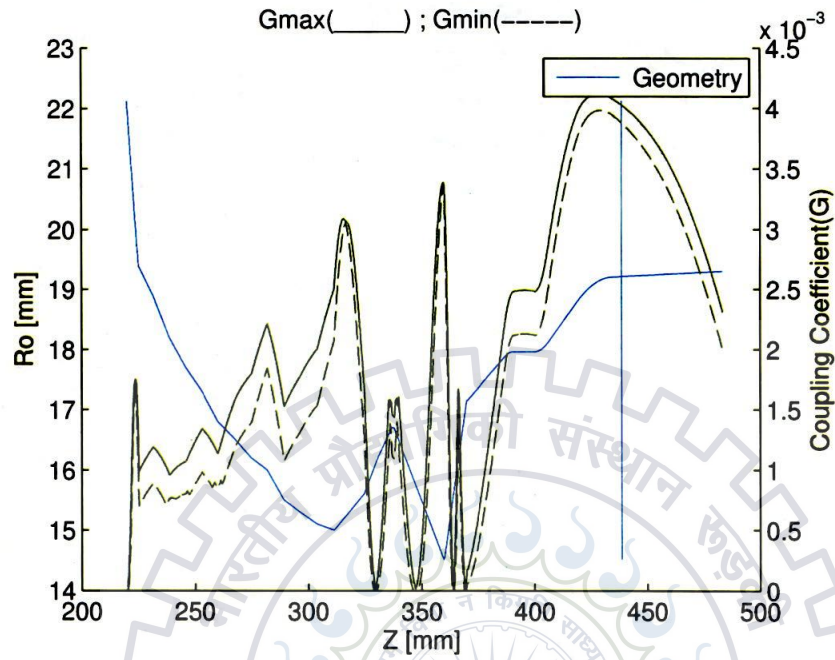


Figure 5.20: Coupling coefficient variation along Z axis for mode  $TE_{17,8}$

### 5.2.3 Case 3

We discuss the results coming from the tool when we are considering variation along cathode voltage in the measurement data also taking into account the value of  $P_{out}$ . Data file for 140 GHz gyrotron is given in the Table 5.14 and its constraints are given in the Table 5.15. In this measurement, parasites are in the range of 126–129 GHz. The variation in measured frequency along variation in cathode voltage is presented in 5.21 and also we can see the variation in measured output power.

Table 5.14: Cathode Voltage, Beam Current, Frequency, Output power, Kinetic energy, Alpha, Beam radius, and Assigned Magnetic profile for a 140 GHz gyrotron.

Measurement data				Simulation data			
$U_0$ kV	$I_b$ A	f GHz	$P_{out}$ kW	$E_{kin}$ keV	$\alpha$	$R_b$ mm	B file
87.7	43.3	126.425	960	78.90	1.541	8.29	B86.31_15.0_55.03.dat
86.5	46.3	126.611	900	78.722	1.541	8.280	B86.31_15.0_55.03.dat
85	46.3	126.786	830	77.157	1.542	8.280	B86.31_15.0_55.03.dat
84	43.3	127.051	780	76.12	1.541	8.280	B86.31_15.0_55.03.dat
82	42.6	127.439	650	74.70	1.536	8.287	B86.31_15.0_55.03.dat
79	42	127.428	450	71.764	1.51	8.287	B86.31_15.0_55.03.dat
78	41.6	127.635	380	70.83	1.496	8.287	B86.31_15.0_55.03.dat
77	42.3	127.813	360	69.720	1.478	8.287	B86.31_15.0_55.03.dat
76	41	128.014	310	68.97	1.462	8.286	B86.31_15.0_55.03.dat
75	41	128.211	260	68.00	1.441	8.288	B86.31_15.0_55.03.dat
83	43	127.25	730	75.66	1.539	8.280	B86.31_15.0_55.03.dat
85.7	43	126.685	900	78.46	1.54	8.286	B86.31_15.0_55.03.dat
87	44	126.518	950	79.642	1.54	8.287	B86.31_15.0_55.03.dat
88.4	45	126.211	1006	80.93	1.538	8.287	B86.31_15.0_55.03.dat

Table 5.15: Gyrotron constraints

Mode	TE <sub>22,7</sub>
Geometry Cavity Center ( $zG\_cavityCenter/mm$ )	396
Magnetic Field Cavity center ( $zB\_cavityCenter/mm$ )	416
Reference Position ( $zB\_refPos/mm$ )	416

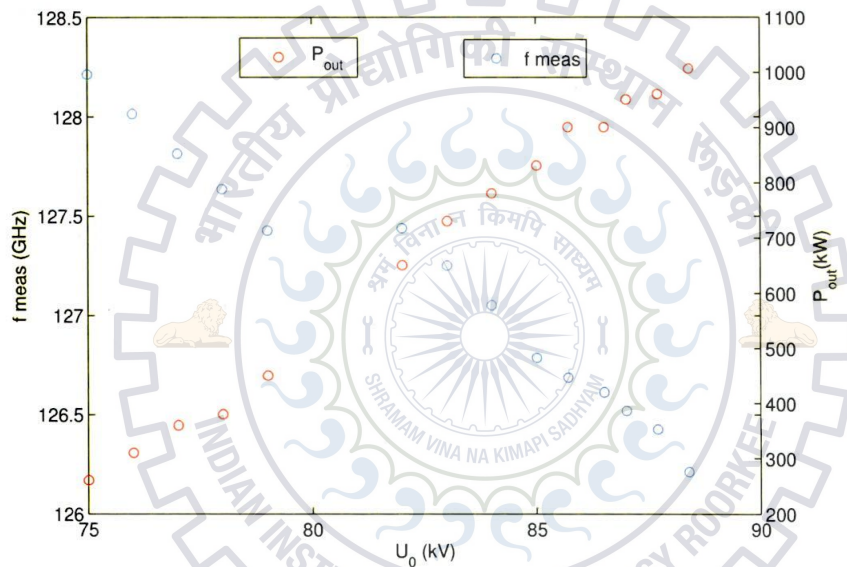


Figure 5.21: Data plot

### With Power Correction

First of all, we discuss the case with power correction considering power loss of 15%. Based on the available data, we have calculated the eigen values along the whole geometry, and also their root mean square error and variance between different data lines. Their curves can be seen in  $\chi$  RMS and Variance plot given in Figure 5.22. Plot shows several local minima points in RMS value of Chi as given in Table 5.16, also local minima points in variance curve of  $\chi$  given in Table 5.17. Taking only variance minimas into our consideration, Brillouin diagram for variance minimum 1) in Figure 5.23, minimum 2) in Figure 5.24, minimum 3) in Figure 5.25, minimum

4) in Figure 5.26 and minimum 5) in Figure 5.27 are shown.

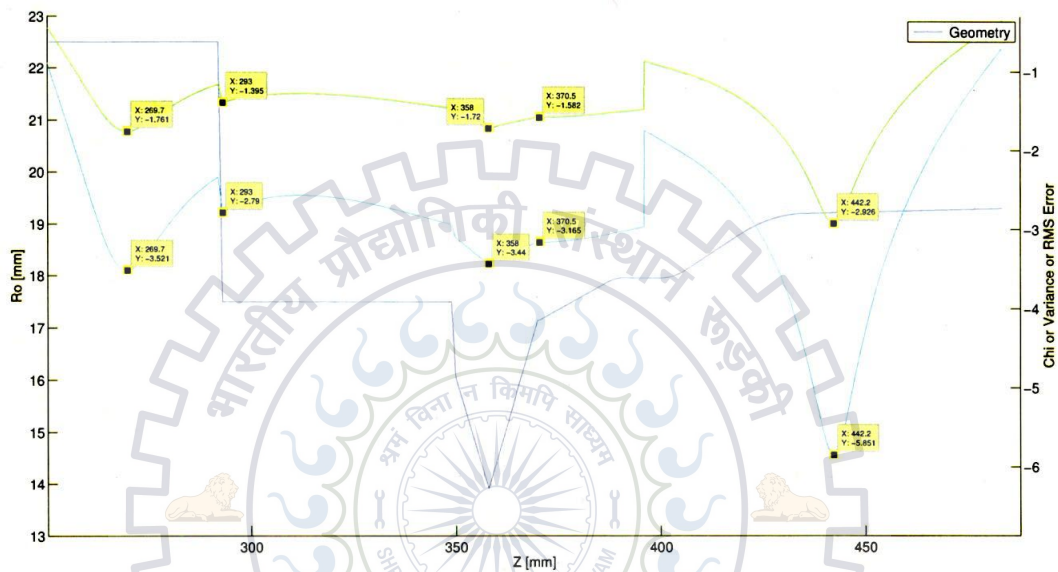


Figure 5.22:  $\chi$  RMS and Variance plot.

Table 5.16: Local minima points in RMS value of  $\chi$

	$\chi$	Z	$\log(\text{RMS}+(1e-6))$
1	47.1682	269.7000	-1.761
2	42.8677	293	-1.395
3	37.0647	358	-1.72
4	45.6874	370.5000	-1.582
5	50.6679	442.2000	-2.926

Table 5.17: Local minima points in variance curve of  $\chi$

	$\chi$	Z	$\log(\text{var}+(1e-6))$
1	47.1682	269.7000	-3.521
2	42.8677	293	-2.79
3	37.0647	358	-3.44
4	45.6874	370.5000	-3.165
5	50.6679	442.2000	-5.851

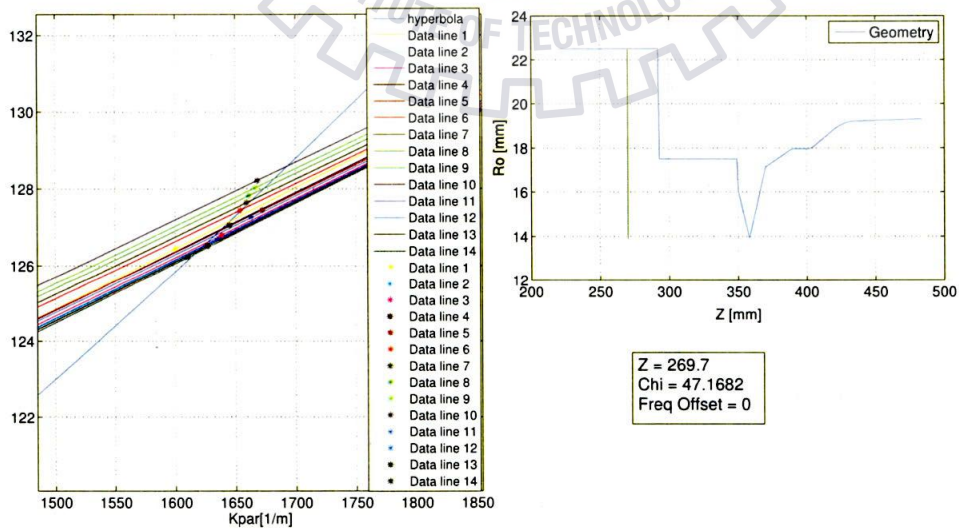


Figure 5.23: Brillouin Diagram for variance minimum 1).

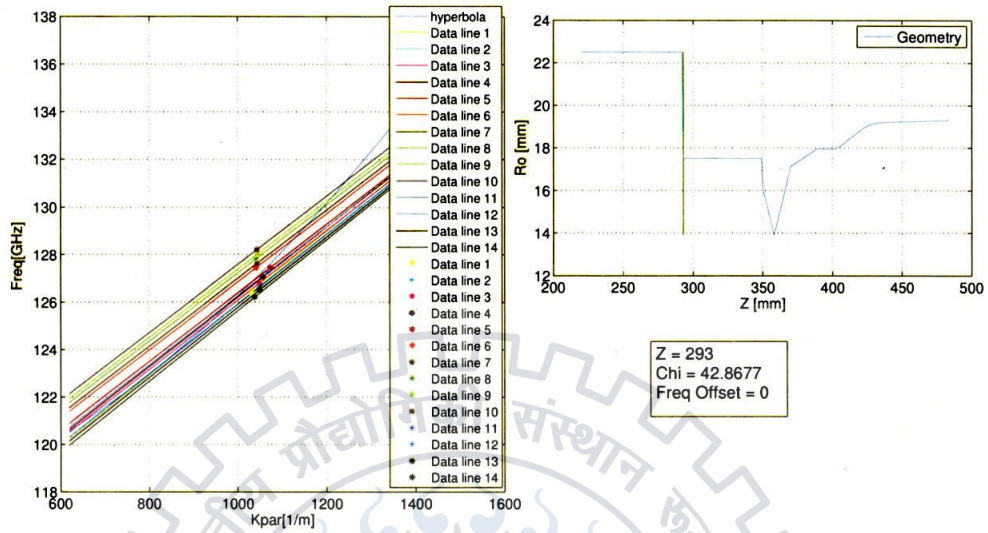


Figure 5.24: Brillouin Diagram for variance minimum 2).

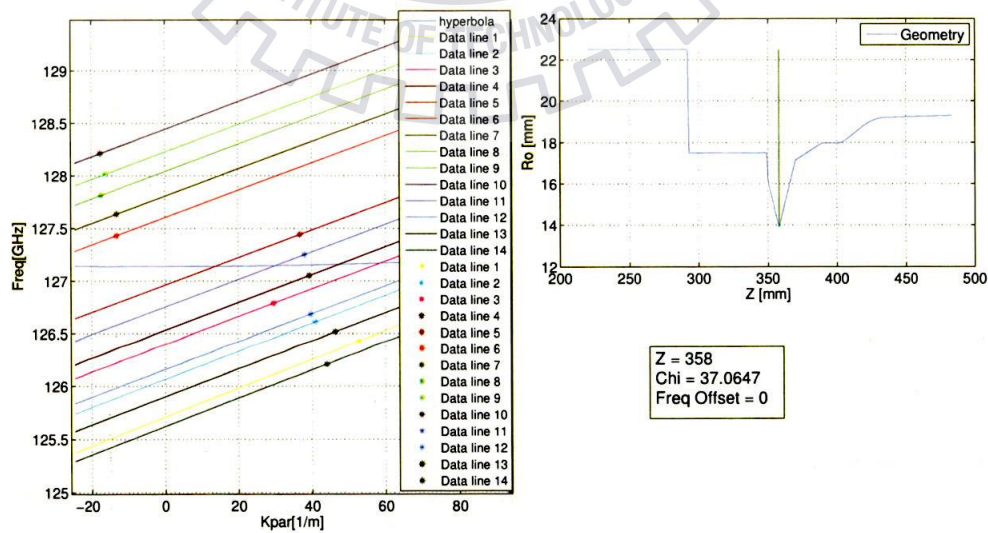


Figure 5.25: Brillouin Diagram for variance minimum 3).

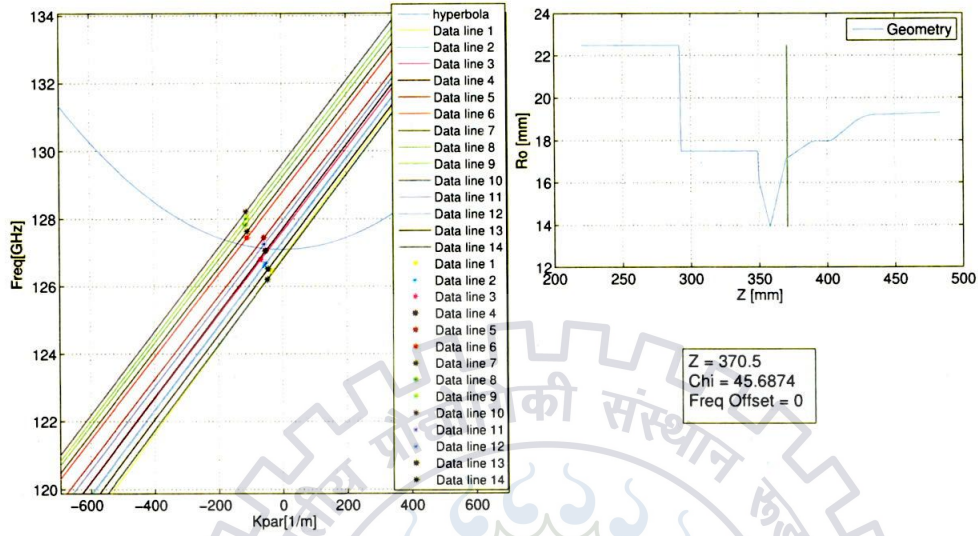


Figure 5.26: Brillouin Diagram for variance minimum 4).

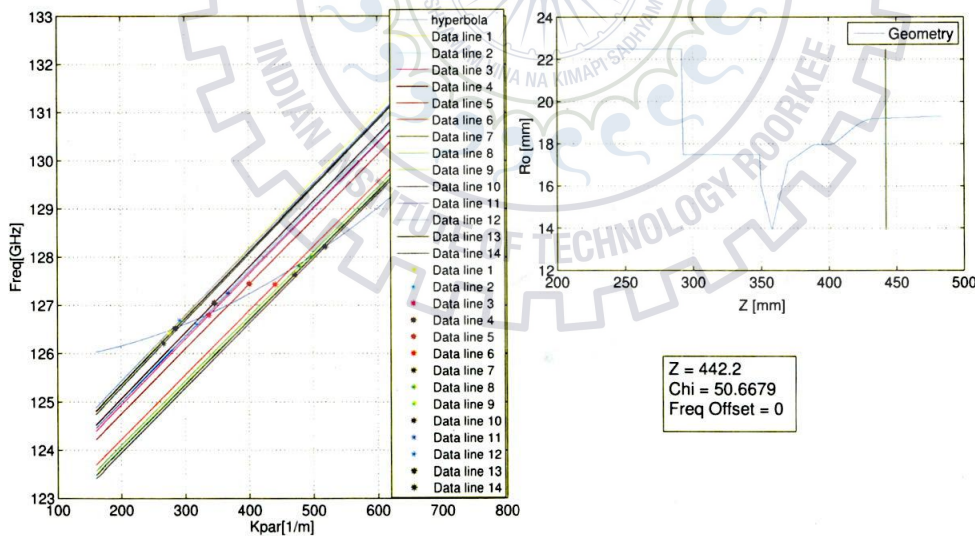


Figure 5.27: Brillouin Diagram for variance minimum 5).

We are getting best fit at  $Z=269.7$ . So on optimizing and taking the data lines 2,3,4,6,7,8,9,10,12,13 and 14 for the variance minimum 1)  $\chi=47.1682$ ,  $Z=269.7$ , we get the following Figure 5.28. Depending on the selection of the data lines, we get



the  $\chi$  RMS and Variance plot as shown in Figure 5.29.

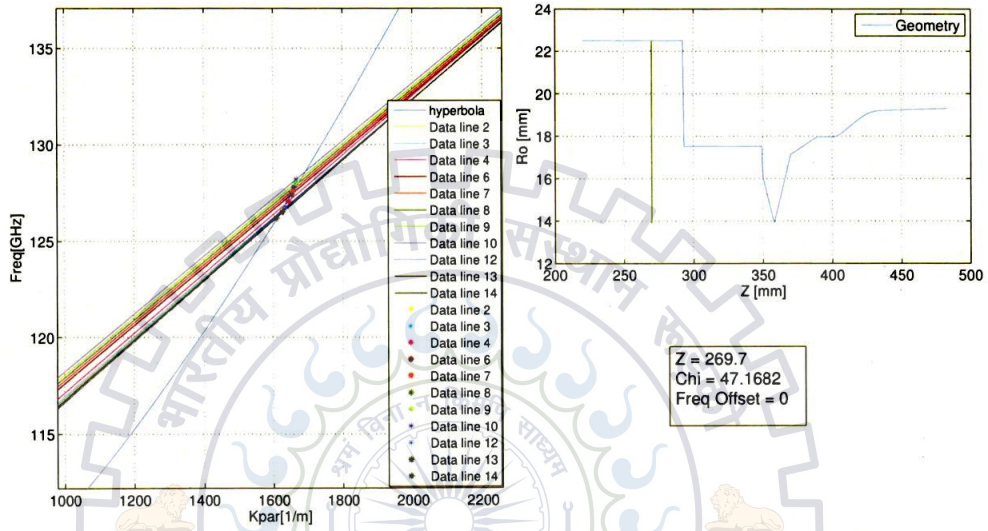


Figure 5.28: Brillouin Diagram after optimizing Variance minimum 1).

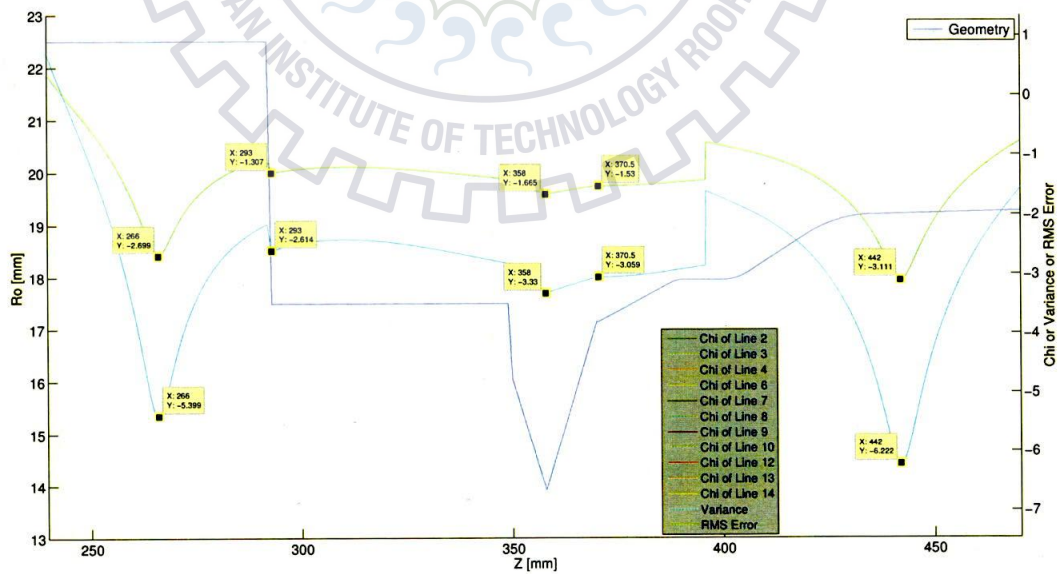


Figure 5.29:  $\chi$  RMS and Variance plot for selected data lines (2,3,4,6,7,8,9,10,12,13,14).

Plot shows several local minima points in RMS value of  $\chi$  as given in Table 5.18, also local minima points in variance curve of  $\chi$  given in Table 5.19.

Table 5.18: Local minima points in RMS value of  $\chi$

	$\chi$	Z	$\log(\text{RMS}+(1e-6))$
1	45.4046	266	-2.699
2	42.8677	293	-1.307
3	37.0647	358	-1.655
4	45.6874	370.5000	-1.53
5	50.6783	442	-3.111

Table 5.19: Local minima points in variance curve of  $\chi$

	$\chi$	Z	$\log(\text{var}+(1e-6))$
1	45.4046	266	-5.399
2	42.8677	293	-2.614
3	37.0647	358	-3.33
4	45.6874	370.5000	-3.059
5	50.6783	442	-6.222

We are getting best fit for variance minimum 1)  $Z=266$  and  $\chi=45.4046$ , as shown in the following Figure 5.30.

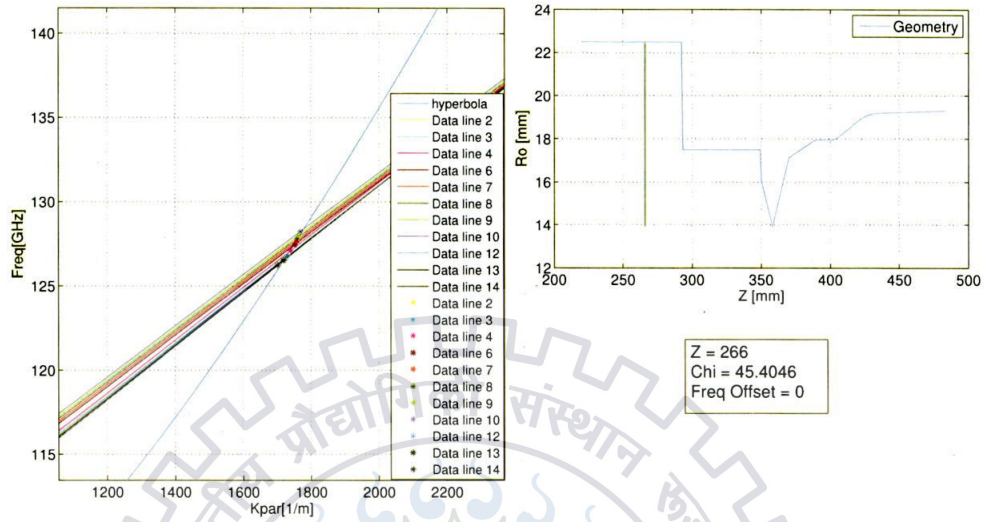


Figure 5.30: Brillouin Diagram for variance minimum 1).

At position  $Z=269.7$ , depending on the range of  $\chi$  value we are getting several approximate modes as given in Table 5.20. Coupling coefficient variation along  $Z$  axis with suitable modes are presented in the following figures, i.e., for mode  $TE_{15,9}$  in Figure 5.31 and for mode  $TE_{18,8}$  in Figure 5.32.

Table 5.20: Expected modes and their coupling coefficients at  $Z=269.7$  and  $\chi$  range between 46.859–47.5247.

m	n	$\chi$	G(max)	G(min)
44	1	46.8741	9.9370e-25	9.0515e-25
15	9	47.0595	0.0025	0.0025
8	12	47.2218	0.0017	0.0017
38	2	47.2461	1.4626e-17	1.3545e-17
30	4	47.4790	1.4385e-09	1.3641e-09
6	13	47.5220	1.8342e-04	1.6119e-04
18	8	47.5951	0.0033	0.0033

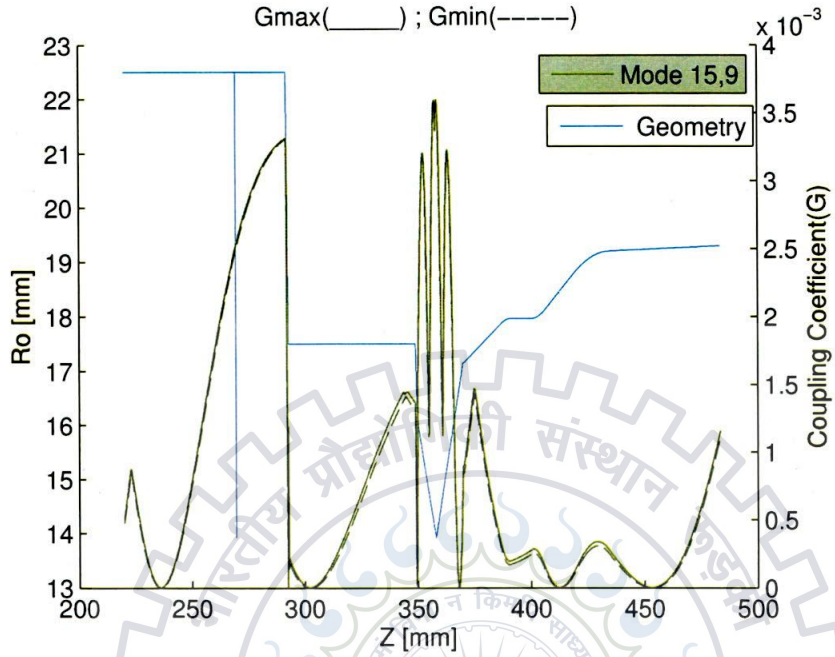


Figure 5.31: Coupling coefficient variation along Z axis for mode TE<sub>15,9</sub>

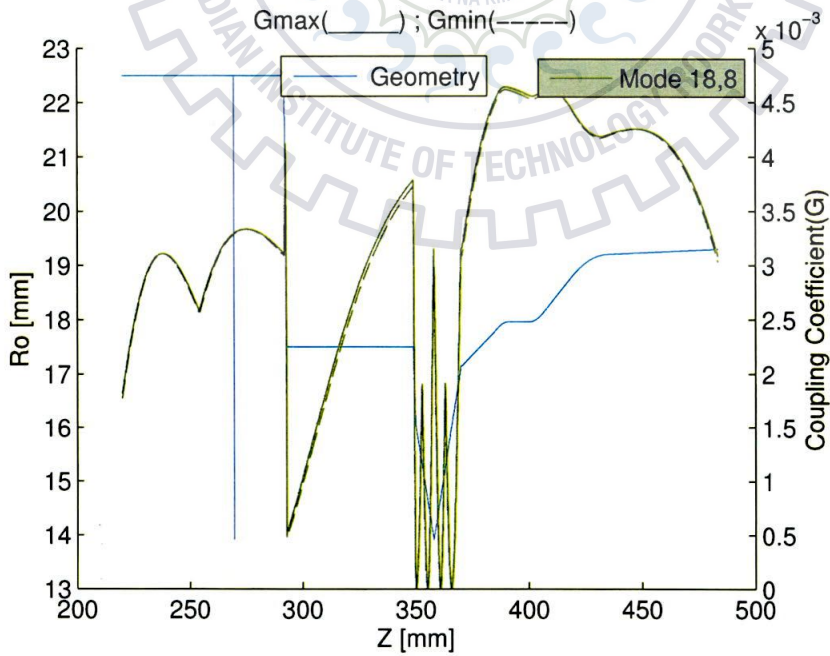


Figure 5.32: Coupling coefficient variation along Z axis for mode TE<sub>18,8</sub>

Similarly at position  $Z=266$ , depending on the range of  $\chi$  value we are getting several approximate modes as given in Table 5.21. Coupling coefficient variation along  $Z$  axis with suitable modes are presented in the following figures, i.e., for mode  $TE_{19,7}$  in Figure 5.33 and for mode  $TE_{16,8}$  in Figure 5.34.

Table 5.21: Expected modes and their coupling coefficients at  $Z=266$  and  $\chi$  range between 45–45.8934.

m	n	$\chi$	G(max)	G(min)
16	8	45.0254	0.0029	0.0029
36	2	45.1017	2.2875e-16	2.1282e-16
28	4	45.1847	1.2103e-08	1.1532e-08
9	11	45.4355	9.5850e-04	9.2206e-04
19	7	45.4357	0.0021	0.0021
32	3	45.5102	4.5721e-12	4.3042e-12
25	5	45.5592	2.8802e-06	2.7730e-06
22	6	45.6243	1.7289e-04	1.6841e-04
14	9	45.7402	0.0013	0.0013
7	12	45.7940	7.2182e-04	6.8617e-04
43	1	45.8524	6.6101e-24	6.0355e-24
5	13	46.0586	0.0014	0.0014

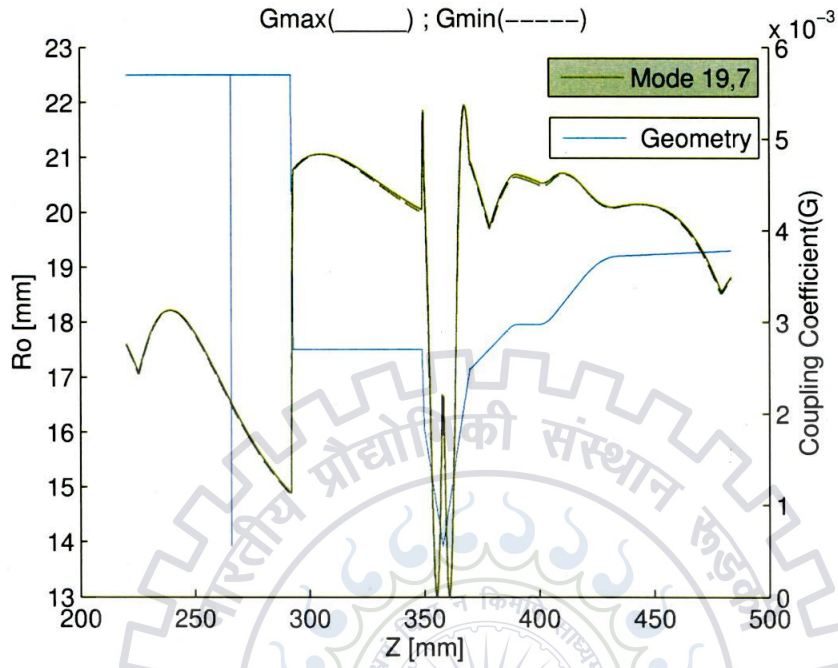


Figure 5.33: Coupling coefficient variation along Z axis for mode TE<sub>19,7</sub>

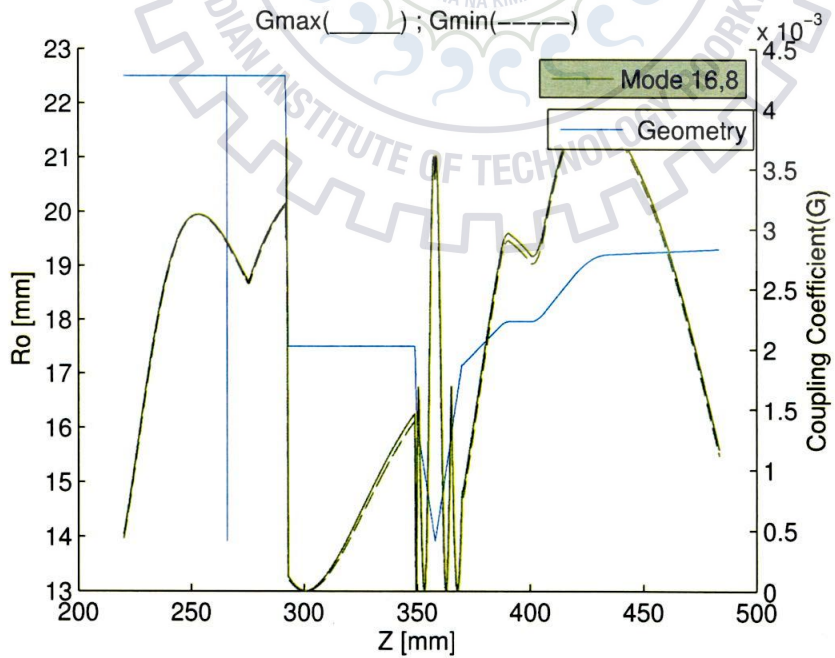


Figure 5.34: Coupling coefficient variation along Z axis for mode TE<sub>16,8</sub>

From the Figure 5.22, we can also see that best fit is also present at  $Z=442.2$ . So on optimizing and taking the data lines 1,2,3,6,7,8,9,10 and 13 for the variance minimum 5)  $\chi=50.6679$  and  $Z=442.2$  showed in Figure 5.27, we get the following Figure 5.35.

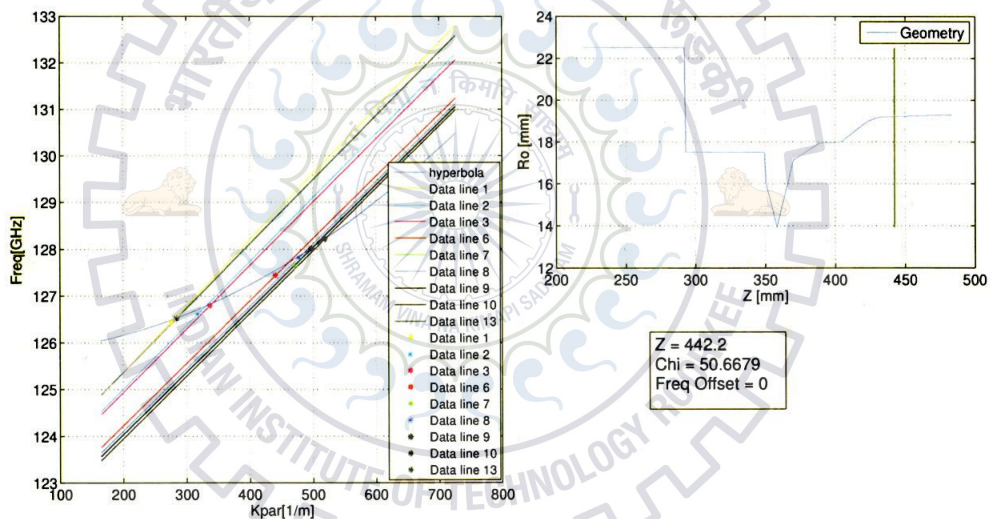


Figure 5.35: Brillouin Diagram after optimizing variance minimum 5).

Depending on the selection of the data lines, we get the  $\chi$  RMS and Variance plot as shown in Figure 5.29.

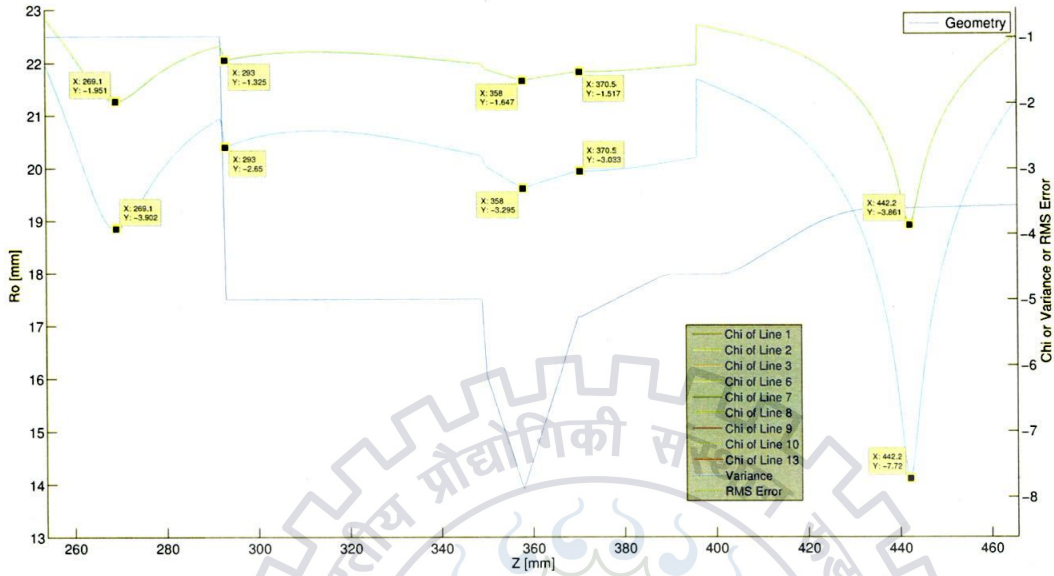


Figure 5.36:  $\chi$  RMS and Variance plot for selected data lines (1,2,3,6,7,8,9,10,13).

Plot shows several local minima points in RMS value of  $\chi$  as given in Table 5.22, also local minima points in variance curve of  $\chi$  given in Table 5.23. Depending on the range of  $\chi$  value we are getting several approximate modes, as given in Table 5.24. Coupling coefficient variation along Z axis with suitable modes are presented in the following figures, i.e., for mode  $TE_{6,14}$  in Figure 5.37, for mode  $TE_{20,8}$  in Figure 5.38, for mode  $TE_{23,7}$  in Figure 5.39 and for mode  $TE_{13,11}$  in Figure 5.40.

Table 5.22: Local minima points in RMS value of  $\chi$

	$\chi$	Z	$\log(\text{RMS}+(1e-6))$
1	46.8939	269.1000	-1.951
2	42.8677	293	-1.325
3	37.0647	358	-1.647
4	45.6874	370.5000	-1.517
5	50.6679	442.2000	-3.861



Table 5.23: Local minima points in variance curve of  $\chi$ 

	$\chi$	Z	$\log(\text{var}+(1e-6))$
1	46.8939	269.1000	-3.902
2	42.8677	293	-2.65
3	37.0647	358	-3.295
4	45.6874	370.5000	-3.033
5	50.6679	442.2000	-7.72

Table 5.24: Expected modes and their coupling coefficients at  $Z=442.2$  and  $\chi$  range between 50–51

m	n	$\chi$	G(max)	G(min)
10	12	50.0404	0.0017	0.0016
20	8	50.1386	0.0037	0.0036
29	5	50.2676	3.1694e-06	3.0363e-06
15	10	50.3625	0.0010	9.8126e-04
8	13	50.4070	7.1039e-04	6.6136e-04
23	7	50.4088	0.0023	0.0023
41	2	50.4541	2.0826e-16	1.9212e-16
26	6	50.4634	1.7765e-04	1.7229e-04
6	14	50.6878	9.4403e-04	8.9247e-04
4	15	50.8862	1.8495e-05	9.6520e-06
33	4	50.9004	7.1325e-09	6.7441e-09
13	11	50.9458	0.0023	0.0023
48	1	50.9576	1.1286e-23	1.0212e-23
18	9	50.9711	0.0029	0.0029
2	16	51.0043	9.5374e-05	7.3699e-05

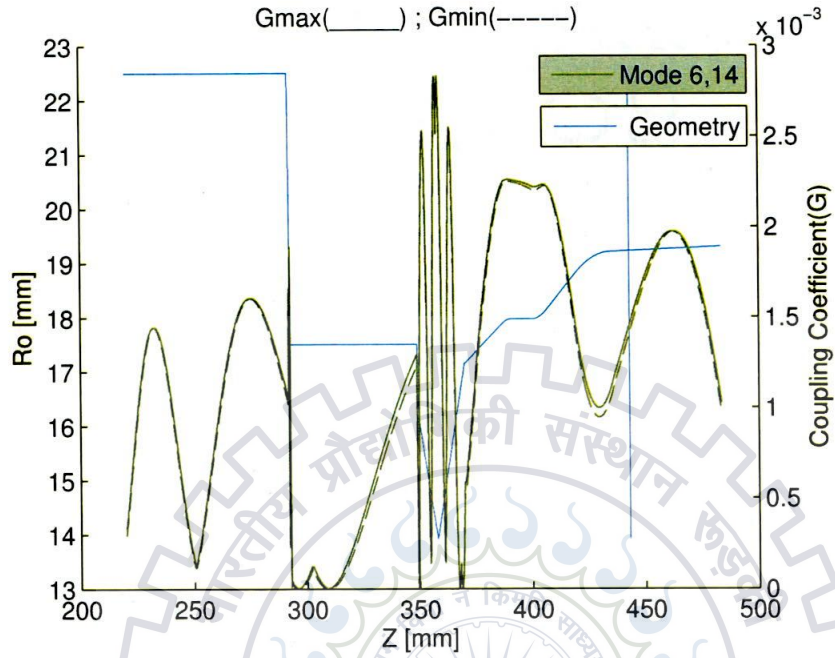


Figure 5.37: Coupling coefficient variation along Z axis for mode TE<sub>6,14</sub>

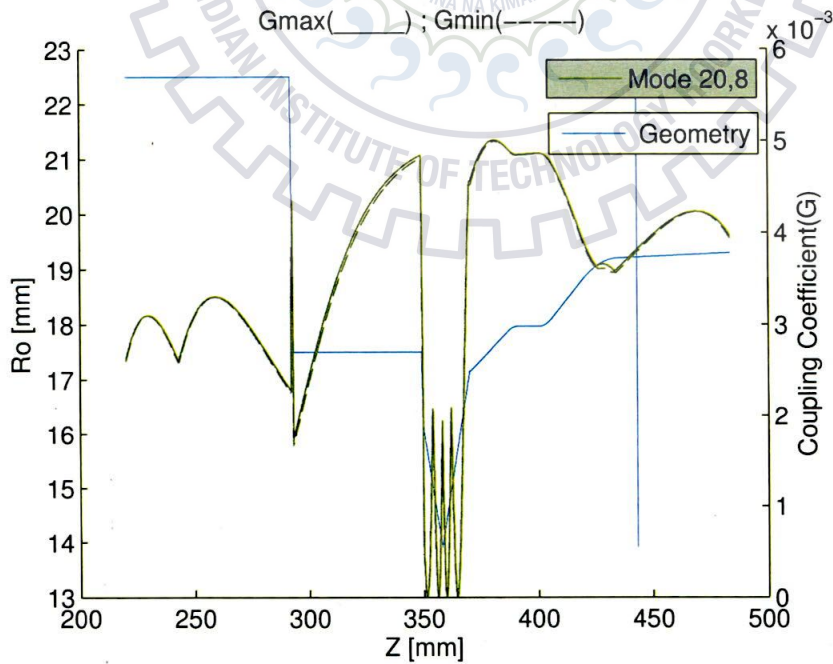


Figure 5.38: Coupling coefficient variation along Z axis for mode TE<sub>20,8</sub>

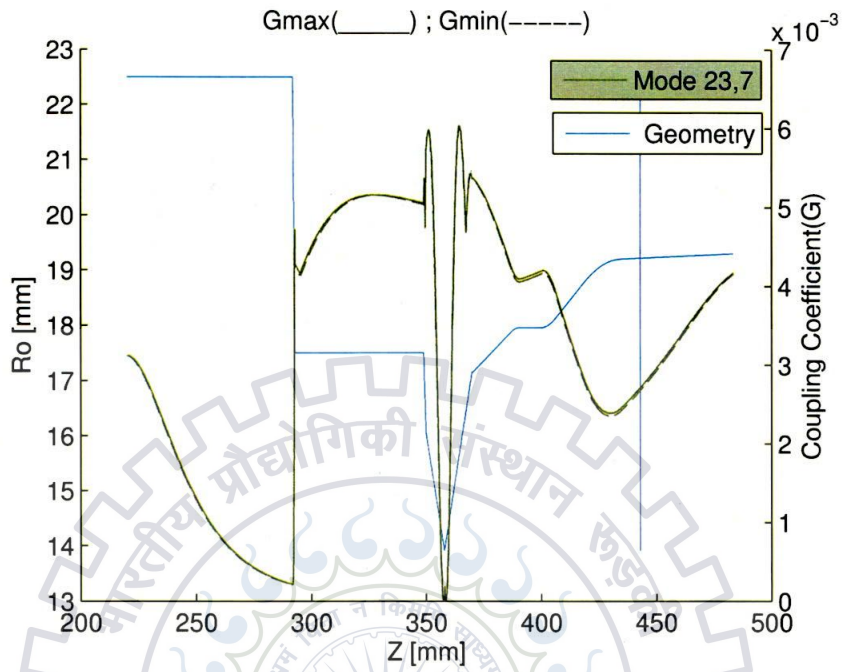


Figure 5.39: Coupling coefficient variation along Z axis for mode TE<sub>23,7</sub>

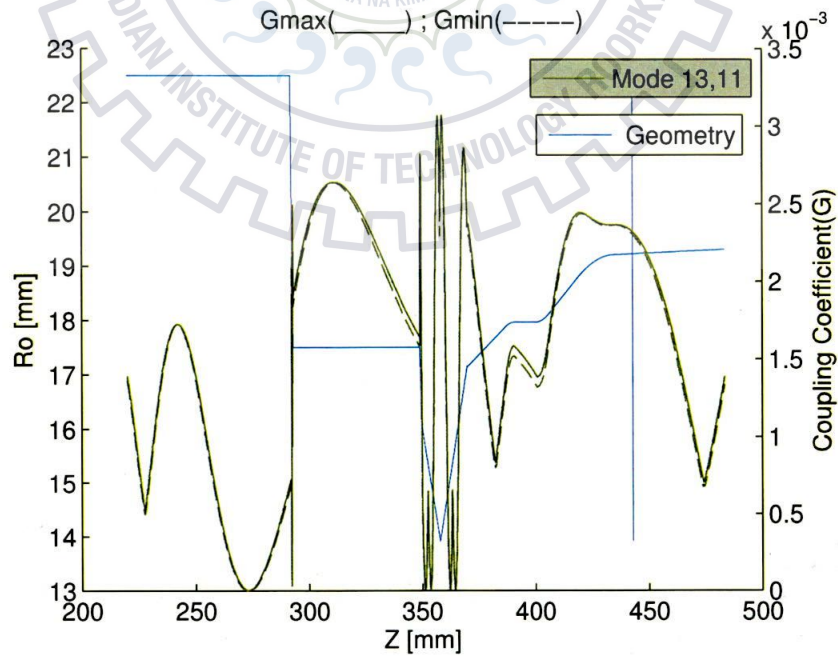


Figure 5.40: Coupling coefficient variation along Z axis for mode TE<sub>13,11</sub>

**Without Power Correction**

Now we discuss the results coming from the tool with the same data but without considering power correction.  $\chi$  RMS and Variance plot is shown in Figure 5.41.

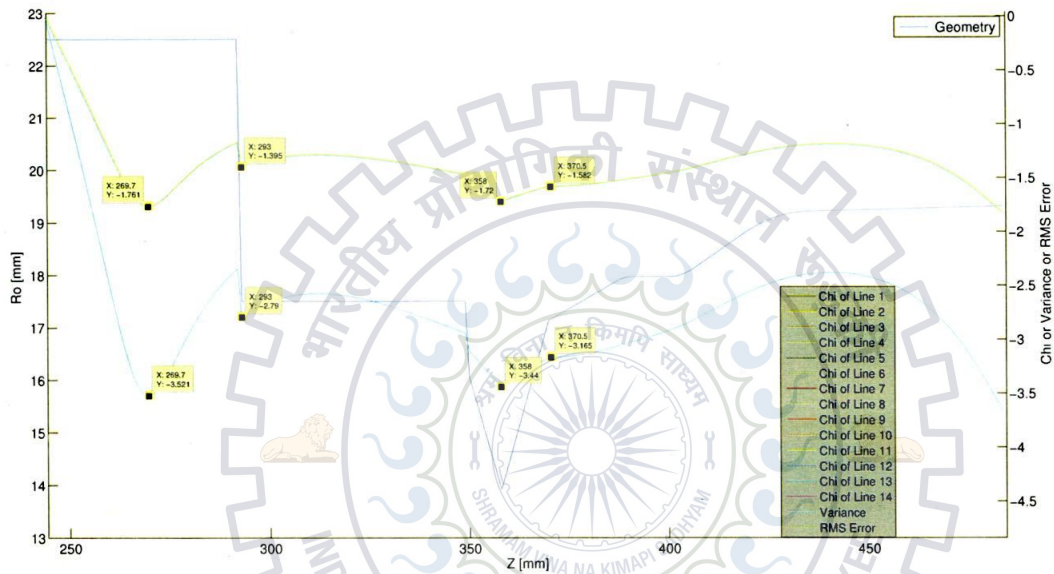


Figure 5.41:  $\chi$  RMS and Variance plot without power correction.

Plot shows several local minima points in RMS value of  $\chi$  as given in Table 5.25, also local minima points in variance curve of  $\chi$  given in Table 5.26.

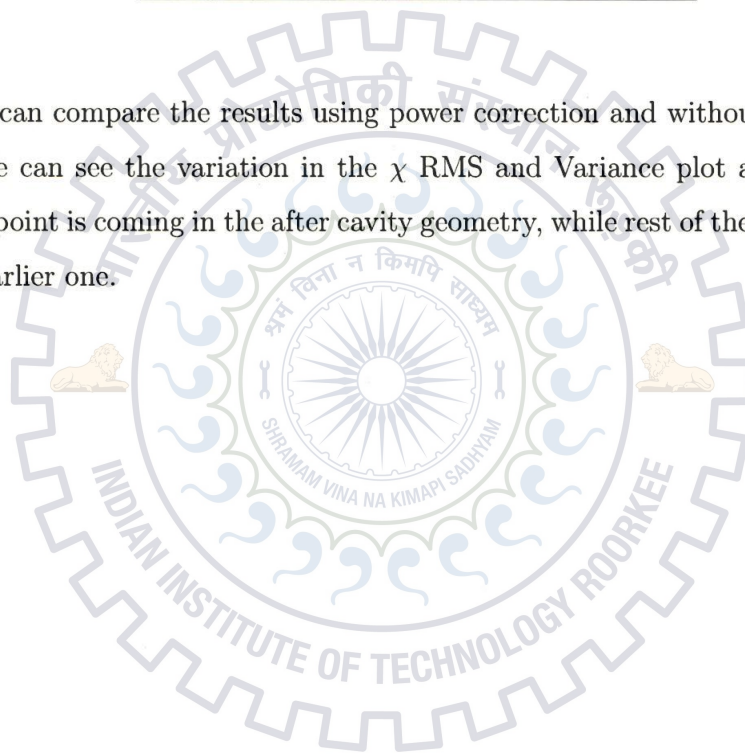
Table 5.25: Local minima points in RMS value of  $\chi$

	$\chi$	Z	$\log(\text{RMS}+(1\text{e-}6))$
1	47.1682	269.7000	-1.761
2	42.8677	293	-1.395
3	37.0647	358	-1.72
4	45.6874	370.5000	-1.582

Table 5.26: Local minima points in variance curve of  $\chi$ 

	$\chi$	Z	$\log(\text{var}+(1e-6))$
1	47.1682	269.7000	-3.521
2	42.8677	293	-2.79
3	37.0647	358	-3.44
4	45.6874	370.5000	-3.165

Now we can compare the results using power correction and without power correction. We can see the variation in the  $\chi$  RMS and Variance plot after cavity. No minima point is coming in the after cavity geometry, while rest of the curve is similar to the earlier one.



## 5.3 Results and Discussion on checking Coupled Dispersion Relation

### 5.3.1 Case 1

Now we discuss the results coming from the tool when we are testing coupled dispersion relation with W7-X data. Here we consider the variation along cathode voltage. Data file for the same is given in the Table 5.28 and its constraints are given in the Table 5.27.

We do something special here, in applying our techniques to a cavity mode. An important point is that the frequencies of both the coupled and the uncoupled dispersion relation fail to reproduce the behavior of the gyrotron. This shows that “strong” interactions are much more dynamic, and cannot be covered by linear theory. This is acceptable because parasites are by far not as strong or efficient as cavity modes, so this discrepancy is expected to be smaller. Of course it is quite impossible to investigate the assumption (referred in section 3.6).

Table 5.27: Gyrotron Constraints

Mode	28,8
Mag Field	5.604
Cavity Radius/mm	20.48
Beam Radius/mm	10.15

Table 5.28: Data of W7-X for TE<sub>28,8</sub>

Data Line	Measurement data			Simulation data		
	$U_0$ kV	$I_b$ A	f meas GHz	$E_{kin}$ kV	$\beta_{\parallel}$	$\beta_{\perp}$
1	71.7	38.4	140.328	67.1	0.323	0.3377
2	73.7	39.1	140.31	69.0	0.320	0.3483
3	75.7	39.1	140.297	70.9	0.316	0.359
4	77.7	40.0	140.297	72.8	0.311	0.37
5	80	40.0	140.3	74.9	0.305	0.3826
6	80.5	40.4	140.3	75.4	0.303	0.3854
7	81.7	41.1	140.297	76.5	0.300	0.392
8	82.3	41.1	140.297	77.1	0.298	0.3954
9	83	41.1	140.289	77.7	0.295	0.3992
10	84.3	41.1	140.281	78.9	0.290	0.4064
11	85.7	41.7	140.274	80.1	0.285	0.4142
12	86.3	41.7	140.258	80.7	0.282	0.4175
13	87.7	41.7	140.242	81.9	0.277	0.4251

The variation in measured frequency along variation in cathode voltage is presented in Figure 5.42. For data line 1, perturbed dispersion curves of the mode TE<sub>22,8</sub> and linear instability growth rate in a vacuum waveguide are shown in Figure 5.42. From the curves we can see the distortion in the hyperbola.

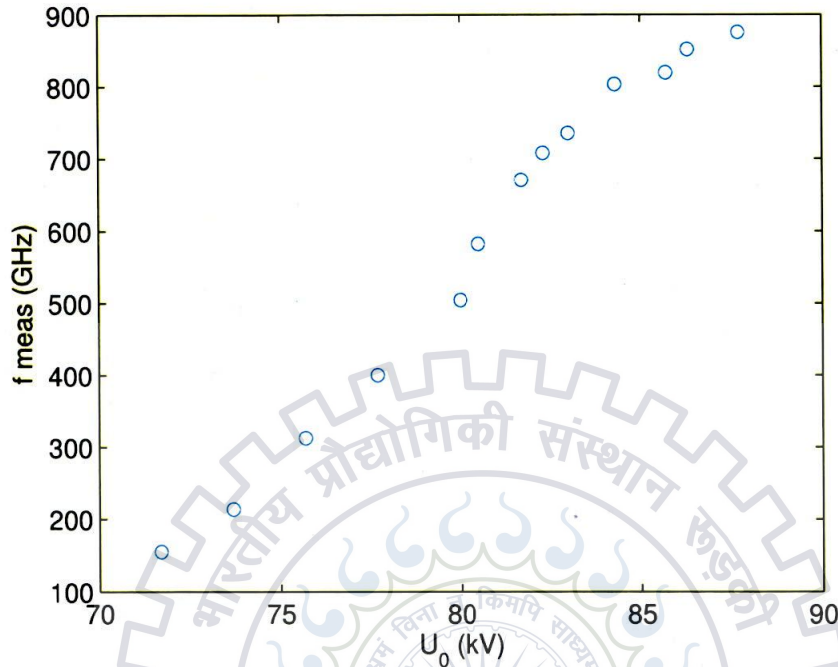
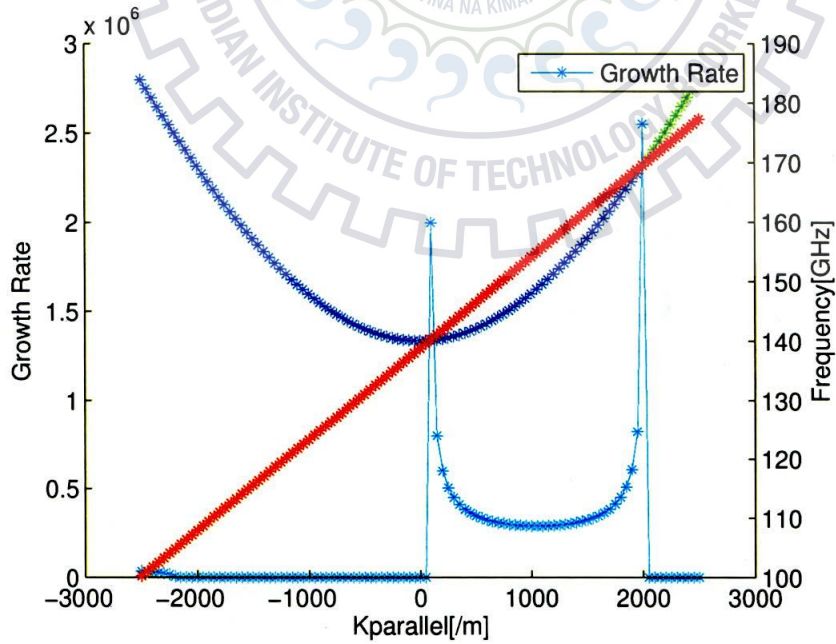


Figure 5.42: Data plot



(a) Whole region



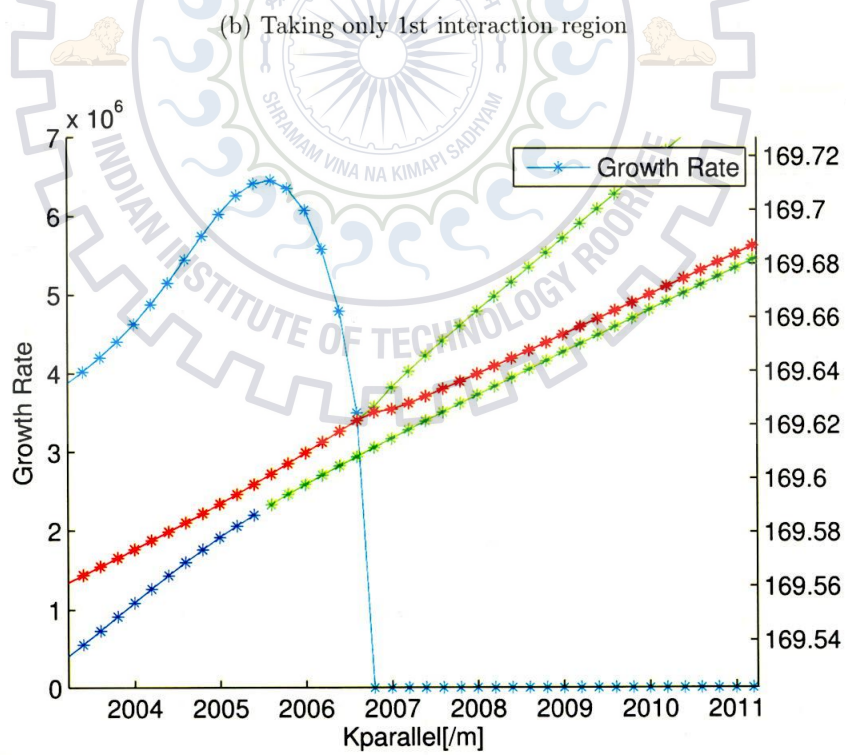
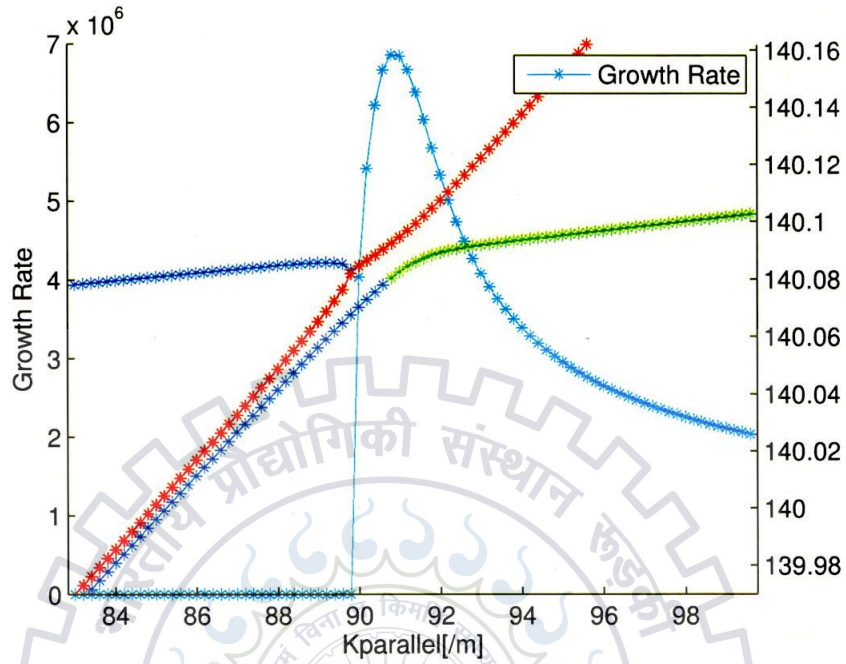


Figure 5.42: Perturbed dispersion curves of the mode  $TE_{22,8}$  and linear instability growth rate in a vacuum waveguide.

As explained earlier also, the perturbation is strongest near the points of intersection between the dispersion curves of the waveguide and beam modes. In the vicinities of these points, the modes are unstable. Point of highest growth rate gives us the point of interaction, depending on this, whole analysis of coupled dispersion relation for cavity mode  $TE_{28,8}$  is shown in Table 5.29.

Table 5.29: Analysis of Coupled Dispersion Relation for  $TE_{28,8}$

DataLine	Uncoupled Freq GHz	Coupled Max Freq GHz	Coupled Min Freq GHz	Growth Rate $\text{Imag}(\omega/2\pi)$
1	140.0897	140.092	140.08	6.87E+06
2	140.1536	140.157	140.145	7.07E+06
3	140.2413	140.245	140.233	7.21E+06
4	140.3619	140.366	140.353	7.43E+06
5	140.5621	140.565	140.552	7.61E+06
6	140.6077	140.61	140.597	7.68E+06
7	140.7681	140.773	140.76	7.82E+06
8	140.8577	140.861	140.848	7.87E+06
9	140.9541	140.959	140.945	7.94E+06
10	141.2016	141.205	141.191	8.06E+06
11	141.5907	141.594	141.58	8.22E+06
12	141.7774	141.781	141.767	8.28E+06
13	142.4854	142.491	142.477	8.39E+06

### 5.3.2 Case 2

On applying coupled dispersion relation on the results of 140 GHz gyrotron, having measurement data considering variation along magnetic field (as done in earlier section), following results are obtained. As we are getting best fit at  $Z=348.8$  and  $Z=447.2$ , so both these are points are analysed with suitable modes. Here, analysis results are only presented for data lines 1, 5, 8, and 11.

General data in Table 5.30 and analysis results of Coupled Dispersion Relation for  $TE_{19,6}$  are shown in Table 5.31.

Table 5.30: Testing of Mode  $TE_{19,6}$

Z	348.8
Mode	19,6
Coup Coeff	0.0057
	41.9446

Table 5.31: Analysis of Coupled Dispersion Relation for  $TE_{19,6}$

Data Line	Uncoupled Freq GHz	Coupled Max Freq GHz	Coupled Min Freq GHz	Growth Rate $\text{Imag}(\omega/2\pi)$	Freq in Table GHz
1	129.1293	129.132	129.123	4.93E+06	129.435
5	129.2572	129.06	129.052	4.92E+06	129.361
8	128.9989	129.002	128.993	4.92E+06	129.314
11	128.9424	128.945	128.936	4.90E+06	129.247

CHAPTER 5. ANALYSIS RESULTS

General data in Table 5.32 and analysis results of coupled dispersion relation for  $TE_{22,5}$  are shown in Table 5.33.

Table 5.32: Testing of Mode  $TE_{22,5}$

Z	348.8
Mode	22,5
Coup Coeff	0.0047
$\chi$	41.9879

Table 5.33: Analysis of Coupled Dispersion Relation for  $TE_{22,5}$

Data Line	Uncoupled Freq GHz	Coupled Max Freq GHz	Coupled Min Freq GHz	Growth Rate $\text{Imag}(\omega/2\pi)$	Freq in Table GHz
1	129.2231	129.227	129.216	6.17E+06	129.435
5	129.1532	129.157	129.146	6.16E+06	129.361
8	129.0957	129.099	129.088	6.20E+06	129.314
11	129.0412	129.044	129.033	6.18E+06	129.247

General data in Table 5.34 and analysis results of coupled dispersion relation for  $TE_{21,8}$  are shown in Table 5.35.

Table 5.34: Testing of Mode  $TE_{21,8}$

Z	447.2
Mode	21,8
Coup Coeff	0.0044
$\chi$	51.4014

Table 5.35: Analysis of Coupled Dispersion Relation for  $TE_{21,8}$ 

Data Line	Uncoupled Freq GHz	Coupled Max Freq GHz	Coupled Min Freq GHz	Growth Rate $\text{Imag}(\omega/2\pi)$	Freq in Table GHz
1	128.5802	128.584	128.572	7.09E+06	129.435
5	128.5006	128.505	128.492	7.10E+06	129.361
8	128.4361	128.439	128.427	7.09E+06	129.314
11	128.3745	128.378	128.365	7.10E+06	129.247

General data in Table 5.36 and analysis results of coupled dispersion relation for  $TE_{19,9}$  are shown in Table 5.37.

Table 5.36: Testing of Mode  $TE_{19,9}$ 

Z	447.2
Mode	19,9
Coup Coeff	0.0045
$\chi$	52.2612

Table 5.37: Analysis of Coupled Dispersion Relation for  $TE_{19,9}$ 

Data Line	Uncoupled Freq GHz	Coupled Max Freq GHz	Coupled Min Freq GHz	Growth Rate $\text{Imag}(\omega/2\pi)$	Freq in Table GHz
1	130.1248	130.127	130.119	4.58E+06	129.435
5	130.067	130.069	130.061	4.54E+06	129.361
8	130.0221	130.024	130.016	4.55E+06	129.314
11	129.9801	129.983	129.975	4.55E+05	129.247

General data in Table 5.38 and analysis results of coupled dispersion relation for  $TE_{7,14}$  are shown in Table 5.39.

Table 5.38: Testing of Mode  $TE_{7,14}$

Z	447.2
Mode	7,14
Coup Coeff	0.0020
$\chi$	52.1438

Table 5.39: Analysis of Coupled Dispersion Relation for  $TE_{7,14}$

Data Line	Uncoupled Freq GHz	Coupled Max Freq GHz	Coupled Min Freq GHz	Growth Rate Imag( $\omega/2\pi$ )	Freq in Table GHz
1	129.9016	129.905	129.895	5.48E+06	129.435
5	129.8416	129.844	129.834	5.46E+06	129.361
8	129.793	129.796	129.786	5.48E+06	129.314
11	129.7473	129.75	129.741	5.48E+06	129.247

The analysis results in the above tables provide us the corridor for interaction frequency considering both coupled and uncoupled dispersion relation. On matching these frequencies with the measured frequencies, we can decide the existence of the particular mode which has been considered for analysis.

## Chapter 6

# Conclusions And Future Scope

### 6.1 Conclusions

- From the analysis results coming from the tool, we came to know about probable position of generation of parasitic oscillations. Frequencies of parasitic oscillations are measured experimentally and analysed to locate where they come from. It simply tells us that these positions are probably the location of the frequencies measured.
  - We found multiple minima along the Z axis. In case 1 and 2, no power correction is used due to unavailability of measured power, found minimas are of equal quality and appear at similar magnetic field strengths before and after the cavity because there are always two places where  $\omega_c \sim \omega_{RF}$ .
  - In case 3, when we consider with power correction, after cavity effect is much stronger. This case shows that power correction is necessary to distinguish between the minimas properly. While when we do analysis without power correction, the after cavity results are much different, and we do not get the strong minima for  $Z > Z_{cavity}$ .

- Coupling coefficient investigation is a valuable addition to the resonance-based investigation, and it helps to associate probable modes with the eigenvalues found by the Brillouin Tool. The expected mode which can be oscillated depends on their coupling coefficient value. We are using several data lines having a corridor of  $\chi$  and also we are using frequency offset, due to these reasons we extend our  $\chi$  range for calculating probable modes present. Variation of coupling along whole geometry gives us the idea of the behavior of the particular mode.
- Coupled dispersion relation is used to investigate the point of interaction. The results are very much similar to what explained in [23] [24]. Hyperbola is distorted near the points of interaction and gives a corridor for approximation of perfect frequency of operation. It is also measured experimentally that operating frequency is slightly different from the cold interaction frequency.

## 6.2 Future Scope

Some of the future works of the current research work are as follows:

- Depending on the modes and position of parasitic oscillations which are generating in the gyrotrons, several measures have to be done to remove these oscillations in order to increase the efficiency of the main mode.
- Our results for coupled dispersion relation are not as much accurate, more work can be done in this area. There are several other approaches also which define this relation, and can be implemented to get some better results (as in [24]). We can also take into account a magnetized plasma waveguide penetrated by a beam of electron oscillators, having some electron plasma density to see its

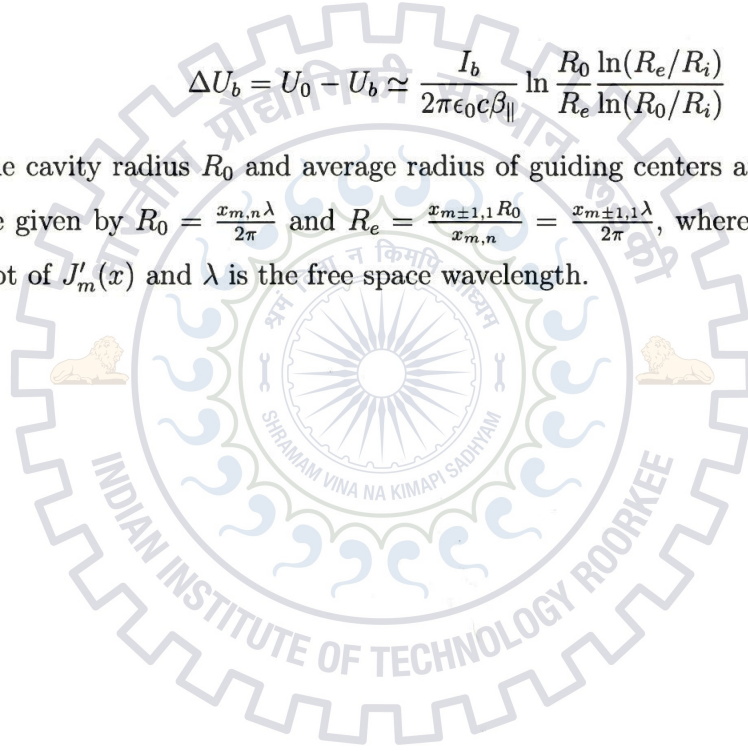


effect on dispersion diagrams.

- The tool was developed for the use with conventional gyrotrons, and different formulation must be adapted if it is used on coaxial geometries. As in the case of a coaxial cavity having insert radius  $R_i$ , voltage depression is defined by [22]

$$\Delta U_b = U_0 - U_b \simeq \frac{I_b}{2\pi\epsilon_0 c\beta_{\parallel}} \ln \frac{R_0 \ln(R_e/R_i)}{R_e \ln(R_0/R_i)} \quad (6.1)$$

The cavity radius  $R_0$  and average radius of guiding centers at interaction  $R_e$  are given by  $R_0 = \frac{x_{m,n}\lambda}{2\pi}$  and  $R_e = \frac{x_{m\pm 1,1}R_0}{x_{m,n}} = \frac{x_{m\pm 1,1}\lambda}{2\pi}$ , where  $x_{mn}$  is the  $n$ th root of  $J'_m(x)$  and  $\lambda$  is the free space wavelength.



# Bibliography

- [1] M. Thumm, "State-of-the-art of High Power Gyro- Devices and Free Electron Maseres, Update 2011," KIT Scientific Reports 7606, Karlsruhe Institute of Technology, Germany, 2012.
- [2] M. V. Kartikeyan, E. Borie, and M. Thumm, *Gyrotrons - High power microwave and millimeter wave technology*, Berlin-Heidelberg, Germany: Springer-Verlag, 2004.
- [3] J. Jelonnek, K. Avramidis, J. Franck, G. Dammertz, G. Gantenbein, K. Hesch, S. Illy, J. Jin, A. Malygin, I.Gr. Pagonakis, B. Pioeczyk, T. Rzesnicki, A. Samartsev, A. Schlaich, M. Thumm, J. Zhang, "KIT Contribution to the Gyrotron Development for Nuclear Fusion Experiments in Europe," *Microwave Conference (GeMIC), 2014 German*, pp.1-4, 10-12 March 2014.
- [4] M. Thumm, "High-power Gyro-devices for plasma heating and other applications," *International Journal of Infrared and Millimeter Waves*, vol. 26, no. 4, pp. 483-503, April 2005.
- [5] M. Thumm, "Progress on Gyrotrons for ITER and Future Thermonuclear Fusion Reactors," *Plasma Science, IEEE Transactions on* , vol.39, no.4, pp.971-979, April 2011.
- [6] Kwo Ray Chu, "Overview of research on the gyrotron traveling-wave amplifier," *IEEE Trans. Plasma Sci.* , vol.30, no.3, pp. 903-908, Jun 2002.

- [7] Q.F.Li, S.Y. Park, J.L. Hirshfield, "Theory of Gyrotron Traveling-Wave Amplifiers," *IEEE Trans. Microwave Theory and Techniques*, vol.34, no.10, pp. 1044-1058, Oct 1986.
- [8] M. Thumm, "Progress in gyrotron development," *Fusion Engineering and Design*, vol. 66-68, pp. 69-90, Sept. 2003.
- [9] K. L. Felch, B. G. Danly, H. R. Jory, K. E. Kreischer, W. Lawson, B. Levush, R.J. Temkin, "Characteristics and applications of fast-wave gyrodevices," *Proceedings Of The IEEE*, vol. 87, no. 5, pp. 752-781, May 1999.
- [10] A.Kupiszewski, "The Gyrotron: A High Frequency Microwave Amplifier," *DSN Progress Report 42-52*, May and June 1979.
- [11] Timothy C. Luce, "Applications of High-Power Millimeter Waves in Fusion Energy Research", *IEEE Transactions on Plasma Science*, vol. 30, no. 3, June 2002.
- [12] J. P. Calame, M. Garven, B. G. Danly, B. Levush, and K. T. Nguyen, "Gyrotron-traveling-wave-tube circuits based on lossy ceramics," *IEEE Trans. Electron Devices*, vol. 49, pp. 1469-1477, Aug. 2002.
- [13] M. Garven, J.P. Calame, B.G. Danly, K.T. Nguyen, B. Levush, F.N. Wood, D.E. Pershing, "A gyrotron traveling wave tube amplifier experiment with a ceramic loaded interaction region," *IEEE Trans., Plasma Sci.*, vol.30, no.3, pp. 885-893, Jun 2002.
- [14] S. Kern, A. Schlaich, J. Flamm, G. Gantenbein, G. Latsas, T. Rzesnicki, A. Samartsev, M. Thumm, I. Tigelis, "Investigations on parasitic oscillations in megawatt gyrotrons," *Infrared, Millimeter, and Terahertz Waves, 2009. IRMMW-THz 2009. 34th International Conference on*, pp.1-3, 21-25 Sept. 2009.

- [15] G. Gantenbein, G. Dammertz, J. Flamm, S. Illy, S. Kern, G. Latsas, B. Piosczyk, T. Rzesnicki, A. Samartsev, A. Schlaich, M. Thumm, "Experimental Investigations and Analysis of Parasitic RF Oscillations in High-Power Gyrotrons," *IEEE Transactions on Plasma Science*, vol. 38, no. 6, June 2010.
- [16] A. Schlaich, A.R. Choudhury, G. Gantenbein, S. Illy, S. Kern, C. Lievin, A. Samartsev, M. Thumm, "Examination of parasitic after-cavity oscillations in the W7-X series gyrotron SN4R," *Infrared, Millimeter and Terahertz Waves (IRMMW-THz), 2011 36th International Conference on*, pp.1,2, 2-7 Oct. 2011.
- [17] M. K. Hornstein, *Design of a 460 GHz Second Harmonic Gyrotron Oscillator for use in Dynamic Nuclear Polarization*, Massachusetts Institute of Technology, Department of Electrical Engineering and Computer Science, Sept. 2001.
- [18] M. Airila, *Electron Energy Spectra in Gyrotrons with Depressed Collectors*, Master's thesis, Helsinki University of Technology, Department of engineering physics and mathematics, November 2000.
- [19] M.V. Kartikeyan, E. Borie, M.K. Thumm, "Possible operation of a 1.5-2-MW, CW conventional cavity gyrotron at 140 GHz," *IEEE Transactions on Plasma Science*, vol. 11, no. 7, pp. 837-850, 1990.
- [20] Amitavo Roy Choudhury, "Investigations of after cavity interaction in gyrotrons including the effect of non-uniform magnetic field," *Dissertation, Karlsruhe Institut für Technologie (KIT)*, 2013.
- [21] B. Piosczyk, "Non-adiabatic electron gun for gyrotrons," *International Journal of Electronics*, vol. 67, no. 3, pp 447-456, 1989.
- [22] R.A. Correa, J.J. Barroso, "Space charge effects of gyrotron electron beams in coaxial cavities," *Int. J. Electronics*, vol. 74, no. 1, pp. 131-136, 1993.

- [23] Joon Y. Choe, S. Ahn, "General Mode Analysis of a Gyrotron Dispersion Equation," *IEEE Transactions on Electron Devices*, vol. ED-28, no. 1, pp. 94-102, January 1981.
- [24] G. I. Zaginaylov, V. I. Shcherbinin, and K. Schuenemann, "Linear Theory of Electron Cyclotron Instability of Electromagnetic Waves in a Magnetoactive Plasma Waveguide," *Plasma Physics Report*, vol. 33, no. 8, 2007.
- [25] C. J. Edgcombe, "The dispersion equation for the gyrotron amplifier," *International Journal of Electronics*, vol. 48, no. 6, pp. 471-486, 1980.
- [26] Z. Shi Chang, "On the gyrotron dispersion equation for a general mode," *International Journal of Electronics*, vol. 60, no. 2, pp. 297-299, 1986.
- [27] S. Ahn, J. Choe, "Analysis of the Gyrotron Amplifier for Azimuthally Varying TE Modes," *IEEE Electron Devices Letters*, vol. edl-1, no. 1, January 1980.
- [28] Y. Choyal, T. Watanabe, K. Minami, "Microwave Excitation by a Constrained Large-Orbit Electron Beam—A Unified Dispersion Relation for Slow- and Fast-Wave Devices," *IEEE Transactions on Plasma Science*, vol. 32, no. 3, June 2004.
- [29] G. Dammertz, O. Dumbrajs, K. Koppenburg, B. Piosczyk, M. Thumm, "Frequency-step-tunable high-power gyrotron for plasma physics applications," *Electronics and Radiophysics of Ultra-High Frequencies, 1999. International University Conference Proceedings*, pp.108,111, Aug 1999.
- [30] A. Schlaich, G. Gantenbein, J. Jelonnek, M. Thumm, "Transient Millimeter-Wave Signal Analysis With Unambiguous RF Spectrum Reconstruction," *IEEE Transactions on Microwave Theory and Techniques*, vol. 61, no. 12, December 2013.

- [31] A. Roy Choudhury, S. Kern, D. D'Andrea, M. Thumm, "Numerical investigations of parasitic oscillations in gyrotrons," *Plasma Science (ICOPS), 2012 Abstracts IEEE International Conference on*, pp.1P-8,1P-8, 8-13 July 2012.
- [32] Nitin Kumar, Udaybir Singh, T. P. Singh, A. K. Sinha, "Suppression criteria of parasitic mode oscillations in a gyrotron beam tunnel," *Physics of Plasmas* 18, 022507, 2011.
- [33] G.P. Latsas, Z.C. Ioannidis, I.G. Tigelis, "Numerical studies on the parasitic modes in gyrotron beam tunnels," *Plasma Science (ICOPS), 2011 Abstracts IEEE International Conference on*, pp.1,1, 26-30 June 2011.
- [34] I.G. Chelis, K.A. Avramidis, J.L. Vomvoridis, "Simulation of parasitic gyrotron interaction in beam tunnels," *Infrared, Millimeter, and Terahertz Waves (IRMMW-THz), 2013 38th International Conference on*, pp.1-2, 1-6 Sept. 2013.
- [35] G.S. Nusinovich, O.V. Sinitsyn, T.M. Antonsen, A.N. Vlasov, "How to avoid excitation of parasitic modes in MW-class gyrotrons?," *Plasma Science, 2008. ICOPS 2008. IEEE 35th International Conference on*, pp.1,1, 15-19 June 2008.
- [36] J. Yu, T.M. Antonsen, G.S. Nusinovich, "Excitation of backward waves in the beam tunnel of a high power gyrotron," *Infrared, Millimeter and Terahertz Waves, 2008. IRMMW-THz 2008. 33rd International Conference on*, pp.1-2, 15-19 Sept. 2008.
- [37] M. Pedrozzi, S. Alberti, J. P. Hogge, M. Q. Tran, and T. M. Tran, "Electron beam instabilities in gyrotron beam tunnels," *Physics of Plasmas*, vol. 5, no. 6, pp. 2421-2430, June 1998.
- [38] I. I. Antakov, I. G. Gachev, and E. V. Zasyrkin, "Self-excitation of spurious oscillations in the drift region of gyrotron and their influence on gyrotron operation," *IEEE Trans. Plasma Science*, vol. 22, no. 5, pp. 878-882, Oct. 1994.

## BIBLIOGRAPHY

---

- [39] G. P. Latsas, J. L. Vomvoridis, K. A. Avramides, and I. G. Tigelis, "Beamwave interaction in slow-wave structures in the small-signal regime," *IEEE Trans. Plasma Science*, vol. 37, no. 10, pp. 2020-2030, Oct. 2009.
- [40] J.-P. Hogge et al., "First experimental results from the European Union 2-MW coaxial cavity ITER gyrotron prototype", *Fusion Science and Technology*, 55, Feb. 2009, pp. 204-212.



BIBLIOGRAPHY

---

